



UNIVERSITY OF THE  
WITWATERSRAND,  
JOHANNESBURG

**Soft-Decision Decoding Techniques for Permutation Modulation in Powerline  
and Visible Light Communication**

**KOLADE Oluwafemi Ibrahim**  
(ORCID: 0000-0002-8337-3827)

Supervised by: **Prof. Ling Cheng**

A thesis submitted to the Faculty of Engineering and the Built Environment, University of the  
Witwatersrand, Johannesburg, in fulfilment of the requirements for the degree of Doctor of  
Philosophy

**November, 2020**

## Declaration

I declare that this thesis is my own unaided work. It is being submitted for the Degree of Doctor of Philosophy to the University of the Witwatersrand, Johannesburg. It has not been submitted before for any degree or examination to any other University.

**KOLADE Oluwafemi Ibrahim**



---

Braamfontein, Johannesburg  
3 November, 2020

## Abstract

As the realization of smart cities and connected internet of things (IoT) devices becomes imminent, the spectral requirements of the volume of devices requiring data communication will exceed the available radio frequency spectrum. Alternative means of communication such as powerline and visible light communication (VLC) are proposed as supplementary data links to radio frequency communication. Powerline communication (PLC) is essential to the deployment of smart grids since the equipment's powerlines can also be used for communication. Since indoor illumination units are powered by powerlines, a natural integration exists between the powerline and visible light unit, extending the indoor VLC unit to the grid via the powerline. However, the PLC channel becomes noisy due to 'burst' impulses introduced into the channel by other powered equipment. VLC units on the other hand, exist in a cluster of light emitting diodes (LEDs), hence the presence of cross-talk interference among the emitting transmitters.

In this research, the channel model of an amplify-and-forward (AF) hybrid PLC-VLC system is designed using the Fritchman model, a semi-hidden Markov model. Measurements are obtained from an indoor testbed for multicarrier, orthogonal frequency division multiplexing (OFDM) modulation with binary phase shift keying (BPSK). With adequate knowledge of the channel's error distribution, adequate coding such as permutation codes (PC) and permutation trellis codes (PTC) are recommended to mitigate the bursts of errors in the channel when combined with  $M$ -ary frequency shift keying ( $M$ -FSK). The combination of codewords with distinct properties are then used to novelistically increase the data rate of a permutation coded multiple-input multiple-output (MIMO) VLC scheme. In order to improve the bit error rate (BER) of PC and PTC with  $M$ -FSK, novel soft-decision techniques are presented. Soft-decision is possible by interpreting the output of the channel as an assignment problem, hence the use of optimization algorithms for detection. The optimization algorithms are then used to mitigate the effects of impulse noise in permutation-coded OFDM- $M$ FSK and avoid channel estimation errors in space-time shift keying (STSK).

## **Dedication**

This thesis is dedicated to my beautiful wife, *Oluwatomisin*. Thank you for all your selfless love and support during the course of this degree.

## Acknowledgments

First, I would like to thank my supervisor Prof. Ling Cheng for his excellent, hands-on supervision and mentorship over the course of the PhD. I found the thorough discussions, brainstorming sessions and ideas very valuable, providing me with a solid foundation for research and development.

I would like to thank my wife, Tomi. From the time we were dating and even after we got married, her companionship, support and understanding have been very key to the completion of my degree. Also, I am grateful for my parents and my entire family for their understanding and support when I had to leave industry to be a student for another 5 years so as to complete my MSc and now PhD. In particular, Momore and Tobi, my little niece and dear nephew who I had evening chats with when studying was tough.

I would also like to thank the Wits-Sibanye Stillwater Digital Mining Laboratory (DigiMine), Wits Mining Institute (WMI) for generously funding my research and providing me with the resources I needed. In particular, I would like to thank Prof. Frederick Cawood at the WMI for his leadership, for providing me with some exposure to the digital space of deep level underground mining, international collaborators, industry partners and projects that have contributed to my research career development.

To God be the glory.

---

## Publications

### Conferences

1. O. Kolade, M. Cox, and L. Cheng, "Visible Light Communication using a Software-defined Radio Approach", In *SPIE Fifth Conference on Sensors, MEMS, and Electro-Optic Systems*, Jan. 2019.
2. (Invited) O. Kolade and L. Cheng, "Impulse Noise Mitigation Using Subcarrier Coding of OFDM-MFSK Scheme in Powerline Channel", *IEEE SmartGridComm*, Oct. 2019.
3. O. Kolade and L. Cheng, "Permutation-Aided Space-Time Shift Keying for Indoor Visible Light Communication", *IEEE SmartGridComm*, Oct. 2019.

### Journals

1. O. Kolade, M. Shimaponda-Nawa, D.J.J Versfeld, and L. Cheng, "Optimization Algorithms for Improving the Performance of Permutation Trellis Codes". *Under revision with Elsevier Physical Communication*.
2. O. Kolade, A. D. Familua, and L. Cheng, "Indoor Amplify-and-Forward Power-Line and Visible Light Communication Channel Model Based on a Semi-Hidden Markov Model." *AEÜ - International Journal of Electronics and Communications*, p. 153108, Feb. 2020.
3. O. Kolade, and L. Cheng, "Low-Complexity Detection of Multiweight Permutation Modulation Space-Time Block Codes for Indoor Visible Light Communication". *Under review with Elsevier Optics Communications*.
4. O. Kolade, J. Versfeld, and M. van Wyk, "Soft-Decision Decoding of Permutation Block Codes in AWGN and Rayleigh Fading Channels", *IEEE Communications Letters*, vol. 21, no. 12, pp. 2590 - 2593, Dec. 2017.

### Book Chapters

1. (Invited) O. Kolade, A.D. Familua, and L. Cheng, "Channel Models for an Indoor Powerline Communication System for Smart Cities", *IET Book on Networked Smart Cities*. *In press*.

# Contents

<b>List of Figures</b>	<b>x</b>
<b>List of Tables</b>	<b>xiii</b>
<b>Abbreviations</b>	<b>xiv</b>
<b>1 Introduction</b>	<b>1</b>
1.1 Research Question and Contributions	3
<b>2 Background Review</b>	<b>4</b>
2.1 Memoryless PLC and VLC Channel	5
2.1.1 Multipath Channel Model for PLC	5
2.1.2 Middleton Class A Noise Model for PLC	6
2.1.3 Bernoulli-Gaussian Noise Model for PLC	8
2.1.4 VLC Channel Model	8
2.1.4.1 Indoor VLC Channel Model	8
2.1.4.2 VLC Transmitter using Summing Amplifier	9
2.1.4.3 VLC Receiver using Transimpedance Amplifier	10
2.2 Memory, Discrete Channel Modelling	11
2.3 Coding and Modulation	11
2.3.1 Phase Shift Keying (PSK)	12
2.3.2 Pulse Amplitude Modulation	12
2.3.3 Orthogonal Frequency Division Multiplexing (OFDM)	13
2.3.3.1 Inverse Fast Fourier Transform	14
2.3.3.2 Cyclic Prefix	14
2.3.4 Permutation Codes with $M$ -ary Frequency Shift Keying	14
2.3.5 Permutation Trellis Codes with $M$ -FSK	15
2.3.6 Single Carrier Modulation for PLC	17
2.3.7 Multicarrier Modulation for PLC	19
2.3.7.1 Multicarrier Impulse Noise Model	19
2.3.8 MIMO Space-Time Shift Keying for VLC	20
2.3.9 Multicarrier Modulation in Hybrid Amplify-and-Forward PLC-VLC	22
<b>3 Indoor Amplify-and-Forward Powerline and Visible Light Communication Channel Model Based on Semi-Hidden Markov Models</b>	<b>23</b>
3.1 Introduction	23
3.2 Channel Modelling	24
3.2.1 Theoretical Model for PLC and VLC	25
3.2.2 Markov Model for Memory PLC-VLC Channel	26
3.2.3 Fritchman Model	27
3.2.4 Baum-Welch Algorithm	27
3.2.5 Semi-Hidden Fritchman HMM	28
3.3 Experimental Setup and Measurements	29
3.4 Results	30

3.4.1	Estimated Model (State Transition Probabilities) . . . . .	30
3.4.2	Estimated Model Validation . . . . .	31
3.4.2.1	Log-Likelihood Ratio Plots . . . . .	31
3.4.2.2	Error-Free Run Distribution Plots . . . . .	32
3.4.2.3	Error Probabilities . . . . .	33
3.5	Conclusion . . . . .	34
<b>4</b>	<b>Soft-Decision Decoding of Permutation Block Codes in AWGN and Rayleigh Fading Channels</b>	<b>36</b>
4.1	Introduction . . . . .	36
4.2	$M$ -FSK and Permutation Codes . . . . .	37
4.3	Channel Model . . . . .	37
4.4	Soft-Decision Decoder . . . . .	38
4.4.1	Hungarian Algorithm . . . . .	38
4.4.2	Murty's Algorithm . . . . .	39
4.4.3	Maximum Likelihood Decoding . . . . .	39
4.5	Simulation Results . . . . .	40
4.6	Conclusion . . . . .	42
<b>5</b>	<b>Impulse Noise Mitigation Using Subcarrier Coding of OFDM-MFSK Scheme in Powerline Channel</b>	<b>43</b>
5.1	Introduction . . . . .	43
5.2	System Model . . . . .	44
5.2.1	OFDM-MFSK . . . . .	44
5.3	Proposed Scheme . . . . .	45
5.3.1	OFDM-MFSK with Permutation Codes . . . . .	45
5.3.2	OFDM-MFSK with Permutation Codes in Powerline Communication Channel . . . . .	47
5.3.3	Soft-Decision Decoding in Frequency Domain . . . . .	47
5.4	Simulation Results . . . . .	48
5.5	Conclusion . . . . .	51
<b>6</b>	<b>Optimization Algorithms for Improving the Performance of Permutation Trellis Codes</b>	<b>52</b>
6.1	Introduction . . . . .	52
6.2	System Model . . . . .	53
6.2.1	Permutation Trellis Codes . . . . .	53
6.2.2	$M$ -ary Frequency Shift Keying with PTC . . . . .	54
6.2.3	Probability of Error of PTC . . . . .	55
6.2.4	The Permutation Soft-Decision Decoder . . . . .	57
6.3	Proposed Soft-Decision Decoder and Schemes . . . . .	58
6.3.1	Branch and Bound . . . . .	58
6.3.2	Schemes . . . . .	59
6.3.2.1	Scheme 1 . . . . .	59
6.3.2.2	Scheme 2 . . . . .	59
6.3.2.3	Schemes 3 & 4 . . . . .	59
6.4	Simulation Results and Complexity Analysis . . . . .	60
6.4.1	BER Performance and $\frac{2^n}{M!}$ Ratio . . . . .	60
6.4.2	Complexity Analysis . . . . .	62
6.5	Conclusion . . . . .	63
<b>7</b>	<b>Permutation-Aided Space-Time Shift Keying for Indoor Visible Light Communication</b>	<b>64</b>
7.1	Introduction . . . . .	64
7.2	System Model . . . . .	65

7.2.1	Permutation-Aided STSK Scheme . . . . .	66
7.3	Proposed Optimization Algorithms as Soft-Detection Receiver . . . . .	68
7.4	Simulation Results . . . . .	69
7.4.1	BER Performance and $\frac{Q}{ T }$ Ratio . . . . .	70
7.4.2	Effect of Minimum Distance and Modulation Order $M$ . . . . .	71
7.5	Conclusion . . . . .	72
<b>8</b>	<b>Low-complexity Detection of Multiweight Permutation Modulation Space-Time Block Codes for Indoor Visible Light Communication</b> . . . . .	<b>73</b>
8.1	Introduction . . . . .	73
8.2	System Model for Permutation-Aided MIMO For VLC . . . . .	74
8.2.1	Permutation-Aided STSK Scheme . . . . .	74
8.2.2	MIMO VLC Channel Model . . . . .	75
8.2.3	Concatenated Permutations for STSK . . . . .	76
8.3	Proposed Optimization Algorithms for Soft-Decision Detection . . . . .	78
8.3.1	Brute Force Soft-Decision Receiver . . . . .	78
8.3.2	Branch and Bound . . . . .	78
8.3.3	Iterative Soft-Decision Detection . . . . .	79
8.4	Simulation Results . . . . .	79
8.4.1	BER Analysis . . . . .	81
8.4.2	Mobile Receiver without CSI . . . . .	82
8.4.3	Data Rate Analysis . . . . .	82
8.4.4	Complexity Analysis of Soft-Decision Decoders . . . . .	83
8.5	Conclusion . . . . .	84
<b>9</b>	<b>Conclusions and Future Work</b> . . . . .	<b>85</b>
9.1	Conclusions . . . . .	85
9.2	Future Work . . . . .	86
	<b>Bibliography</b> . . . . .	<b>87</b>

# List of Figures

2.1	Connection between the grid to a smart home with powerline also serving as a data communication link. . . . .	4
2.2	PLC network illustrating multipath model in the branches. . . . .	6
2.3	Amplitude response for $N = 4$ . . . . .	6
2.4	Envelope distribution for $\Lambda = 0.1$ . . . . .	7
2.5	2-state Middleton Class A noise model. . . . .	7
2.6	2-state Bernoulli-Gaussian noise model. . . . .	7
2.7	Block diagram of an optical communication system in baseband. . . . .	8
2.8	Geometric model of transmitter LED and receiver PD. . . . .	9
2.9	LOS channel gain with $\phi = 10^\circ$ , $d = 2$ m. . . . .	10
2.10	Voltage adder circuit to supply DC bias and amplification to the transmitted signal. . .	10
2.11	Transimpedance amplifier to convert photodiode current $I_{TIA}$ to voltage. . . . .	10
2.12	BPSK constellation . . . . .	12
2.13	4-PSK constellation . . . . .	12
2.14	Gray-coded 4-PAM constellation mapping . . . . .	13
2.15	OFDM flow diagram. . . . .	13
2.16	Synchronized OFDM message structure . . . . .	14
2.17	BPSK and OFDM-BPSK heavily disturbed scenario. . . . .	20
2.18	BPSK and OFDM-BPSK mildly disturbed scenario. . . . .	20
2.19	4FSK and OFDM-4FSK heavily disturbed scenario. . . . .	21
2.20	4FSK and OFDM-4FSK mildly disturbed scenario. . . . .	21
3.1	Block diagram of hybrid AF PLC-VLC . . . . .	25
3.2	Geometric model of a Lambertian LED and PD . . . . .	25
3.3	Fritchman Model with 3 States . . . . .	27
3.4	Hybrid AF PLC-VLC indoor laboratory testbed. . . . .	29
3.5	VLC transmitter unit. . . . .	29
3.6	VLC receiver unit. . . . .	29
3.7	Voltage adder circuit to supply DC bias and amplification to the transmitted signal. . .	30
3.8	Transimpedance amplifier to convert photodiode current $I_{TIA}$ to voltage. . . . .	30
3.9	LLR plot 1. . . . .	32
3.10	LLR plot 2. . . . .	32
3.11	LLR plot 3. . . . .	32
3.12	LLR plot 4. . . . .	32
3.13	Measured vs. model-generated EFRD 1. . . . .	33
3.14	Measured vs. model-generated EFRD 2. . . . .	33
3.15	Measured vs. model-generated EFRD 3. . . . .	33
3.16	Measured vs. model-generated EFRD 4. . . . .	33
3.17	Probability of error for different values of $w$ with $d = 40$ cm measured from the hybrid channel. . . . .	34
4.1	Performance of the soft-decision decoder in AWGN channel using 4 codewords (CW). . .	41
4.2	Performance of the soft-decision decoder in AWGN Channel using 24 codewords (CW). .	41

4.3	Performance of the soft-decision decoder in AWGN & Rayleigh fading channels using 4 codewords (CW).	42
5.1	System diagram showing permutation codes with OFDM-MFSK without the block with dotted lines. Including block with dotted lines describes OFDM-MFSK-DPSK.	44
5.2	Encoded information bits 0010 are mapped to subcarriers such that the mapping in each group corresponds to each symbol in the permutation codeword 1342.	46
5.3	BER performance comparing permutation coded OFDM-4FSK scheme with the uncoded scheme in AWGN, $L = 4$ , $ C  = 4$ .	48
5.4	BER performance comparing permutation coded OFDM-4FSK scheme with the uncoded scheme in PLC, $\frac{\sigma_G}{\sigma_I} = 0.1$ , $L = 4$ , $ C  = 4$ .	49
5.5	BER performance comparing permutation coded OFDM-4FSK-4DPSK scheme with the uncoded scheme in AWGN, $L = 4$ , $ C  = 4$ .	49
5.6	BER performance comparing permutation coded OFDM-4FSK-4DPSK scheme with the uncoded scheme in PLC, $\frac{\sigma_G}{\sigma_I} = 0.1$ , $L = 4$ , $ C  = 4$ .	50
5.7	BER performance comparing permutation coded OFDM-8FSK-4DPSK scheme with the uncoded scheme in PLC, $\frac{\sigma_G}{\sigma_I} = 0.1$ , $L = 8$ , $ C  = 256$ .	50
6.1	System model for permutation trellis encoder.	53
6.2	State transition diagram for $R_C = 1/2$ and $R_P = 1/3$ .	54
6.3	Trellis representation of the PTC for $R_C = 1/2$ and $R_P = 1/3$ .	54
6.4	Tree-based method to decode permutation codes using branch and bound with $M = 4$ .	58
6.5	Decoder system model of permutation code soft-decision and permutation trellis decoder.	59
6.6	BER comparisons of HD with SD schemes for code having $R_C = 1/2$ and $M = 3$ .	61
6.7	Schemes 1 & 3 with Viterbi decoding of PTC codewords for $R_C = 1/2$ and $M = 3$ in AWGN channel.	61
6.8	Schemes 2 & 4 with Viterbi decoding of demapped codewords for $R_C = 1/2$ and $M = 3$ in AWGN channel.	61
6.9	Schemes 1 & 3 with Viterbi decoding of PTC codewords for $R_C = 2/3$ , $M = 4$ and $A = 0.1$ in PLC channel.	62
6.10	Schemes 2 & 4 with Viterbi decoding of demapped codewords for $R_C = 2/3$ , $M = 4$ and $A = 0.1$ in PLC channel.	62
6.11	Schemes 1 & 3 with Viterbi decoding of PTC codewords for $R_C = 1/4$ , $M = 4$ and $A = 0.1$ in PLC channel.	62
6.12	Schemes 2 & 4 with Viterbi decoding of demapped codewords for $R_C = 1/4$ , $M = 4$ and $A = 0.1$ in PLC channel.	62
7.1	Room dimensions with transmitter and receiver arrangement.	65
7.2	Geometric model of transmitter LED and receiver PD.	65
7.3	System model for permutation-aided STSK with soft-detection.	66
7.4	BER performance of PSTSK(4, 4, 4, 2) using codebook with $d_{\min} = 4$ selected from $ T  = 24$ .	69
7.5	BER performance of PSTSK(4, 4, 4, 4) using codebook with $d_{\min} = 4$ selected from $ T  = 24$ .	69
7.6	PSTSK(6, 6, 256, 4) when $\frac{Q}{ T } = 0.3556$ . Codebook's $d_{\min} = 3$ and $Q = 256$ , selected from $ T  = 720$ .	70
7.7	PSTSK(6, 6, 512, 2) when $\frac{Q}{ T } = 0.7111$ . Codebook's $d_{\min} = 2$ and $Q = 512$ , selected from $ T  = 720$ .	70
7.8	dB gain between the ML and SD at $e = 4$ at different ratios of $\frac{Q}{ T }$ .	71
7.9	BER vs SNR comparing the performance of the SD's 4th iteration with ML detection of a PSTSK(4, 4, 4, $M$ ) setup with $d_{\min} = 4$ .	71

---

8.1	System model for permutation-aided STSK with soft-detection. . . . .	75
8.2	Tree-based method to decode permutation codes using branch and bound with $L = 4$ . .	79
8.3	BER comparisons of PM with RC and SM for two channel matrices transmitting 4 bits. The circles and squares are plots for $\mathbf{H}_{0.2}$ and $\mathbf{H}_{0.6}$ respectively. . . . .	80
8.4	BER of concatenated codebooks of $w = 1$ and $w = 2$ containing 24 and 8 codewords respectively. . . . .	80
8.5	Comparison of soft-decision techniques with ML performance for P(4, 8, 1, 1) and P(4, 8, 1, 2) with $\mathbf{H}_{0.2}$ . . . . .	81
8.6	Top view cross-section of transmitter and receiver placements. . . . .	81
8.7	BER of concatenated codebooks of P(4, 8, 1, {1, 2}) transmitting 5 bits with receiver at the transmitter's center using $\mathbf{H}_{0.6}$ and different positions of the receiver. . . . .	83
8.8	BER of concatenated codebooks of P(4, 8, 1, {1, 2}) using $\tilde{\mathbf{H}}_{0.6}$ for different positions of the receiver. . . . .	83

# List of Tables

2.1	PLC parameters for $N = 4$ paths . . . . .	6
2.2	Distance increasing mapping (DIM) of binary code of length $n = 2$ to $L = 3$ permutation code . . . . .	16
2.3	Distance increasing mapping (DIM) of binary code of length $n = 3$ to $L = 4$ permutation code . . . . .	16
3.1	USRP and modulation parameters . . . . .	30
3.2	Estimated Models (estimated state transition probabilities) . . . . .	31
3.3	Error probabilities comparison ( $(P_e)$ - measured sequence vs. $(\bar{P}_e)$ - model regenerated sequence . . . . .	35
4.1	Performance of the soft-decision decoder using 8-FSK in AWGN channel, non-coherent detection . . . . .	41
4.2	Performance of the soft-decision decoder using 8-FSK in AWGN and Rayleigh fading channel . . . . .	42
6.1	Two sample mappings of binary outputs of convolutional code to non-binary permutation codes . . . . .	54
7.1	Mapping of message bits to PSTSK and Modulation Scheme . . . . .	67
8.1	Mapping between modulation scheme and codes with $w = 1$ and $w = 2$ . . . . .	77

# Abbreviations

<b>A-CSTSK</b>	<b>Asynchronous Coherent STSK</b>
<b>ACO-OFDM</b>	<b>Asymmetrically Clipped Optical OFDM</b>
<b>ADC</b>	<b>Analog to Digital Conversion</b>
<b>AE</b>	<b>Antenna Element</b>
<b>AF</b>	<b>Amplify-and-Forward</b>
<b>AWGN</b>	<b>Additive White Gaussian Noise</b>
<b>BB</b>	<b>Branch and Bound</b>
<b>BER</b>	<b>Bit Error Rate</b>
<b>BPSK</b>	<b>Binary Phase Shift Keying</b>
<b>CSI</b>	<b>Channel State Information</b>
<b>D-STSK</b>	<b>Differential Space-Time Shift Keying</b>
<b>DAC</b>	<b>Digital to Analog Conversion</b>
<b>DC</b>	<b>Direct Current</b>
<b>DCO-OFDM</b>	<b>Direct Current Optical OFDM</b>
<b>DD</b>	<b>Direct Detection</b>
<b>DF</b>	<b>Decode-and-Forward</b>
<b>DPSK</b>	<b>Differential Phase Shift Keying</b>
<b>DSM</b>	<b>Differential Spatial Modulation</b>
<b>ED</b>	<b>Envelope Detection</b>
<b>EFRD</b>	<b>Error Free Run Distribution</b>
<b>FM</b>	<b>Fritchman Model</b>
<b>GF</b>	<b>Galois Field</b>
<b>HA</b>	<b>Hungarian Algorithm</b>
<b>HD</b>	<b>Hard Decision</b>
<b>HMM</b>	<b>Hidden Markov Model</b>
<b>ICI</b>	<b>Inter-Channel Interference</b>
<b>IDFT</b>	<b>Inverse Discrete Fourier Transform</b>
<b>IFFT</b>	<b>Inverse Fast Fourier Transform</b>
<b>IM</b>	<b>Index Modulation</b>
<b>IN</b>	<b>Impulse Noise</b>
<b>IoT</b>	<b>Internet of Things</b>
<b>ISI</b>	<b>Inter-Symbol Interference</b>
<b>LED</b>	<b>Light Emitting Diode</b>
<b>LLR</b>	<b>Log-Likelihood Ratio</b>
<b>LOS</b>	<b>Line-of-Sight</b>
<b><i>M</i>-FSK</b>	<b><i>M</i>-ary Frequency Shift Keying</b>
<b><i>M</i>-PSK</b>	<b><i>M</i>-ary Phase Shift Keying</b>
<b>MIMO</b>	<b>Multiple-Input Multiple-Output</b>
<b>MOLS</b>	<b>Mutually Orthogonal Latin Squares</b>
<b>NB</b>	<b>Narrowband</b>
<b>NBI</b>	<b>Narrowband Interference</b>
<b>OD</b>	<b>Optimal Decision</b>
<b>OFDM</b>	<b>Orthogonal Frequency Division Multiplexing</b>
<b>OOK</b>	<b>On-Off Keying</b>
<b>PD</b>	<b>PhotoDiode</b>
<b>PDF</b>	<b>Probability Density Function</b>

---

<b>PEP</b>	<b>P</b> airwise <b>E</b> rror <b>P</b> robability
<b>PLC</b>	<b>P</b> owerline <b>C</b> ommunication
<b>PM</b>	<b>P</b> ermutation <b>M</b> odulation
<b>PPM</b>	<b>P</b> ulse <b>P</b> osition <b>M</b> odulation
<b>PSDD</b>	<b>P</b> ermutation <b>S</b> oft <b>D</b> ecision <b>D</b> ecoder
<b>PSK</b>	<b>P</b> hase <b>S</b> hift <b>K</b> eying
<b>PTC</b>	<b>P</b> ermutation <b>T</b> rellis <b>C</b> ode
<b>QAM</b>	<b>Q</b> uadrature <b>A</b> mplitude <b>M</b> odulation
<b>RF</b>	<b>R</b> adio <b>F</b> requency
<b>SD</b>	<b>S</b> oft- <b>D</b> ecision
<b>SHFMM</b>	<b>S</b> emi- <b>H</b> idden <b>F</b> ritchman <b>M</b> arkov <b>M</b> odel
<b>SHMM</b>	<b>S</b> emi- <b>H</b> idden <b>M</b> arkov <b>M</b> odel
<b>SM</b>	<b>S</b> patial <b>M</b> odulation
<b>SNR</b>	<b>S</b> ignal to <b>N</b> oise <b>R</b> atio
<b>SSK</b>	<b>S</b> pace- <b>S</b> hift <b>K</b> eying
<b>STSK</b>	<b>S</b> pace- <b>T</b> ime <b>S</b> hift <b>K</b> eying
<b>TIA</b>	<b>T</b> ransimpedance <b>A</b> mplifier
<b>USRP</b>	<b>U</b> niversal <b>S</b> oftware- <b>D</b> efined <b>R</b> adio <b>P</b> eripheral
<b>WDM</b>	<b>W</b> ave <b>D</b> ivision <b>M</b> ultiplexing
<b>VLC</b>	<b>V</b> isible <b>L</b> ight <b>C</b> ommunication

# Introduction

The growth of the digital revolution continues to create a high demand for fast, reliable and efficient data communication channels that also effectively utilize the available data transmission spectrum. The immediate future is the development of internet of things (IoT) frameworks, smart grids and smart devices for better connectivity of technology and people across the world. Powerline communication (PLC) is recommended to play a critical role in realizing smart grid technology by using existing power installations for communication. The channel is however prone to interference as a result of impulses from devices connected to the powerline bus network. While several noise mitigation techniques exist in wireless, radio frequency (RF) and wired communication systems, the behaviour of noise in the PLC channel, some of which are man-made require different modulation and coding techniques. Hence, there is a need for efficient coding and modulation schemes to mitigate the effects of impulse and frequency-selective interference in the channel. On the other hand, visible light communication (VLC) uses light emitting diode (LED) units for communication by using light within the visible light spectrum (430-790 THz). A natural integration exists between the two channels as the VLC unit is usually powered by a powerline cable. Hence, the VLC unit can be extended towards the network backbone via the PLC. However, the VLC installation unit usually consists of a cluster of LEDs for adequate illumination. As a result, multiple-input multiple-output (MIMO) schemes such as space-time shift keying (STSK) which mitigates cross-talk between information emitting transmitters is proposed. Furthermore, the efficient detection of MIMO STSK at the receiver is necessary for scenarios with multiple LEDs at the transmitter and multiple photodiodes (PDs) at the receiver.

VLC [1, 2] is widely proposed as an alternative and sometimes supplementary [3–5] to RF data communication due to its huge, unlicensed bandwidth. Signals are modulated simply by using single carrier modulation such as on-off keying (OOK) and pulse-position modulation (PPM). In order to increase the data rate, multicarrier modulation such as wavelength division multiplexing (WDM) [6–9] is used by producing white light from the combination of red, green and yellow LED color combinations. Orthogonal frequency division multiplexing (OFDM) also efficiently increases the data rate in a single LED by spreading a sequence of information over  $N$  orthogonal subcarriers. The OFDM sequences are designed to have the Hermitian symmetry structure, so that the inverse fast Fourier transform (IFFT) of the signal produces real and positive discrete signals. Two common methods to achieve this are asymmetrically clipped optical OFDM (ACO-OFDM) and direct current biased optical OFDM (DCO-OFDM) [10–12]. ACO-OFDM clips all negative signals to zero while DCO-OFDM adds a DC bias to the information signal.

The natural integration of PLC with VLC brings the ‘isolated’ VLC system closer to a communication backbone. The integration of PLC with VLC was introduced in [13] using a simple wiring between the PLC and VLC module. Since then, single carrier modulation schemes such as OOK [14] and spread frequency shift keying [15] have been introduced. In order to increase the data rate of the integrated channels, multicarrier modulation using narrowband OFDM has also been demonstrated in [16, 17]. Furthermore, channel models of integrated PLC-VLC are provided in [18, 19] in order to provide adequate channel knowledge required for relevant modulation and coding schemes suited for the channels. However, experimental integration of PLC with VLC in literature such as [20, 21] emphasize the decode-and-forward (DF) method. In this method, the transmitted information is decoded and

demodulated using the PLC receiver unit before re-encoding and re-modulating for transmission via the VLC transmitter. This method is effective because errors can be corrected at the PLC channel's output before forwarding to the VLC transmitter unit. The drawback however is that additional circuitry is required to decode, demodulate, re-encode and re-modulate the information with complexity depending on the coding and modulation scheme.

This research develops a channel model for the multicarrier, hybrid amplify-and-forward (AF) PLC-VLC channel [22]. The AF design does not require additional circuitry and algorithms to decode the PLC channel output before re-transmitting over the VLC channel. This presents a low-cost design that requires minimal changes to the existing circuitry in the existing indoor PLC and VLC installations. However, the PLC channel is known to be noisy due to the devices plugged into the powerline 'bus' network, creating impulse sparks in the narrowband region. The AF module on the other hand, introduces noise due to the components in the circuitry. A channel model is therefore designed using a semi-hidden Markov model with the aid of the Fritchmann model in order to understand the noise distribution in the cascaded channels. This is done using a testbed setup with measurements taken under different indoor PLC load conditions and VLC geometric setups.

Permutation block codes with  $M$ -ary frequency shift keying ( $M$ -FSK) have been proposed to combat impulse noise (IN) in the PLC channel due to the combined schemes' ability to spread the signal over the spectrum in the frequency and time domain. This allows the signal to be successfully decoded, provided the parts of the signal affected by the impulses are not beyond the limits of the code's decoding capability. The frequency hopping nature of  $M$ -FSK can also be an advantage to the signal in avoiding the bad parts of the channel. The use of a convolutional code as an outer code for the permutation code, otherwise known as a permutation trellis code (PTC) further improves the coding performance of permutation codes in PLC channels. PTC proposed in [23] becomes even more attractive due to its ability to be decoded using a modified Viterbi decoder which decodes the demodulated permutation sequence directly, rather than first converting the demodulated sequence to its equivalent binary sequence before decoding. In this research, the output of the channel such as PLC is interpreted as an assignment problem. This allows the decoding of the soft-output of the channel using combinatorial optimization algorithms. The Hungarian, Murty and branch and bound algorithms will be used to design decoders for PTC, with the performances discussed and analyzed. The decoder is further extended to multicarrier OFDM in an AF PLC-VLC to mitigate IN in the frequency domain.

VLC modules usually include a cluster of LEDs in each illuminating unit. Multiple-input communication is therefore possible with existing illumination installations and can be used to improve error rate performance while taking advantage of the spatial, time, transmitter or receiver diversity. Index modulation (IM) is an example of a MIMO scheme in which an LED luminary or set of LEDs are activated based on the incoming input bits. In RF communication, a STSK scheme was presented in [24, 25] which extends spatial modulation (SM) and space-shift keying (SSK) by achieving space and time diversity of the transmitters. While this scheme mitigates inter-channel interference (ICI) between the multiple transmitters, the knowledge of the channel state information (CSI) is required for the maximum likelihood (ML) detection of the transmitted symbols. Based on the asynchronous coherent STSK (A-CSTSK) proposed in [24, 25], we propose a permutation-based STSK scheme. In this scheme, a permutation matrix is activated in addition to a constellation from a modulation scheme in order to transmit data over space and time in a MIMO VLC system. The index of the VLC transmitter to be activated at each time in a space-time block is determined by the index of the non-zero element of the permutation matrix. Concatenated codewords which have the highest possible Hamming distance between them are then used to increase the number of bits the transmitting matrix can convey, while maintaining the power constraint requirements of the system. Soft-decision detection is also presented to reduce the complexity of the ML detection receiver using optimization algorithms. This soft-detection algorithm is also capable of detecting the transmitted symbols with or without the knowledge of CSI. Results show the soft-decision detector's bit error rate (BER) matches the ML in certain setups when the SD decoder is implemented without the knowledge of the CSI and a 5 dB coding loss when the CSI is not known. A theoretical upper bound is also derived for the permutation-based STSK scheme in order to validate the simulations.

## 1.1 Research Question and Contributions

The research question and sub-questions are described as follows:

**What are the impacts, in terms of bit error rate, computational complexity and code rate, of applying permutation modulation and soft-decision decoding techniques over visible light and hybrid powerline visible light channels?**

**1. What is the channel model that describes the error distribution in a cascaded, AF PLC-VLC channel in an indoor environment?**

In this thesis, an indoor testbed which consists of an AF PLC-VLC channel is setup with software-defined radios [22, 26] which perform digital to analog and analog to digital conversion at the transmitter and receiver respectively. With multicarrier OFDM and BPSK modulation, the error sequence from the received bits are then used to derive probabilistic models using a Markov model that combines the Fritchman 3-state model with the Baum-Welch algorithm for steady state transition. In order to validate the suitability of the derived models, a re-estimation algorithm is used along with the derived state transition probabilities, to generate error-free runs (EFR) and error probabilities ( $P_e$ ) which match the EFR and  $P_e$  obtained from the actual cascaded channels.

**2. Can optimization algorithms be applied as soft-decision decoders to PTC in order to mitigate the effects of impulse noise and narrowband interference by increasing the BER performance?**

A permutation codeword of length  $L$  repeats  $M$ FSK symbols  $L$  times. Due to the combinatorial property of the codeword, all the  $M$  frequencies are used using a unique combination. In order for the receiver to determine the likely transmitted codeword or frequency combination, the channel output can be interpreted as an assignment problem. Optimization algorithms can then be used to detect the received samples. In [27] and chapter 4, the novel iterative soft-decision decoder uses the Hungarian algorithm for the first iteration and Murty algorithm for subsequent iterations. A novel branch and bound method is also used for soft-decision detection. Results show that the iterative decoder gives better performance in the additive white Gaussian noise (AWGN), Rayleigh and PLC [28] channels when compared to the hard decision decoder. The computational complexity of the soft-decision decoder is also much reduced when compared with the hard decision's complexity.

**3. Can combinatorial optimization algorithms be used to design STSK transmitters and soft-decision detectors for MIMO VLC? Can the data rate of combinatorial-based STSK MIMO VLC be increased?**

Differential spatial modulation's transmitting matrices use permutations in their construction. Permutation modulation-aided STSK transmit matrices in [29] are also constructed in a similar manner. The iterative soft-decision decoder adapted from [27] is then used to decode the received matrix without the knowledge of the channel gain coefficients. Further work in this thesis creates multiweight codeword matrices by combining permutation codewords which have the highest possible Hamming distance between them. With this novel concept, the amount of information a permutation modulation-aided STSK transmit matrix can convey is significantly increased. Then, soft-decision detection methods are formulated in [29] and an expression for the upper bound of the maximum likelihood performance is derived in Chapter 8.

## Background Review

The role of the power grid is evolving from electricity supply for buildings to further supporting the communication infrastructure required for connected devices. This evolution places a demand on current and future infrastructure to be smart and dynamic enough to adapt to fast digital innovation. Therefore, power grids are becoming smarter by additionally providing communication links to the devices connected to them while also providing communication among the devices on the power network. Therefore, home appliances powered by electricity are automatically on a data network, enabled by PLC while electric vehicles are also able to communicate with the grid. For an indoor scenario such as illustrated in Fig. 2.1 where low-voltage appliances become part of the IoT network, the ability to use existing infrastructure to provide data communication becomes attractive. This is because, with minimal changes to the installations in the building, devices are capable of sending data to one another and to the grid.

The realization of efficient communication in smart grids therefore, relies on the success of reliable communication using the PLC channel. The PLC channel is however, a hostile channel because neither the powerline cables nor the power network is designed to cater for communication signals. As a result, normal activities in an indoor environment such as plugging or unplugging a device from the powerline introduces impulses into the channel, interpreted as noise to the information signal. Since such man-made interference is unpredictable, it is important to understand the statistical distribution of the noise in order to inform modulation and error correction techniques that are suitable and adaptive for error mitigation. Noise can be modelled as either memoryless or with memory. For a channel

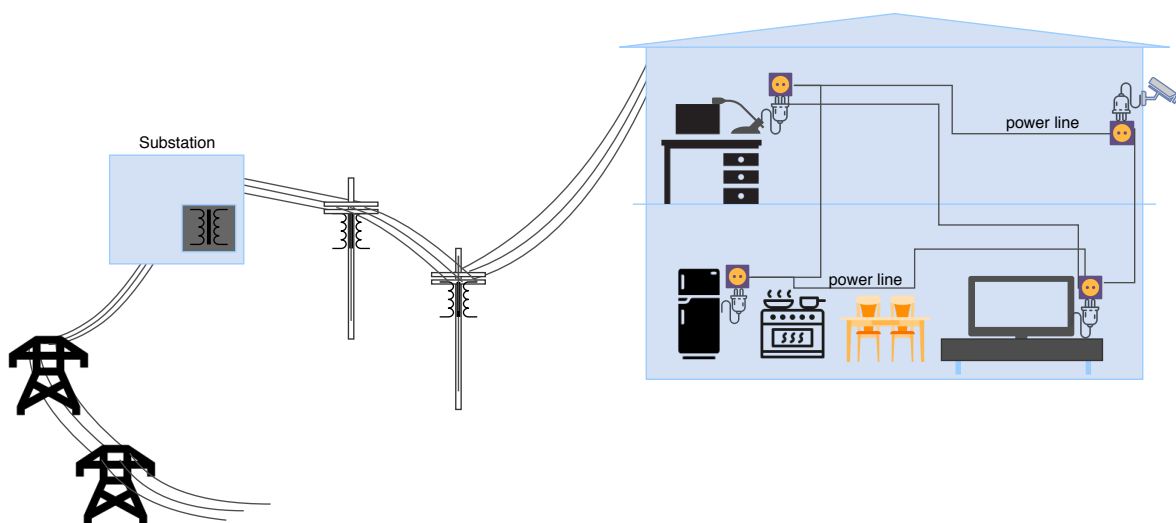


FIGURE 2.1: Connection between the grid to a smart home with powerline also serving as a data communication link.

with memory, the statistical representation of the channel at its current state relies on the channel's previous state or states. A memoryless channel on the other hand, considers the current state of the channel as independent of previous states but considers the occurrence of noise to follow a statistical distribution.

## 2.1 Memoryless PLC and VLC Channel

In order to model a memoryless channel, the physical properties and signal parameters are considered in order to find the statistical distribution that best describes the behavior of the noise. While it is often impossible to consider all possible parameters, the derived model provides an approximation of the actual channel. The memoryless PLC channel is summarized to be characterized by background noise, IN, narrowband interference (NBI) and signal attenuation with distance. While background noise can be modelled as having a Gaussian distribution, IN is dominant in the narrowband (NB) range of 3-500 kHz and broadband range of 1.8-250 MHz. In later sections, we will consider the multipath channel model that describes the signal attenuation with distance and frequency, the statistical representation of the channel and the effect on single carrier and multicarrier modulation schemes.

### 2.1.1 Multipath Channel Model for PLC

An indoor powerline wiring is usually not a point-to-point, direct link between the source and destination. Rather, it commonly consists of branches to satisfy the power requirements of the building. Therefore, the signal from the source flows across all the branches of the channel. This 'bus' topology means the signal flows to all branches in the channel can be received at any point in the branches. The signal therefore, propagates in a multipath model [30], hence the attenuation and delay experienced in each branch of the channel may be different. Consider the PLC network with three branches in Fig. 2.2 where the transmitter and receiver are placed at point A and C respectively and the impedance at both points are matched. From the three branches, several paths can be drawn as indicated by the arrows showing the direction of flow of the signal. An example path is the direct  $A \rightarrow B \rightarrow C$  path while a longer path is for the signal to arrive at the receiver is  $A \rightarrow B \rightarrow D \rightarrow B \rightarrow C$ .

The frequency response of the signal arriving at point C from A is influenced by the dominant paths  $j = 1, 2, \dots, J$ , the length  $d_j$ , delay  $\tau_j$  and the weighting factor  $g_j$  in each path  $j$ . In order to model the attenuation along each path,  $J$  dominant paths whose signal amplitude contribute significantly to the overall received signal can be considered. Signals having negligible amplitude due to longer path lengths can be ignored. The attenuation in each path as a function of the frequency and distance is therefore derived as [30]

$$K(f, d_i) = e^{-(\kappa_0 + \kappa_1 f^k) d_i}, \quad (2.1)$$

where  $k$  is the exponent of the attenuation factor which takes values between 0.5 and 1,  $\kappa_0$  is the initial attenuation and  $\kappa_1$  is the attenuation which increases with frequency and are all obtained from the measured transfer functions linked to the cable parameters. The time delay experienced by the signal along the path it travels is represented as

$$\tau_i = \frac{d_i \sqrt{\epsilon}}{c}, \quad (2.2)$$

where  $\epsilon$  represents the dielectric constant of the insulating material of the cable and  $c$  is the speed of light. Considering the weighting factor  $g_i$  of each path and using (2.1) and (2.2), the frequency response of the signal arriving at C from A is therefore represented as

$$H(f) = \sum_{i=1}^N g_i \cdot K(f, d_i) \cdot e^{-j2\pi f \tau_i}. \quad (2.3)$$

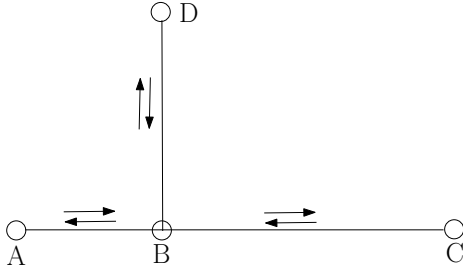


FIGURE 2.2: PLC network illustrating multipath model in the branches.

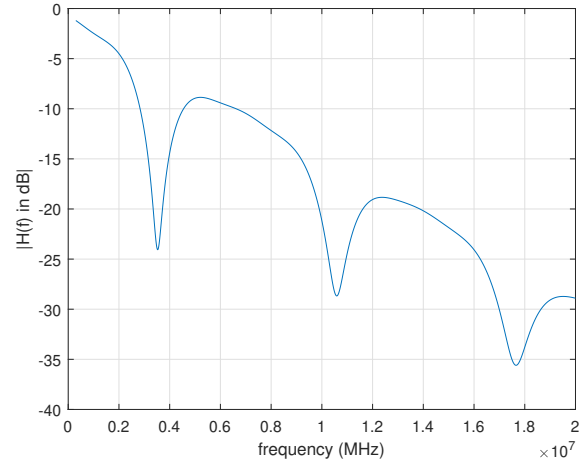


FIGURE 2.3: Amplitude response for  $N = 4$ .

TABLE 2.1: PLC parameters for  $N = 4$  paths

$i$	$g_i$	$d_i$
1	0.64	200
2	0.38	222.4
3	-0.15	244.8
4	0.05	267.5

The parameter  $g_i$  is the weighting factor and is obtained from the product of the reflection factor and transmission factor of each transmission path in Fig. 2.2. Fig. 2.3 shows the frequency response for 4 paths and assumes a copper cable with  $\epsilon = 3.6$ . The path lengths and each path's weighting factor are given in Table 2.1.

### 2.1.2 Middleton Class A Noise Model for PLC

Noise is also introduced into the PLC channel as a result of devices plugged into the channel or voltages from switching transients. This type of noise is introduced into the channel as impulses of high amplitude and their occurrence is successive, persisting for a short period of time. These bursts of impulses may affect a set of frequencies such as in the NB region. This form of NBI may occur for a short period, affecting the information transmitted across the channel at a certain timeslot. If the impulses are measured in the time domain, successive information bits are affected irrespective of the frequency used in transmitting the information.

In this case, the powerline channel is modelled as a combination of background noise and IN. The Middleton Class A noise model [31,32] is sufficient to describe such PLC noise. The probability density function (PDF) of the channel is therefore not entirely Gaussian but can be described by the frequency of occurrence of the impulses  $\Lambda$ , the variance of the impulses  $\sigma_1^2$  and the ratio between the variance of the Gaussian noise and IN  $\Phi = \frac{\sigma_G^2}{\sigma_1^2}$ . The probability  $P(\epsilon > \epsilon_0)$  of receiving a signal whose envelope  $\epsilon$  exceeds the transmitted envelope  $\epsilon_0$  as a result of the occurrence of IN and Gaussian noise is given as

$$P_1(\epsilon > \epsilon_0) \cong e^{-\Lambda} \sum_{m=0}^{\infty} \frac{\Lambda^m}{m!} e^{-\frac{\epsilon_0^2}{2\sigma_m^2}}, \quad \text{for } 0 \leq \epsilon_0 < \infty. \quad (2.4)$$

Therefore, solving  $w_1 = -\frac{dP_1}{d\epsilon_0} |_{\epsilon_0 \rightarrow \epsilon}$  evaluates the PDF as

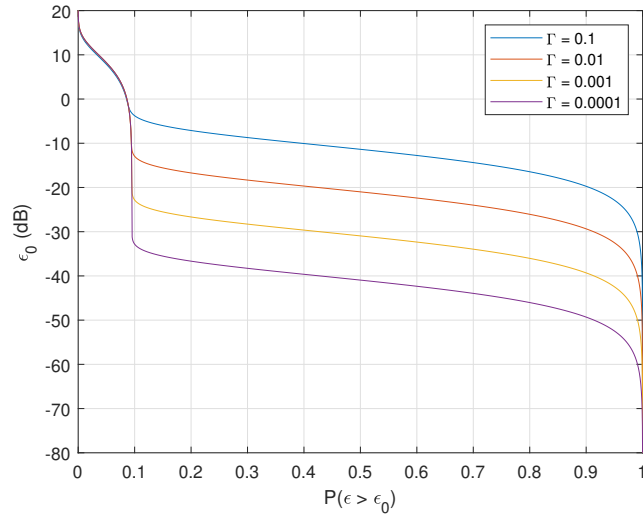
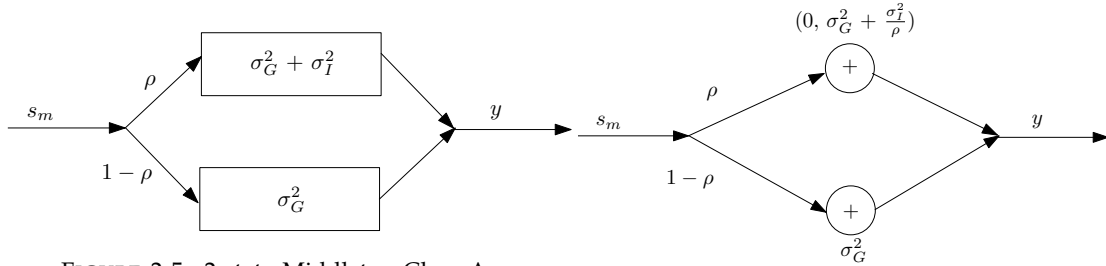
FIGURE 2.4: Envelope distribution for  $\Lambda = 0.1$ .

FIGURE 2.5: 2-state Middleton Class A noise model.

FIGURE 2.6: 2-state Bernoulli-Gaussian noise model.

$$w_1(\epsilon) \cong e^{-\Lambda} \sum_{m=0}^{\infty} \frac{\Lambda^m}{m! \sigma_m^2} e^{-\frac{\epsilon}{2\sigma_m^2}}, \quad \text{for } 0 \leq \epsilon < \infty, \quad (2.5)$$

where  $\sigma_m^2 = 2\hat{\sigma}_m^2 = \frac{m+\Lambda\Phi}{\Lambda(1+\Phi)}$ ,  $\sigma_G^2$  and  $\sigma_I^2$  have distributions  $\mathcal{N}(0, \sigma_G^2)$  and  $\mathcal{N}(0, \sigma_I^2)$  respectively.

Fig. 2.4 shows the probability of  $\epsilon$  exceeding the transmitted envelope  $\epsilon_0$  for different  $\epsilon_0$  levels and different values of  $\Phi$  at  $\Lambda = 0.1$ . The plot shows the probability  $P_{1-\Lambda}$  of the Class A model follows the Rayleigh probability distribution's weighted sum.

As illustrated in the 2-state model in Fig. 2.5, IN is not constant over the channel but occurs within short periods and the occurrence can be determined using a certain probability. The occurrence of IN can therefore be modelled as independent random variables whose occurrence follows the Poisson distribution [31]. Therefore, each PLC noise sample at the output of the channel can be defined as

$$z_{\text{PLC}} = z_G + z_I \sqrt{\delta}. \quad (2.6)$$

Here,  $z_G$  is random complex, zero mean Gaussian distributed variable with variance of  $\sigma_G^2 = 2N_0$  for each complex component. The occurrence of IN is defined by the sequence  $\delta$  with a Poisson distribution and impulsive index  $\Lambda$  which determines the frequency of occurrence of the zero mean, Gaussian sequence  $z_I$  with variance of  $\frac{\sigma_G^2}{\Lambda}$ .

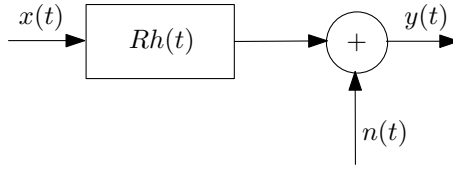


FIGURE 2.7: Block diagram of an optical communication system in baseband.

### 2.1.3 Bernoulli-Gaussian Noise Model for PLC

The Bernoulli-Gaussian model [33, 34] is similar to the Middleton Class A but as shown in Fig. 2.6, both states have a Gaussian distribution with zero mean. The Gaussian state has a variance of  $\sigma_G^2$  while the state with both impulse and Gaussian noise has a variance of  $\sigma_G^2 + \sigma_I^2/p$ . The PDF of the model is defined as

$$F_{bg}(n_k) = (1 - p)\mathcal{N}(n_k : 0, \sigma_G^2) + p\mathcal{N}(n_k : 0, \sigma_G^2 + \sigma_I^2). \quad (2.7)$$

### 2.1.4 VLC Channel Model

The VLC channel behavior can be simply characterized using either an indoor and outdoor environment. A simple communication technique uses the intensity of the light to manipulate the data for transmission while the receiver implements direct detection (DD) [35]. This method is common due to its simplicity of implementation and cost-effectiveness. Intensity modulation (IM) maps the power of the optical beam from the light source, to the data at the transmitter. At the same time, the receiver uses a photodetector to generate a photocurrent that corresponds to the received power intensity. The nature of IM implies the transmitted signal cannot be negative.

A simple flow diagram in Fig. 2.7 describes the baseband model where  $R$  represents how responsive the photodetector is,  $h(t)$  represents the impulse response of the channel at baseband and  $n(t)$  is introduced into the system from the components in the communication device and is modelled as a random Gaussian process with power spectral density  $N_0/2$ .  $n(t)$  can also be considered as shot noise.  $y(t)$  is expressed as

$$y(t) = Rx(t) \otimes h(t) + n(t), \quad (2.8)$$

where  $\otimes$  represents the convolution operation.  $h(t)$  is modelled in [2] as

$$h(t) = \begin{cases} \frac{2t_0}{t^3 \sin^2(\text{FOV})}, & \text{if } t_0 \leq t \leq \frac{t_0}{\cos(\text{FOV})} \\ 0, & \text{elsewhere,} \end{cases} \quad (2.9)$$

where FOV is the field-of-view (FOV) and  $t_0$  represents the minimum delay.

#### 2.1.4.1 Indoor VLC Channel Model

The length of the channel in an indoor environment is considerably small, for example, the distance between the ceiling and a receiver module on the table. The DC gain of the channel  $H(0)$  is a function of the channel impulse response  $h(t)$  and is defined as

$$H(0) = \int_{-\infty}^{\infty} h(t)dt, \quad (2.10)$$

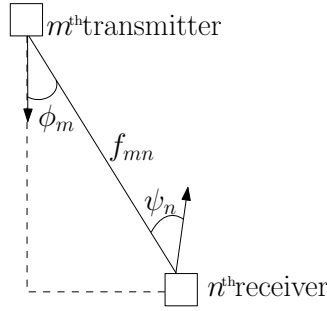


FIGURE 2.8: Geometric model of transmitter LED and receiver PD.

and the SNR is a function of the average power of the received squared optical power  $P_r$  and is directly proportional such that

$$\text{SNR} = \frac{R_{\text{PD}}^2 H^2(0) P_r^2}{R_b N_0}, \quad (2.11)$$

where  $N_0$  is the power spectral density (PSD) of the noise and  $R_{\text{PD}}$  is the PD's responsiveness value.

The received signal's DC gain in an indoor setup with considerably short distance  $f_{mn}$  and a Lambertian source transmitter pointing at an angle  $\phi$  as shown in Fig. 2.8 is given as

$$H_{\text{los}}(0) = \begin{cases} \frac{(b+1)A_{\text{PD}}}{2\pi f_{mn}^2} \cos^b(\phi_m) \cos(\psi_n), & \text{for } 0 \leq \psi_n \leq \Psi_c \\ 0, & \psi_n > \Psi_c, \end{cases} \quad (2.12)$$

where the Lambertian emission order  $b = \frac{-\ln 2}{\ln(\cos \Phi_{1/2})}$  for a semi-angle  $\Phi_{1/2}$ ,  $A_{\text{PD}}$  describes the area of the  $n$ -th PD,  $f_{mn}$  is the distance between the  $m$ -th LED and the  $n$ -th PD,  $\phi_m$  and  $\psi_n$  are the transmitter's and receiver's angle of incidence respectively while  $\Psi_c$  is the receiver's FOV. This model enables the measurement of the amount of power attenuation of the received signal by calculating the received power which is given as

$$W_{r-\text{los}} = H_{\text{los}}(0) W_t. \quad (2.13)$$

for a transmitted power  $W_t$ . A plot of  $H_{\text{los}}$  is shown in Fig. (2.9) with  $m_1 = 1$  at and angle  $\phi_p = 10^\circ$ . The center of the room where the LED has a direct transmission has the highest received power of about 21 dBm

#### 2.1.4.2 VLC Transmitter using Summing Amplifier

Consider a VLC transmitter which modulates the intensity of an LED with the analog signal generated by the USRP [22, 26, 36]. The transmitter consists of a simple voltage adder circuit with two inputs as shown in Fig 2.10. One input conveys the modulated analog signal from the USRP while the other input conveys a direct current (DC) voltage. The output is the analog signal with a DC bias and simultaneously amplified by a gain

$$A_v = \frac{R_3 + R_4}{R_3}. \quad (2.14)$$

The DC bias is applied such that it can drive the LED while the amplification is chosen such that the total peak voltage of the signal does not saturate the operational amplifier (OP-AMP). In the case of a laser diode, the modulated analog signal is DC-biased using a bias-Tee which is suitable for higher frequencies.

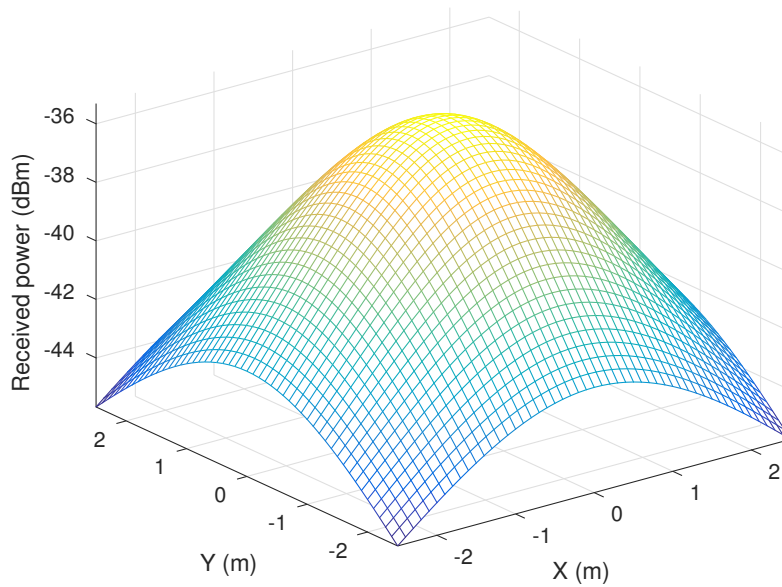
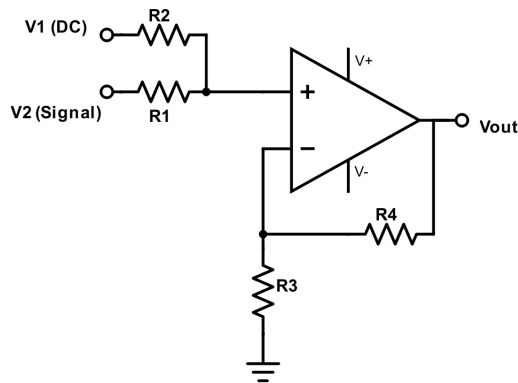
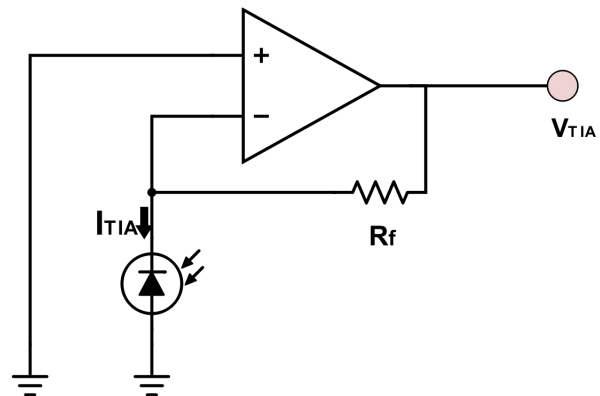
FIGURE 2.9: LOS channel gain with  $\phi = 10^\circ$ ,  $d = 2$  m.

FIGURE 2.10: Voltage adder circuit to supply DC bias and amplification to the transmitted signal.

FIGURE 2.11: Transimpedance amplifier to convert photodiode current  $I_{TIA}$  to voltage.

### 2.1.4.3 VLC Receiver using Transimpedance Amplifier

At the receiver, DD of the intensity-modulated LED signal is employed using a photodiode and transimpedance amplifier (TIA) [37] as shown in Fig. 2.11. The photodiode generates a current  $I_{TIA}$  as a result of the changes in the intensity of the LED. These changes in intensity are read as currents which are then converted to a corresponding voltage by the TIA such that

$$V_{TIA} = I_{TIA} \times R_f. \quad (2.15)$$

The voltage  $V_{TIA}$  is then converted to a digital signal by the USRP for further post-processing.

## 2.2 Memory, Discrete Channel Modelling

Communication systems utilize waveforms to transmit and receive information across the communication channel. This process can be quantized into its equivalent, discrete form such that the samples of the waveform to be transmitted are mapped into discrete data or binary numbers. The receiver however, receives a waveform which consists of the transmitted signal but in a rather degraded form due to interference, attenuation and noise. The receiver samples the received waveform into its discrete equivalent and attempts to reconstruct the transmitted message. This transmitted signal could be pre-processed using automatic gain control, synchronization, scrambling and interleaving while the received signal could be post-processed using equalization, de-interleaving, frequency compensation, automatic gain control, synchronization and de-scrambling as the case requires.

As a result of the degradation experienced by the signal, the received signal differs from the transmitted message and this varies with the degree of severity of the channel. Therefore, the difference between the transmitted and received is of interest in order to derive a channel model that describes the situation within the channel. The transmitted waveform can be sampled and mapped into a sequence of discrete symbols of vector  $\mathbf{x} = (x_1, x_2, \dots, x_K)$  while the received, sampled waveform is mapped into a sequence of vector  $\mathbf{y} = (y_1, y_2, \dots, y_K)$ . The error sequence  $\mathbf{e} = \mathbf{y} - \mathbf{x}$  contains information about the channel's state at each interval. The channel is in an error-free state when  $e_k = 0$  while the channel is in an error state when  $e_k = 1$  for  $k = 1, 2, \dots, K$ . The probability  $\text{Pr}(i)$  of the channel will be found in state  $i$  is given as  $\pi_i$  and for  $N$  states,  $\Pi = [\pi_1, \dots, \pi_N]$ . A first order Markov model considers only one previous interval ( $k - 1$ ), and by observing an error sequence, it can be inferred the channel transitions between states when  $e_t \neq e_{t+1}$ . The channel remains in the same state when  $e_k = e_{k+1}$ . This transition probability matrix  $A = [a_{ij}]$  describes this transition between any two states of the  $N$  states such that

$$A = \begin{bmatrix} a_{11} & a_{12} & \dots & a_{1N} \\ a_{21} & a_{22} & \dots & a_{2N} \\ \vdots & \vdots & \ddots & \vdots \\ a_{N1} & a_{N2} & \dots & a_{NN} \end{bmatrix}. \quad (2.16)$$

The emission probabilities  $B = [mn]$  ( $m = 1, 2, \dots, M, n = 1, 2, \dots, N$ ) describe the probability of the model making a wrong or right decision when the channel is in a given state and is described by the matrix

$$B = \begin{bmatrix} b_{11} & b_{12} & \dots & b_{1N} \\ b_{21} & b_{22} & \dots & b_{2N} \\ \vdots & \vdots & \ddots & \vdots \\ b_{M1} & b_{M2} & \dots & b_{MN} \end{bmatrix}. \quad (2.17)$$

Therefore, the Markov channel model estimates the maximum likelihood model parameters ( $A, B, \Pi$ ) which can be used to generate error sequences with error-free distributions similar to the distribution of the measured sequences.

## 2.3 Coding and Modulation

In analog and digital transmission of data through channels, the data is converted to a form that is suitable for the channel to transmit the data, a process generally known as modulation. The type of modulation technique used usually depends on the nature of the channel, the overall design of the system among other factors. The amount of bandwidth available for example, can influence the choice of the modulation technique.

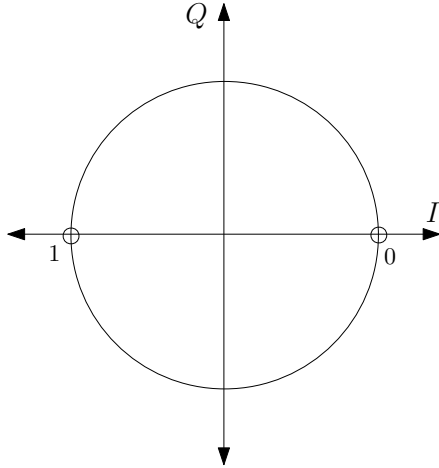


FIGURE 2.12: BPSK constellation

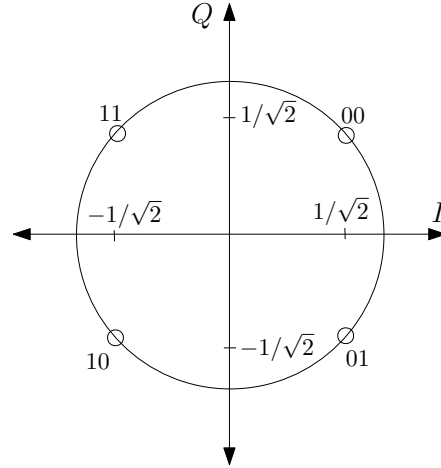


FIGURE 2.13: 4-PSK constellation

### 2.3.1 Phase Shift Keying (PSK)

Phase shift keying (PSK) uniquely maps a signal's digital representation to the phase such that the signal's phase is changed when modulated. The simplest form of PSK is binary PSK (BPSK) such that a '0' is mapped to a phase, say  $0^\circ$  while a '1' is mapped to  $180^\circ$ . In general,  $M$ -PSK modulation uniquely maps each binary symbol of length  $\log_2 M$  to one of  $M$  equally separated phases.

The modulation in BPSK is done such that the transmitted signal

$$s(t) = \sqrt{2E/T} \cos(2\pi ft + \pi(1 - n)), \quad \text{for } n = 0, 1, \quad (2.18)$$

where  $E$  is the power of the signal and  $T$  is the bit duration. Therefore, a '0' will be modulated as

$$s_0(t) = \sqrt{2E/T} \cos(2\pi ft + \pi), \quad (2.19)$$

while a '1' will be modulated as

$$s_1(t) = \sqrt{2E/T} \cos(2\pi ft), \quad (2.20)$$

with a phase difference of  $180^\circ$  between the two signals as shown in the constellation diagrams in Fig. 2.12. Higher order constellation in Fig. 2.13 shows a QPSK constellation with the mapping of the input bits with respect to the In-phase (I) and Quadrature (Q) channels. The probability of error for BPSK in an additive white Gaussian noise (AWGN) channel is defined as [38]

$$P_{e,B} = Q\left(\sqrt{\frac{2E_b}{N_0}}\right), \quad (2.21)$$

where  $Q(x) = \frac{1}{2} \int_x^\infty \exp(-\frac{u^2}{2})$  and  $E_b/N_0$  is the signal to noise ratio (SNR) per bit for bit energy  $E_b$  and noise spectral density  $N_0$ .

### 2.3.2 Pulse Amplitude Modulation

Pulse amplitude modulation (PAM) is a multi-level OOK modulation that maps the incoming bits onto the amplitude of a pulse as shown in Fig. 2.14. PAM is attractive for VLC because it can be used to modulate incoming bits into real and positive signals which are required for transmission over VLC. Gray coding can be used to map the incoming bits into an  $M$ -PAM constellation, similar to a conventional  $M$ -PSK or  $M$ -ary quadrature amplitude modulation ( $M$ -QAM) mapping. In a line-of-sight (LOS) VLC using unipolar PAM, the probability of error is defined as [39,40]

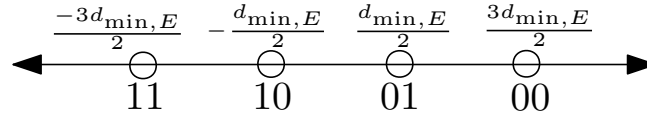


FIGURE 2.14: Gray-coded 4-PAM constellation mapping

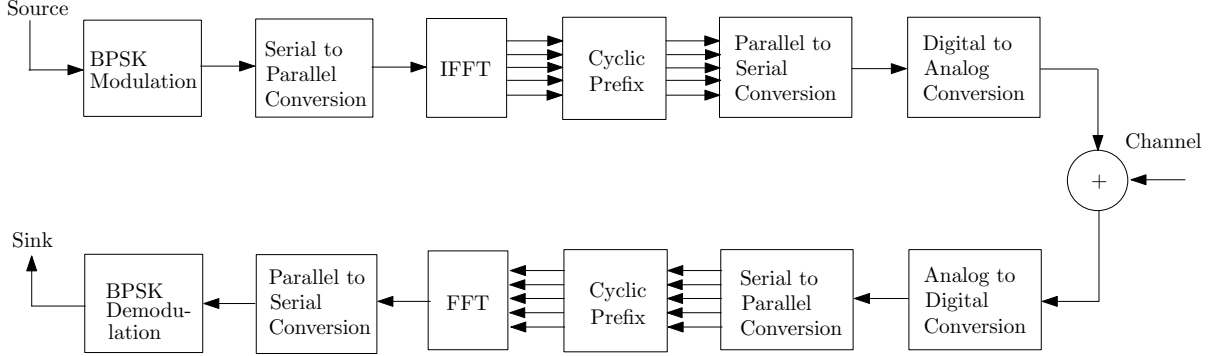


FIGURE 2.15: OFDM flow diagram.

$$P_{e,\text{PAM}} = \frac{2(M-1)}{M} Q \left( \sqrt{\frac{E_b}{N_0} \frac{3 \log_2 M}{(M-1)(2M-1)}} \right), \quad (2.22)$$

where  $E_b/N_0$  is the average electrical energy to noise ratio and  $d_{\min,E}$  is the Euclidean distance between the constellation points and is defined as

$$d_{\min,E} = \sqrt{\frac{6E_b \log_2 M}{(M-1)(2M-1)}}. \quad (2.23)$$

### 2.3.3 Orthogonal Frequency Division Multiplexing (OFDM)

OFDM utilizes subcarriers which are signals orthogonal to one another to transmit messages simultaneously across parallel channels. Each subcarrier frequency is mapped one-to-one onto each channel. The signals to be transmitted are distributed along the available subcarrier frequencies that are orthogonal to one another. By centering the signals around their allocated orthogonal frequencies, the signals in the frequency domain appear to be overlapping signals yet not interfering with one another. This can be visualized as a multi-dimensional space in which the number of subcarriers is the number of dimensions. Therefore, the carrier frequencies can occupy the same bandwidth with the same symbol duration without inter-symbol interference (ISI). This method allows data to be closely packed without experiencing ISI that can occur as a result of delay spread that could occur from multipath channels. Fig. 2.15 shows the steps involved when BPSK symbols are modulated onto predefined OFDM subcarriers, to be transmitted over a channel.

The transmitted signals are centered around the carrier frequency of the subcarrier in which the signal is assigned and separated by guard bands in the frequency domain. OFDM is able to transmit at lower symbol rates in each sub-channel rather than transmit at faster symbol rate in the case of the use of a single channel. Therefore, modulation methods can be utilized with low symbol rate. The multicarrier method also makes room for a longer symbol interval during transmission. The availability of longer symbol times therefore allows the inclusion of symbol guard periods which further mitigates against ISI.

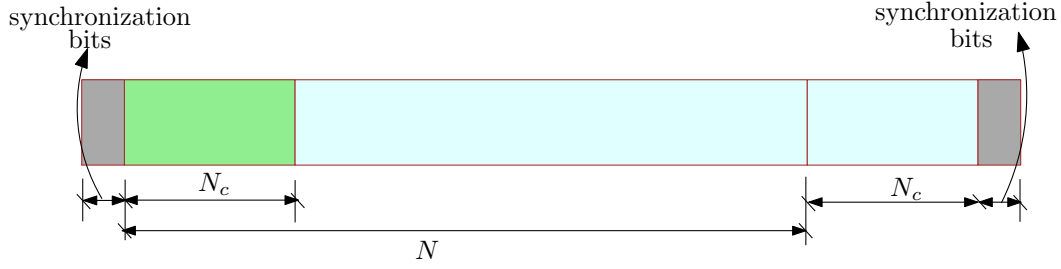


FIGURE 2.16: Synchronized OFDM message structure

### 2.3.3.1 Inverse Fast Fourier Transform

In OFDM, it has been mentioned that  $N$  subcarrier frequencies in parallel are used in conveying signals in order to achieve a higher data rate and mitigate against ISI. To transmit signals at such frequencies, modulation such as BPSK is done per subcarrier to map the incoming bits into their corresponding in-phase and quadrature (IQ) equivalent. This will require  $N$  oscillators each at the transmitter and receiver using traditional RF mixing techniques. Implementing OFDM this way will require complex hardware and high power consumption in order to achieve end-to-end transmission. However, a modern signal processing technique, inverse fast Fourier transform (IFFT) converts the incoming frequency domain signals per subcarrier into their equivalent time domain signal. IFFT sampling is performed above the Nyquist rate and each symbol in the frequency domain is converted into a complex IQ sample in the time domain. The resulting sample is then mapped onto the constellation of a modulation scheme such as BPSK. Digital to analog conversion (DAC) is then performed on the IFFT sample in the universal software-defined radio peripheral (USRP).

### 2.3.3.2 Cyclic Prefix

The cyclic prefix process places a copy of the end of the OFDM symbol into the period occupied by the guard interval. Fig. 2.16 shows a copy of the message portion of symbol period  $N_c$  prepended to the message. Guard bands are utilized in frequency division multiplexing (FDM) in order to space out successive signals apart from each other in the time domain in order to preserve the symbol duration and prevent inter-carrier interference. However, severe multipath channel characteristics over a long period of time causes successive signals to overlap in the frequency domain, causing inter-symbol and inter-carrier interference. This also affects the orthogonality of subcarriers as the severity of the channel increases. In order to mitigate against successive OFDM carriers from overlapping, samples from the end of the IFFT time domain samples of a symbol period are prepended to the symbol duration. With the use of guard bands, a pulse shaping filter is no longer needed.

## 2.3.4 Permutation Codes with $M$ -ary Frequency Shift Keying

Permutation codes are non-binary codes in which the codebook  $\mathcal{C}$  is a subset of codebook  $\mathcal{P}$  and each codeword  $\mathbf{c}_q$  ( $q = 1, 2, \dots, |\mathcal{C}|$ ) is a row vector [41], where  $|\mathcal{C}|$  is the cardinality.  $\mathcal{P}$  is a permutation of all integers in  $v = \{v_1, v_2, \dots, v_L\}$  and  $\mathcal{C}$  is selected to maximize the minimum Hamming distance  $d_{\min}$  of the codebook. The Hamming distance  $d_m(v_1, v_2)$  between any two codewords in  $\mathcal{C}$  is the number of places the two codewords differ in an element-by-element comparison. The minimum  $d_H$  of  $\mathcal{C}$  is defined as [42]

$$d_{\min} = \min\{d_H(\mathbf{c}_q, \mathbf{c}_{q+1}) : \mathbf{c}_q, \mathbf{c}_{q+1} \in \mathcal{C}, \mathbf{c}_q \neq \mathbf{c}_{q+1}, q = 1, 2, \dots, |\mathcal{C}|\}. \quad (2.24)$$

The coderate  $R$  of  $\mathcal{C}$  is defined as

$$R = \frac{\log_2(|\mathcal{C}|)}{L \log_2(L)}, \quad (2.25)$$

where  $|\mathcal{C}|$  is the number of codewords in  $\mathcal{C}$  and  $L$  is the length of each codeword.

Permutation codes can also be used as a modulation scheme [41] or combined with convolutional codes [43] by mapping the output of the convolutional encoder to a codeword in  $\mathcal{C}$ .  $\mathcal{C}$ , in this case is chosen such that the mapping either preserves or increases  $d_H$  [23]. This method is applied in the powerline channel using  $M$ -FSK [38] to combat narrowband interference as well as background and IN [44].

$M$ -ary frequency shift keying ( $M$ -FSK) modulates by mapping the signals onto a set of signals with frequencies chosen such that the carrier waveforms are orthogonal to one another [38]. In (2.26),  $f_i$  is a set of orthogonal carrier frequencies

$$s(t) = A \cos(2\pi f_i t + \theta). \quad (2.26)$$

$M$ -FSK can also be represented in vector form as

$$s_i = \begin{cases} \sqrt{E}, & \text{if } f = f_i, \\ 0, & \text{otherwise} \end{cases}. \quad (2.27)$$

Modulating permutation codes with  $M$ -FSK increases the number of symbols that represent the message. This spreads the message across the spectrum, such that impulse interference only affects some parts of the message and not the entire message. The choice of  $\mathcal{C}$  and the decoding algorithm is therefore to optimize the recovery of the noisy message given that some parts of the message is erased or flipped.

### 2.3.5 Permutation Trellis Codes with $M$ -FSK

Permutation trellis codes combine convolutional codes and permutation codes at the encoder and uses a modified Viterbi decoder to decode the demodulated signal. In the PTC, the outer code is a convolutional encoder of rate  $R = k/n$  which outputs  $n$  bits for every  $k$  input bits.

Each  $n$ -tuple is mapped onto a permutation codeword  $c_q$  of length  $L$  whose codebook  $\mathcal{C}$  is a subset of a set of all possible permutations of  $L$  integers. Therefore, the combined coderate is  $k/L$ . The mapping is done such that the Hamming distance between the binary sequences and their respective permutation sequences are increased (as shown in Tables 2.2 and 2.3), preserved or reduced. As an example, in Table 2.2, the matrix  $D = [d_{ij}]$

$$D = \begin{matrix} & \begin{matrix} 00 & 01 & 10 & 11 \end{matrix} \\ \begin{bmatrix} 0 & 1 & 1 & 2 \\ 1 & 0 & 2 & 1 \\ 1 & 2 & 0 & 1 \\ 2 & 1 & 1 & 0 \end{bmatrix} & \begin{matrix} 00 \\ 01 \\ 10 \\ 11 \end{matrix} \end{matrix}, \quad (2.28)$$

TABLE 2.2: Distance increasing mapping (DIM) of binary code of length  $n = 2$  to  $L = 3$  permutation code

Binary Code	Permutation Code
00	231
01	213
10	132
11	123

TABLE 2.3: Distance increasing mapping (DIM) of binary code of length  $n = 3$  to  $L = 4$  permutation code

Binary Code	Permutation Code
000	1234
001	1342
010	1423
011	3241
100	4132
101	2314
110	2431
111	2143

shows the Hamming distance  $d_m$  between each of the binary codes while the matrix  $E = [e_{ij}]$

$$E = \begin{matrix} & \begin{matrix} 231 & 213 & 132 & 123 \end{matrix} \\ \begin{bmatrix} 0 & 2 & 2 & 3 \\ 2 & 0 & 3 & 2 \\ 2 & 3 & 0 & 2 \\ 3 & 2 & 2 & 0 \end{bmatrix} & \begin{matrix} 231 \\ 213 \\ 132 \\ 123 \end{matrix} \end{matrix}, \quad (2.29)$$

shows the Hamming distance between each of the non-binary codes the binary codes are mapped to. By doing an element-by-element comparison between  $D$  and  $E$ , the distance increasing mapping is shown when  $i \neq j$ ,  $e_{ij} = d_{ij} + 1$ .

The advantage of PTC is found in the decoding such that the demodulated sequence is compared with each branch in the trellis of the Viterbi decoder using minimum distance decoding. Therefore, ML decoding is possible while eliminating the permutation sequence decoder.

Consider a set of  $M$  orthogonal signals  $s_1, s_2, \dots, s_M$ , each having one of the  $M$  different frequency components and low pass vector representation [38]

$$\begin{aligned} s_1 &= (\sqrt{E_s}, 0, 0, \dots, 0), \\ s_2 &= (0, \sqrt{E_s}, 0, \dots, 0), \\ &\vdots \\ s_M &= (0, 0, 0, \dots, \sqrt{E_s}), \end{aligned}$$

where  $E_s$  is the symbol energy. The output of the permutation trellis encoder which is modulated using the  $M$  orthogonal vectors is a non-binary sequence. Each symbol in the sequence is modulated with  $M$ -FSK such that it has a one-to-one mapping with an  $M$ -FSK vector  $s_m$  ( $m = 1, 2, \dots, M$ ). Therefore, the non-binary sequence is transmitted as a permutation of all vectors  $s_1, s_2, \dots, s_M$ , each vector

$s_m$  appearing once in every  $M$  blocks. Therefore, it is obvious the permutation sequence utilizes all  $M$  available frequencies.

Assuming the signal is sent via an AWGN channel, it is non-coherently received as

$$\mathbf{r} = e^{j\phi} \mathbf{s} + \mathbf{n}, \quad (2.30)$$

where  $\mathbf{n}$  consists of Gaussian random and complex variables and the parts of the complex value have a variance of  $2N_0$  and zero mean. Using the union bound method [38], the error probability of the Viterbi decoder for convolutional codes is bounded by

$$P_{e,CC} \leq \sum_{d=d_{\text{free}}}^{\infty} a_d P(d), \quad (2.31)$$

where

$$P(d) = \frac{1}{2} \binom{d}{d/2} p^{d/2} (1-p)^{d/2} + \sum_{k=d/2+1}^d \binom{d}{k} p^k (1-p)^{n-k}, \quad (2.32)$$

when  $d$  is even and  $p$  represents the probability of error when the bits in each codeword are transmitted using FSK and non-coherently detected. If  $d$  is odd, the second term in (2.32) is ignored.  $a_d$  describes the paths with Hamming distance  $d$  bits when compared with the transmitted codeword,  $P_2(d)$  describes the probability of the decoded path having Hamming distance of  $d$  bits with the transmitted codeword. The code's free distance  $d_{\text{free}}$  describes the Hamming distance between the all-zero path in the trellis and a trellis path which departs the all-zero path and returns to the all-zero path.

For non-coherent  $M$ -FSK, the probability of symbol error in AWGN is defined as [38]

$$P_{e,\text{MFSK}} = \sum_{n=1}^{M-1} \frac{(-1)^{n+1}}{n+1} \binom{M-1}{n} e^{-\frac{n \log_2 M}{n+1} \frac{E_b}{N_0}}. \quad (2.33)$$

The received signal is demodulated by using a threshold detector in each of the  $M$  demodulators such that values above the threshold are set to '1' while values below the threshold are set to '0'. The trellis decoder uses a Viterbi decoder that compares the Hamming distance between the demodulated non-binary sequence and non-binary codewords on each transition path of the trellis.

### 2.3.6 Single Carrier Modulation for PLC

In the time domain, IN in an indoor environment occurs in short bursts and lasts for a short period of time. Hence, the occurrence may affect successive information-carrying symbols. In the case of NBI, the noise takes a frequency selective nature in which a certain frequency is affected for a certain period of time. Due to the random occurrence and short burst nature of IN, the occurrence of IN is modelled using the Poisson distribution. Hence, the arrival rate  $\gamma$  of IN in units per second is used to model the Poisson process. If each IN occurs at an average duration  $T_{\text{noise}}$ , then an average of  $\gamma T_{\text{noise}}$  samples are affected by IN in 1 second and  $1 - \gamma T_{\text{noise}}$  samples are not affected by IN. Now consider a BPSK modulated system in a PLC channel, the effect of IN gives the probability of error as [45]

$$P_{e,\text{PLC}} = \gamma T_{\text{noise}} P_{e,I} + (1 - \gamma T_{\text{noise}}) P_{e,B}, \quad (2.34)$$

where  $P_{e,I}$  is the BER as a result of IN. Using (2.21), the probability of error in the presence of IN is given as

$$P_{e,I} = Q \left( \sqrt{\frac{2E_b}{N_0 + N_i}} \right), \quad (2.35)$$

showing the effect of the IN power spectral density (PSD)  $N_i$ .

Due to the nature of the noise occurrence, coding and modulation schemes for PLC are designed in order to avoid the bursts in the channel [44]. An example is the use of  $M$ -FSK to hop between frequencies such that each signal is transmitted as

$$s_m(t) = \sqrt{\frac{2E_s}{T_s}} \sin(2\pi f_m t), \quad \text{for } 1 \leq t \leq T, \quad \text{and } f_i = f_0 + \frac{i-1}{T_s}, \quad (2.36)$$

where  $E_s$  is the symbol energy and  $m = 1, 2, \dots, M$ , describing the  $M$  frequencies each representing  $\log_2 M$  bits of information and spaced  $1/T_s$  Hz apart. This modulation provides constant envelope modulation and can provide non-coherent detection in cases where the phase of the signal is not known at the receiver. Therefore, the non-coherent detector uses  $2M$  correlators in which two are used for detecting the signal at the receiver and chooses the signal with the highest envelope. The vector representation of the low pass signal is given as [38]

$$\mathbf{s}_m = (\underbrace{0, \dots, 0}_{m-1}, \sqrt{E_s}, \underbrace{0, \dots, 0}_{M-m})^T, \quad (2.37)$$

where  $(\cdot)^T$  denotes the transpose operation and the symbol energy is in the frequency conveying the information. At the output of the PLC channel,  $\mathbf{s}_m$  is received as

$$\mathbf{r}_{\text{PLC}} = \mathbf{s}_m + \mathbf{z}_{\text{PLC}}. \quad (2.38)$$

As a result, it is evident that the occurrence of frequency selective, NBI may be avoided in time slots where the affected frequency is not carrying information. However, while this advantage is only determined by random information signals, a permutation code can be used to spread the information across the  $M$  frequencies. This type of encoding ensures that information is still present in the other  $M - 1$  frequencies, if for example, one frequency is interfered with. When  $M$ -FSK is combined with permutation codes [23, 27, 44], the information symbols are repeated such that all the  $M$  different frequencies are used. Therefore, using (2.37), a permutation codeword such as (2143) for  $M = 4$  can be represented as

$$\mathbf{S}(T) = \begin{bmatrix} t_1 & t_2 & t_3 & t_4 \\ 0 & 0 & 1 & 0 \\ 0 & 1 & 0 & 0 \\ 1 & 0 & 0 & 0 \\ 0 & 0 & 0 & 1 \end{bmatrix} \begin{matrix} f_1 \\ f_2 \\ f_3 \\ f_4 \end{matrix}, \quad (2.39)$$

where the columns  $t_1, \dots, t_4$  represent the time slots while the rows  $f_1, \dots, f_4$  represent the frequencies and the '1' denotes the active frequency. In a PLC channel, the non-coherent detector is not optimal. A more optimal detector described in [23] sets a threshold of  $0.6\sqrt{E_s}$  such that the received samples above the threshold are set to '1' while samples below the threshold are set to '0'. Using this threshold detector, if IN occurs at a certain time during transmission, all the frequencies may be affected such that  $\mathbf{S}(T)$  is received as  $\mathbf{Y}_1(T)$

$$\mathbf{Y}_1(T) = \begin{bmatrix} t_1 & t_2 & t_3 & t_4 \\ 0 & 0 & 1 & 1 \\ 0 & 1 & 0 & 1 \\ 1 & 0 & 0 & 1 \\ 0 & 0 & 0 & 1 \end{bmatrix} \begin{matrix} f_1 \\ f_2 \\ f_3 \\ f_4 \end{matrix}, \quad (2.40)$$

affecting all the frequencies at time  $t_4$ . Also, the effect of NBI on  $\mathcal{S}(T)$  is shown in  $\mathbf{Y}_N(T)$

$$\mathbf{Y}_N(T) = \begin{bmatrix} t_1 & t_2 & t_3 & t_4 \\ 0 & 0 & 1 & 0 \\ 1 & 1 & 1 & 1 \\ 1 & 0 & 0 & 0 \\ 0 & 0 & 0 & 1 \end{bmatrix} \begin{bmatrix} f_1 \\ f_2 \\ f_3 \\ f_4 \end{bmatrix}, \quad (2.41)$$

where frequency  $f_2$  is affected over a duration of timeslots.

### 2.3.7 Multicarrier Modulation for PLC

It is also important to consider a multicarrier modulation such as OFDM in PLC. This is because while OFDM assists with improving the data rate of the communication system and is used in PLC standards such as G3 [46] and PRIME [47], IN bursts may affect successive OFDM data symbols. The data symbols are modulated using BPSK, QAM or any other conventional modulation technique. The modulated symbols are divided into blocks of  $N$  symbols and each block is represented as  $X_k$ ,  $k = 0, 1, \dots, N - 1$  in the frequency domain. Then,  $X_k$  is converted to the time domain using an  $N$ -point inverse discrete Fourier transform (IDFT) [38]

$$x_n = \frac{1}{\sqrt{N}} \sum_{k=0}^{N-1} X_k e^{j2\pi nk/N}, \quad \text{for } n = 0, 1, \dots, N - 1, \quad (2.42)$$

by multiplying each symbol in  $X_k$  by the corresponding discrete Fourier transform (DFT) vector  $\mathbf{v}_k = [v_{k0}, v_{k1}, \dots, v_{k(N-1)}]$  and each element is represented as

$$\mathbf{v}_{kn} = \frac{1}{\sqrt{N}} e^{j2\pi nk/N}.$$

Therefore,  $x_n$  is received at the output of a PLC channel as

$$r_{\text{PLC},n} = x_n + z_{\text{PLC},n}. \quad (2.43)$$

#### 2.3.7.1 Multicarrier Impulse Noise Model

At the output of the PLC channel, the filtered and sampled OFDM signal from any of the  $N$  subcarriers is expressed as [48]

$$r_n = h \otimes \frac{1}{\sqrt{N}} \sum_{k=0}^{N-1} X_k e^{j2\pi nk/N} + z_n, \quad \text{for } n = 0, 1, \dots, N - 1, \quad (2.44)$$

where  $h$  is the channel's impulse response,  $X_k$  is the transmitted signal and  $z_n$  is the noise described by i.i.d. random variables.

In order to recover the transmitted signal from  $r_n$ , if  $G_n$  is the Fourier transform of  $z_n$  such that

$$G_n = \frac{1}{\sqrt{N}} \sum_{k=0}^{N-1} z_k e^{-j2\pi nk/N}, \quad \text{for } n = 0, 1, \dots, N - 1, \quad (2.45)$$

where  $z_k$  are i.i.d. variables, then the recovered signal  $R_n$  is expressed as

$$R_n = H_n X_n + G_n, \quad \text{for } n = 0, 1, \dots, N - 1, \quad (2.46)$$

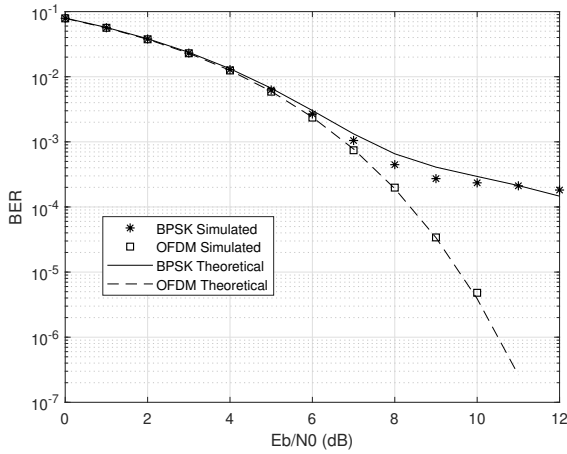


FIGURE 2.17: BPSK and OFDM-BPSK heavily disturbed scenario.

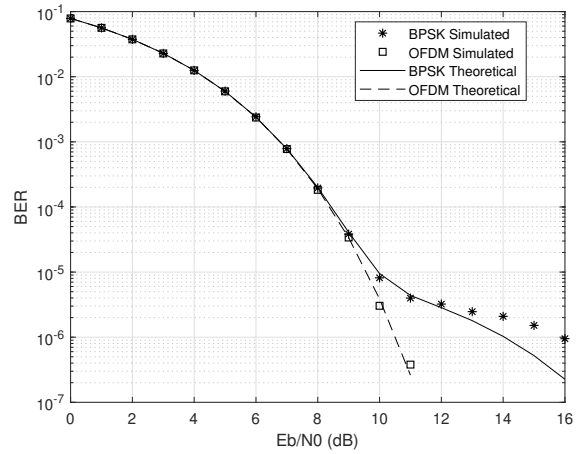


FIGURE 2.18: BPSK and OFDM-BPSK mildly disturbed scenario.

or

$$R_n = \frac{1}{\sqrt{N}} \sum_{k=0}^{N-1} r_k e^{-j2\pi nk/N}, \quad \text{for } n = 0, 1, \dots, N-1, \quad (2.47)$$

where  $H_n$  represents the  $n^{\text{th}}$  sub-channel's transfer function. In the presence of IN, for the same noise duration  $T_{\text{noise}}$  considered in the single carrier BPSK, the DFT operation spreads the noise samples over the  $N$  information symbols. Unlike the single carrier scenario, the total PSD for the OFDM system becomes  $N_0 + \gamma N_i T_{\text{noise}}$ . Therefore, the BER of an OFDM-BPSK scheme becomes

$$P_{e,\text{BMC}} = Q \left( \sqrt{\frac{2E_b}{N_0 + \gamma N_i T_{\text{noise}}}} \right), \quad (2.48)$$

or simplified as

$$P_{e,\text{BMC}} = Q \left( \sqrt{\frac{2E_b/N_0}{1 + A\gamma T_{\text{noise}}}} \right), \quad (2.49)$$

where  $A$  is the ratio between the IN and AWGN noise power.

The advantage of  $M$ -FSK over other modulation schemes such as BPSK is demonstrated in Figs. 2.17 - 2.20 where BER Monte Carlo simulations are used to verify the theoretical BER in (2.34) and (2.48). The inter arrival times (IAT) for the heavily disturbed and mildly disturbed scenarios are 0.0196s and 0.9600s respectively while  $T_{\text{noise}}$  for heavily and mildly disturbed are 0.0641ms and 0.0607ms respectively.  $A = 0.1$  for both scenarios. It is seen that OFDM schemes have better performance at higher SNRs because the effect of the IN is spread over the subcarriers, reducing the overall noise effect.

$M$ -FSK simulations in Figs. 2.19 and 2.20 however, show similar performance for both single carrier and multicarrier scenarios, matching the theoretical BER in (2.33). This is because the  $M$ -FSK scheme in general assists with avoiding noisy parts in the channel since only some of the subcarriers carry information.

### 2.3.8 MIMO Space-Time Shift Keying for VLC

Consider an indoor MIMO VLC system comprising of  $M$  Lambertian LEDs as transmitters and  $N$  photodiodes (PD) as receivers with DC gain  $h_{mn}$  between the  $m$ -th LED and  $n$ -th PD equated as

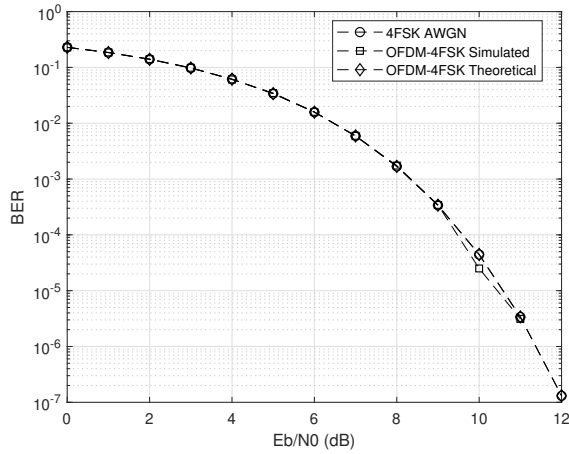


FIGURE 2.19: 4FSK and OFDM-4FSK heavily disturbed scenario.

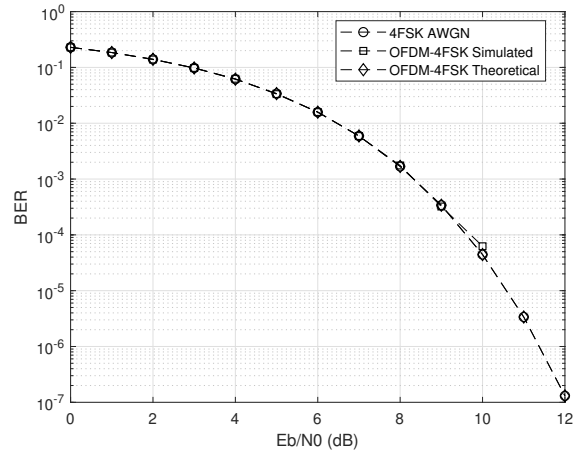


FIGURE 2.20: 4FSK and OFDM-4FSK mildly disturbed scenario.

$h_{mn} = H(0)$ . The source information to be transmitted over the LEDs are mapped to a space-time code block  $\mathbf{S}(i) = s(i) \cdot \mathbf{D}(i)$  where  $i$  represents the index of the block. The signal  $\mathbf{S}(i)$  consists of the constellation point  $s(i)$  from an  $\mathcal{L}$ -PAM or any conventional modulation scheme while  $\mathbf{D}(i)$  is chosen from a set of dispersion matrices  $\mathbf{D}_q (q = 1, 2, \dots, Q)$ . The received signals at the PDs can be modelled as

$$\mathbf{Y}(i) = \mathbf{H}(i)\mathbf{S}(i) + \mathbf{N}(i), \quad (2.50)$$

where  $\mathbf{Y}(i) \in \mathbb{R}^{N \times T}$  is the received signals, each component in  $\mathbf{H}(i) \in \mathbb{R}^{N \times M}$  is described in (2.12),  $\mathbf{S}(i) \in \mathbb{R}^{M \times T}$  describes the permutation-aided space-time signal block and  $\mathbf{N}(i) \in \mathbb{R}^{N \times T}$  models background, shot and thermal noise at the receiver modelled as AWGN with zero mean and variance  $\sigma^2$ .

The ML detector selects the combination  $(q, l)$  representing the input bits that maximizes [49]

$$(q_{\text{ML}}, l_{\text{ML}}) = \arg \max_{\mathbf{S}(i)} P(\mathbf{Y}(i) | \mathbf{S}(i), \mathbf{H}(i)) \quad (2.51)$$

and adapting the ML detection proposed in [49] which finds the  $q$  and  $l$  combination, assuming knowledge of  $\mathbf{H}(i)$

$$(q_{\text{ML}}, l_{\text{ML}}) = \arg \min_{q,l} \|\hat{\mathbf{Y}}(i) - s_l(\hat{\mathbf{H}}(i)\boldsymbol{\zeta}_q)\|^2. \quad (2.52)$$

The expression in (2.52) vectorizes (2.50) such that  $\hat{\mathbf{Y}}(i) = \text{vec}(\mathbf{Y}(i)) \in \mathbb{R}^{NT \times 1}$ ,  $\hat{\mathbf{H}}(i) = \mathbf{I} \otimes \mathbf{H}(i) \in \mathbb{R}^{NT \times MT}$ ,  $\mathbf{I}$  is the identity matrix,  $\otimes$  is the Kronecker product and  $\boldsymbol{\zeta}_q = [\text{vec}(\mathbf{D}_1) \dots \text{vec}(\mathbf{D}_Q)] \in \mathbb{R}^{MT \times Q}$ .

For equiprobable signal matrices, the pairwise error probability (PEP) of receiving a space-time matrix  $\hat{\mathbf{S}}(i)$  when  $\mathbf{S}(i)$  is transmitted, assuming the channel coefficients are known at the receiver is given as [38]

$$P(\hat{\mathbf{S}}(i) \rightarrow \mathbf{S}(i) | \mathbf{H}(i)) \leq Q \left( \sqrt{\frac{E_s}{2N_0} \|\mathbf{H}(i)(\mathbf{S}(i) - \hat{\mathbf{S}}(i))\|_F^2} \right). \quad (2.53)$$

### 2.3.9 Multicarrier Modulation in Hybrid Amplify-and-Forward PLC-VLC

Unlike VLC, OFDM signals for a PLC channel are complex values. From the received sequence at the output of a PLC channel, each sample from the  $N$  subcarriers is expressed as

$$r_{\text{PLC},n} = x_n + z_{\text{PLC},n}. \quad (2.54)$$

If the PLC channel is characterized by background noise and IN [30, 31, 50], then the noise  $z_{\text{PLC},n}$  is defined as

$$z_{\text{PLC},n} = z_{\text{G},n} + z_{\text{I},n} \sqrt{\delta}. \quad (2.55)$$

Here,  $z_{\text{G},n}$  is a random complex, zero mean, Gaussian distributed variable with a variance of  $\sigma_{\text{G}}^2 = 2N_0$  for each complex component. The occurrence of IN is defined by the sequence  $\delta$  with a Poisson distribution and impulsive index  $A$  which determines the frequency of occurrence of the zero mean, Gaussian sequence  $z_{\text{I},n}$  with variance of  $\sigma_{\text{G}}^2/A$ .

In order to transmit  $r_{\text{PLC},n}$  received at the output of the PLC channel, the signal equivalent to each symbol in  $r_{\text{PLC},n}$  is amplified and DC-biased with enough voltage to raise the lowest points of the signal above zero and drive the LED. The amplified and DC-biased signal is then forwarded to the VLC transmitter which will be explained in detail in the next section. Therefore, each sample in the transmitted VLC sequence for the corresponding  $N$  subcarriers from the output of the PLC can be defined as

$$s_{\text{VLC},n} = \alpha r_{\text{PLC},n} + V_{\text{DC}}, \quad (2.56)$$

with an amplification factor of  $\alpha$  and DC bias factor  $V_{\text{DC}}$ . The photodetector is designed such that the surface area collects as much of the incoming signal as possible. A proportional photocurrent is produced by the total optical power or integral of the power detected by the photodetector area [2,35]. The received line-of-sight (LOS) VLC signal can therefore be expressed as

$$r_{\text{VLC},n} = H_{\text{los}}(0) s_{\text{VLC},n} + z_{\text{VLC},n}, \quad (2.57)$$

where  $z_{\text{VLC},n}$  is shot noise that can be modelled as AWGN.

# Indoor Amplify-and-Forward Powerline and Visible Light Communication Channel Model Based on Semi-Hidden Markov Models

---

**This chapter is based on the following publication:** *O. Kolade, A. D. Familua, and L. Cheng, "Indoor Amplify-and-Forward Powerline and Visible Light Communication Channel Model Based on a Semi-Hidden Markov Model." AEÜ - International Journal of Electronics and Communications, p. 153108, Feb 2020.*

The author of this thesis conceptualized the work, performed the experimental measurements, analyzed the data and wrote majority of the paper.

---

## 3.1 Introduction

Communication via visible light such as in light emitting diodes (LEDs) contributes to the promising alternatives to wireless and cable-based communication required for 5G and internet of things (IoT). Naturally, indoor illumination, vehicle lights and other outdoor illumination and signages prefer LEDs due to its long life and low power consumption. Hence, the ability of LEDs to deliver data communication using visible light communication (VLC) in areas where line of sight (LOS) communication is sufficient, provides alternative means of supporting the bandwidth requirements of 5G and IoT. Powerline communication (PLC) on the other hand utilizes the alternating current's wave such as in indoor power cables to convey higher frequency, data signals via the same power cable. Since LED luminaries are lit up by power cable installations, for example, in an indoor environment, LED luminaries can extend their link length to the network backbone or surrounding network architecture using the powerline.

Experimental and theoretical channel models of the memoryless powerline channel show that the powerline noise is not only Gaussian but consists of frequency disturbances, impulsive noise (IN) and signal attenuation with distance [30–32, 51]. IN for example, is observed to occur over a period of time or in bursts, estimated to persist for not longer than 0.1ms [52] and could occur as a result of devices plugged into the channel. Impulses also occur as frequency disturbances, affecting a certain frequency over a period of time. Since the powerline channel exhibits a bus topology in which the different paths in the bus network all convey the signal, each path suffers a different attenuation corresponding to the length of the path [30]. As a result, integrating PLC with VLC using decode-and-forward (DF) [20, 21, 53] methods becomes attractive in order to improve the quality of the attenuated

signal that is forwarded to the VLC transmitter module. Multicarrier modulation schemes can further assist with improving the data rate of the hybrid PLC-VLC setup [16, 17]. However, the performance of DF methods come with increased complexity and additional circuitry and wiring in areas where minimal changes may be required to the existing PLC-VLC integration. The alternative is to forward the PLC signal without demodulating [13, 22, 54] and a further amplification of the PLC signal in the amplify-and-forward (AF) ensures the VLC signal is enough to drive the LED. While AF is more error-prone, it becomes attractive in environments where minimal circuitry changes are required to the existing PLC-VLC circuitry. The theoretical channel model of VLC is assumed to be Gaussian and consists of shot noise and thermal noise [55] generated from the receiver circuitry. Therefore, an AF PLC-VLC setup suggests the noise in the PLC channel is also amplified at the VLC transmitter. For a memoryless, integrated PLC-VLC channel, a simple model which combines the PLC noise with the VLC noise is found in [18]. Furthermore, using the Welch method, a non-parametric approach is used in [19] to model the frequency response of the PLC channel using the number of taps, cable parameters and multipath channel topology similar to [30].

Markov models [56–58] have been used as a convenient technique for modelling channels with memory in order to produce approximate statistical models of the respective channel. For example, Markov models in [59–61] are used to model the bursts in the PLC channel with a derived model that follows the Middleton Class A model found in [62]. A testbed in a controlled environment is the starting point to obtain measurements and the PLC testbed measurements in [61] confirm that noise in the PLC link occurs in bursts. Hence, the Fritchman three-state model in [61] proposes two states to characterize the good state while one state characterizes the events of the channel in an error state. As a result, a semi-hidden Markov model (SHMM) which uses the Fritchman model (FM) [63] is then used to develop an error distribution model of the PLC channel with memory. A similar modelling approach of channels with memory is applied to the VLC channel in [64] with the consideration of pulse width modulation interference. The equivalent DF statistical model using SHMM and FM was obtained in [14] using single carrier modulation which combines frequency shift keying (FSK) with on-off keying (OOK). Furthermore, an AF hybrid PLC-VLC integration in [22] demonstrates the bit error rate for a multicarrier modulation in the hybrid channel. However, a statistical model for the AF hybrid PLC-VLC channel with memory does not exist.

In this paper, the error distribution of the hybrid AF PLC-VLC is obtained using SHMM with the aid of a FM. The measurements are taken using a testbed setup in an indoor office environment. Multicarrier modulation using orthogonal frequency division multiplexing (OFDM) with binary phase shift keying (BPSK) is pre-processed on a computer using MATLAB [65]. The data is then transmitted over a universal software radio peripheral (USRP) N210 [36] transmitter (Tx). The PLC signal is forwarded to the VLC module, amplified enough to drive the LED and transmitted over the LED unit. The receiver photodiode (PD) converts the current from the changing intensity of the LED to a voltage using a trans-impedance amplifier (TIA). The received voltage samples are then converted by the USRP receiver (Rx) and post-processed on a computer to demodulate the samples. The error sequence is then used to derive the steady-state transition probabilities of the channel using the Baum-Welch algorithm [66]. These transition probabilities can then be used to re-generate an approximate, statistical error sequence using the error vector generation algorithm [67]. Error-free run (EFR) distribution plots show that the measured sequences and the re-generated sequences match in most regions and the derived probabilities can be used for channel analysis in terms of suitable parameters of modulation and error correction schemes which can mitigate the effect of the channel noise.

## 3.2 Channel Modelling

Consider a binary sequence  $\mathbf{s} = [s_1, s_2, \dots, s_K]$  representing a message transmitted across the channel. The received bits  $\mathbf{y} = [y_1, y_2, \dots, y_K]$  differ from  $\mathbf{s}$  if there is noise in the channel. Hence, the error sequence  $\mathbf{e} = \mathbf{y} - \mathbf{s}$  describes the difference between the  $\mathbf{y}$  and  $\mathbf{s}$  such that  $e_k = 0$  indicates the bit was received correctly while  $e_k = 1$  for  $k = 1, 2, \dots, K$ , indicates where the bit was received incorrectly.

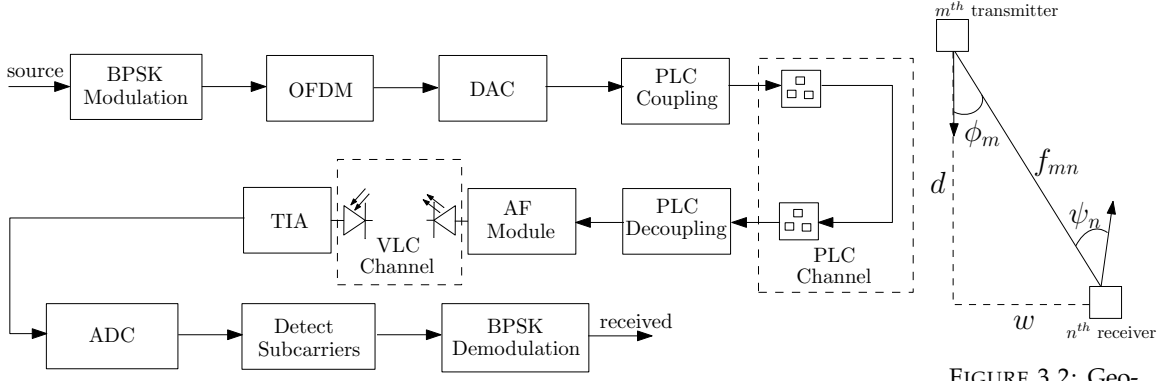


FIGURE 3.1: Block diagram of hybrid AF PLC-VLC

FIGURE 3.2: Geometric model of a Lambertian LED and PD

### 3.2.1 Theoretical Model for PLC and VLC

At the PLC channel, the frequency  $f$  and length  $l_p$  of the path  $p$  travelled by the signal determines the attenuation which is defined as [30]

$$A(f, l_p) = e^{-(u_0 + u_1 f^\rho) l_p}. \quad (3.1)$$

The attenuation factor exponent  $\rho$  consists of values between 0.5 and 1 while  $u_0$  and  $u_1$  are parameters measured from the cable and they describe the initial attenuation and the frequency-related attenuation respectively. Therefore, the frequency response of the received signal is defined as

$$H(f) = \sum_{p=1}^N g_p \cdot A(f, l_p) \cdot e^{-j2\pi f \tau_p}, \quad (3.2)$$

where  $g_p$  is the path's weighting factor and  $\tau_p = \frac{l_p \sqrt{\epsilon}}{c}$  describes the path's delay using the dielectric constant  $\epsilon$  and speed of light  $c$ .

The occurrence of IN in the PLC channel adds to the amplitude of the transmitted signal which is simultaneously affected by background noise generated in the electronic components. Unlike background noise, IN occurs in bursts for a short period of time, hence, the probability  $P(v > v_0)$  of receiving a signal whose envelope  $v$  exceeds the transmitted envelope  $v_0$  can be defined as

$$P(v > v_0) \cong e^{-\kappa} \sum_{\mu=0}^{\infty} \frac{\kappa^\mu}{\mu!} e^{-\frac{v_0^2}{2\sigma_\mu^2}}, \quad \text{for } 0 \leq v_0 < \infty, \quad (3.3)$$

where  $\sigma_\mu^2 = \frac{\mu + \kappa \Gamma}{2\kappa(1 + \Gamma)}$ ,  $\Gamma$  represents the ratio between the background noise power and IN power,  $\kappa$  describes the impulsive index or number of impulses per symbol duration. Since the occurrence of IN is not permanent, it can hence be modelled using the Poisson distribution [31, 32, 50] such that a PLC noise sample at the channel output can be defined as

$$z_{\text{PLC}} = z_G + z_I \sqrt{D}. \quad (3.4)$$

The variables  $z_G$  and  $z_I$  have the respective distributions  $\mathcal{N}(0, \sigma_G^2)$  and  $\mathcal{N}(0, \sigma_I^2)$ , implying zero mean and the variances  $\sigma_G^2$  and  $\sigma_I^2$  represent the Gaussian noise and IN variances respectively. The occurrence of IN is defined by the sequence  $D$  with a Poisson distribution and impulsive index  $\kappa$ .

Fig 3.1 shows a multicarrier system which forwards a PLC signal to a VLC transmitter unit using AF. In the VLC channel, a Lambertian LED and PD follow the geometric model in Fig. 3.2 and the power

in the transmitted signal  $P_{TX}$  is received as

$$P_{RX} = hP_{TX}. \quad (3.5)$$

Here,  $h$  is the attenuation factor of the direct line-of-sight (LOS) between the transmitter and receiver and is given as [55]

$$h = \begin{cases} \frac{A_R(m_L+1)}{2\pi d^2} \cos^{m_L}(\phi_m) T_s(\psi) g(\psi) \cos \psi, & \text{for } 0 \leq \psi \leq \Psi, \\ 0, & \text{elsewhere,} \end{cases} \quad (3.6)$$

where  $T_s(\psi)$  represents the transmitted band pass signal,  $g(\psi)$  is the gain of the imaging concentrator,  $m_L$  is the Lambertian factor of the source,  $A_r$  is the area of the PD and  $d$  is the distance between the LED and PD. Therefore, the received sequence for a transmitted sequence  $s$  is given as

$$\mathbf{y} = h\mathbf{s} + \mathbf{z}_{PLC} + \mathbf{z}_{VLC}, \quad (3.7)$$

where  $\mathbf{z}_{PLC}$  consists of samples defined in (3.4) and  $\mathbf{z}_{VLC}$  are real values with distribution  $\mathcal{N}(0, \sigma_V^2)$  for a noise variance  $\sigma_V^2$ .

### 3.2.2 Markov Model for Memory PLC-VLC Channel

For a given set of states  $\mathbf{c} = (c_1, c_2, \dots, c_N)$ , the Markov model for the channel distribution can be defined by three parameters  $X = [A, B, \Pi]$ . The transition probability matrix  $A(t) = [a_{ij}(t)]$  represents the probability of the channel transitioning into a different state or remaining in the same state between observation period  $t$  and  $t_{n+1}$ . Each element  $a_{ij}$  represents the probability of transitioning from state  $i$  to state  $j$ .

The present state of the model at  $t$  is described by a set of probabilities  $\Pi_t = [\pi_{t,1}, \pi_{t,2}, \dots, \pi_{t,n}]$ . Using the transition probability matrix  $A(t)$ , the state probability distribution at  $t + 1$  is

$$\Pi_{t+1} = \Pi_{t+1}A. \quad (3.8)$$

The aim is to iterate  $\Pi$  until it attains a steady state probability distribution  $\Pi_{ss}$  at iteration  $k$ . Therefore, if

$$\begin{aligned} \Pi_{t+k} &= \Pi_{t+k}A, \\ &= \Pi_t A^k, \end{aligned} \quad (3.9)$$

then

$$\Pi_{ss} = \Pi_{ss}A^k, \quad (3.10)$$

at the  $k$ -th iteration.

The error state probability matrix  $B = [b_{ij}]$  describes the probabilities of the model making a correct or incorrect decision given its current state. Hence,

$$\sum_{i=1}^N b_i = 1, \quad \sum_{j=1}^N b_j = 1. \quad (3.11)$$

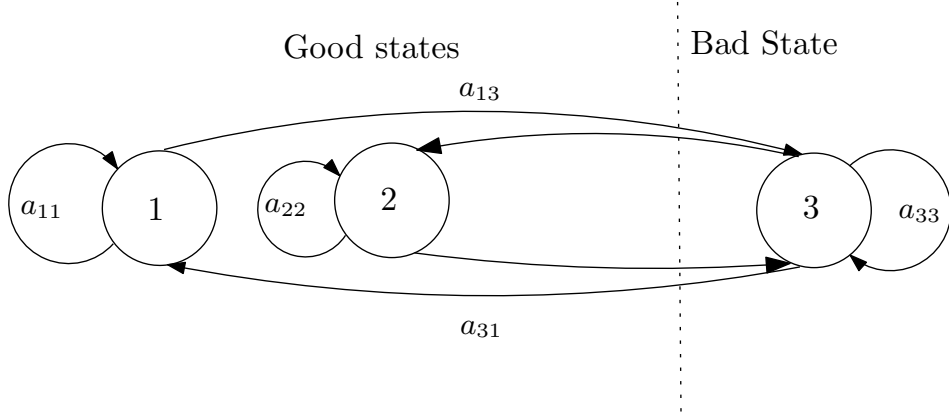


FIGURE 3.3: Fritchman Model with 3 States

### 3.2.3 Fritchman Model

The Fritchman model suits channels with burst errors such as the PLC channel by grouping the channel states into two groups of  $k$  good states and  $N - k$  bad states [63] as shown in Fig. 3.3. Assuming the absence of external interference such as external illumination, the noise model of the VLC channel is predominantly Gaussian. Hence, a 3-state model as shown in Fig 3.3 is chosen to model the PLC-VLC channel such that the transition probability of the channel remaining in a good state is higher than the probability of transitioning to a bad state while in a good state. Two states represent the good states while one state represents the bad state. Therefore, the state transition probabilities are

$$A = \begin{bmatrix} a_{11} & 0 & a_{13} \\ 0 & a_{22} & a_{23} \\ a_{31} & a_{32} & a_{33} \end{bmatrix}. \quad (3.12)$$

The error state probability  $B$  is therefore

$$B = \begin{bmatrix} 1 & 1 & 0 \\ 0 & 0 & 1 \end{bmatrix}, \quad (3.13)$$

where the first row represents the error probabilities of each state when the bit is correctly received while the second row represents otherwise.

### 3.2.4 Baum-Welch Algorithm

In order to find the maximum likelihood parameters  $X = \{A, B\}$  that maximize  $\Pr(\bar{O}|X)$ , the Baum-Welch algorithm [66] iterates until it converges into an estimated  $X = \{A, B\}$ . The estimated elements of  $A$  are defined as

$$\begin{aligned} \hat{a}_{ij} &= \frac{\text{expected number of transitions from } i \text{ to } j}{\text{expected number of transitions from } i}, \\ &= \frac{\sum_{t=1}^{T-1} \xi_t(i, j)}{\sum_{t=1}^{T-1} \gamma_t(i)}, \end{aligned} \quad (3.14)$$

while the estimated elements of  $B$  are defined as

$$\begin{aligned}\hat{b}_j(e_k) &= \frac{\text{expected number of times } e_k \text{ is emitted from state } j}{\text{expected number of visits to state } j}, \\ &= \frac{\sum_{t=1}^T \gamma_t(j)}{\sum_{t=1}^T \gamma_t(j)}.\end{aligned}\quad (3.15)$$

The term

$$\begin{aligned}\xi_t(i, j) &= \Pr[s_t = i, s_{t+1} = j | \bar{O}, X], \\ &= \frac{\alpha_t(i) a_{ij} b_j(O_{t+1}) \beta_{t+1}(j)}{\Pr[\bar{O} | X]},\end{aligned}\quad (3.16)$$

and

$$\begin{aligned}\gamma_t(i) &= \Pr[s_t = i | \bar{O}, X], \\ &= \frac{\alpha_t(i) \beta_t(i)}{\Pr[\bar{O} | X]} \quad i = 1, 2, \dots, N.\end{aligned}\quad (3.17)$$

From (3.16) and (3.17), the forward variables  $\alpha_t(i)$  are determined by initializing at  $t = 1$

$$\alpha_1(i) = \pi_i b_i(O_1), \quad i = 1, 2, \dots, N, \quad (3.18)$$

then at  $t > 1$ ,

$$\alpha_{t+1}(i) = \left[ \sum_{i=1}^N \alpha_t(i) a_{ij} \right] b_i(O_{t+1}), \quad \text{for } 1 \leq t \leq T-1, 1 \leq j \leq N, \quad (3.19)$$

and terminated at condition

$$\Pr[\bar{O} | X] = \sum_{i=1}^N \alpha_T(i) \beta_T(i), \quad (3.20)$$

where

$$\sum_{i=1}^N \alpha_T(i) = \sum_{i=1}^N \Pr[O_1, \dots, O_T, s_T = i | X] = \Pr[\bar{O} | X]. \quad (3.21)$$

At  $t = 1$ , the backward variables  $\beta_t(i)$  are initialized for all  $N$  states

$$\beta_1(i) = 1, \quad i = 1, 2, \dots, N, \quad (3.22)$$

and at  $t > 1$ ,

$$\beta_t(i) = \sum_{j=1}^N \beta_{t+1}(j) b_j(O_{t+1}) a_{ij}, \quad \text{for } 1 \leq t \leq T-1, 1 \leq j \leq N. \quad (3.23)$$

### 3.2.5 Semi-Hidden Fritchman HMM

Error sequences are generated from each frame transmitted as a vector of binary bits over the channel. For simplicity, a randomly composed text message of 70 letters including spaces, which translate to 560 bits are used. The frames are repeatedly transmitted 100 times in order to generate  $5.6 \times 10^4$  bits. An error sequence vector is then generated to using the Hamming distance method between the sent vector and received vector to find the places where they differ. Where the index of the sent and received bits are the same, a "0" is stored in the error sequence vector. Otherwise, a "1" is stored in the error sequence vector. We initialize  $X = \{A, B, \Pi\}$  as follows

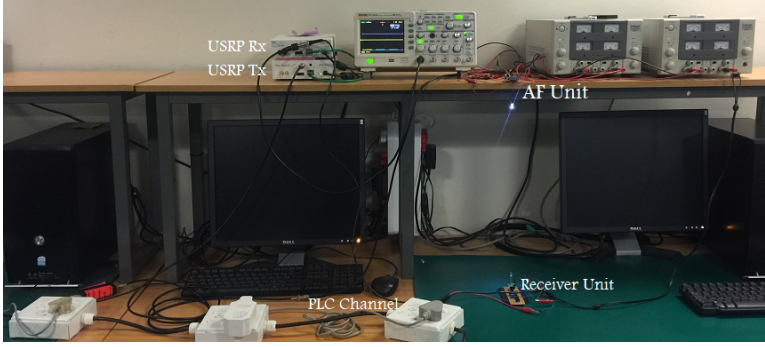


FIGURE 3.4: Hybrid AF PLC-VLC indoor laboratory testbed.

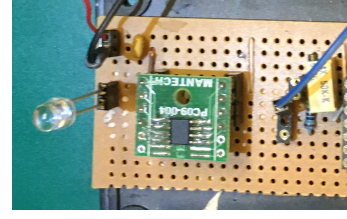


FIGURE 3.5: VLC transmitter unit.

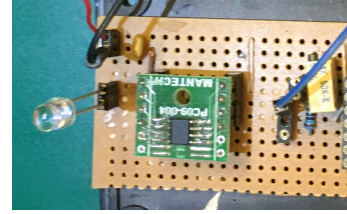


FIGURE 3.6: VLC receiver unit.

$$A = \begin{bmatrix} 0.68 & 0 & 0.32 \\ 0 & 0.79 & 0.21 \\ 0.48 & 0.45 & 0.07 \end{bmatrix},$$

$$B = \begin{bmatrix} 1 & 1 & 0 \\ 0 & 0 & 1 \end{bmatrix},$$

and

$$\Pi = [ 0.47 \quad 0.47 \quad 0.06 ].$$

### 3.3 Experimental Setup and Measurements

Fig. 3.1 shows a block diagram of the experimental setup of the hybrid system. Multicarrier OFDM with BPSK is used to transmit the incoming information over an indoor PLC link. The OFDM-BPSK signals are designed using MATLAB and converted to analog signals for transmission over a USRP N210 software-defined radio. The USRP transmitter (Tx) converts the modulated OFDM signal to analog samples in order to transmit over the PLC channel. The narrowband PLC coupling unit provides galvanic isolation and filtering. At the output of the PLC channel, the PLC signal is amplified with an amplification factor  $A_V$  and a direct current (DC) bias is added to the amplified signal. The PLC signal hence modulates the intensity of the LED which is always ON as a result of the DC voltage.

The error sequence measurements are obtained in an indoor office environment using the testbed in Fig. 3.4 with the transmitter and receiver units of the VLC shown in Figs. 3.5 and 3.6 respectively. The parameters for the USRP radio and transmitted message are also defined in Table 3.1. These measurements are then used as training data to derive the steady-state transition probabilities of the channel using the Baum-Welch algorithm [66] and the initialized FM parameters  $X = \{A, B, \Pi\}$  as input. The resulting transition probabilities are then used to re-generate and obtain an approximate, statistical error sequence using the error vector generation algorithm [67] in order to validate the accuracy of the resulting channel models. An isolation transformer is used to block the impulse that may be injected into the powerline from devices plugged into the powerline bus network in the office. Measurements are taken in a 0 Watt (W) scenario, where other than the coupling circuits, no devices are connected to the powerline. Measurements are also taken in a 11 W scenario where a table lamp with an 11 W bulb is plugged into the powerline channel in order to create noise from a constant

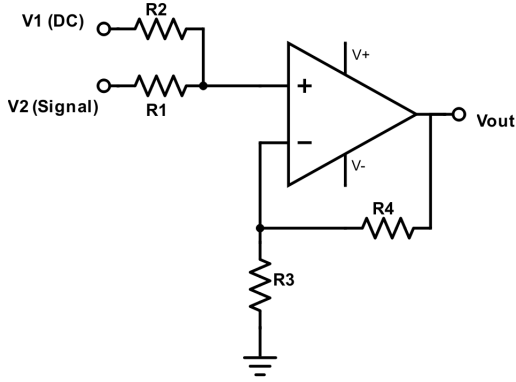


FIGURE 3.7: Voltage adder circuit to supply DC bias and amplification to the transmitted signal.

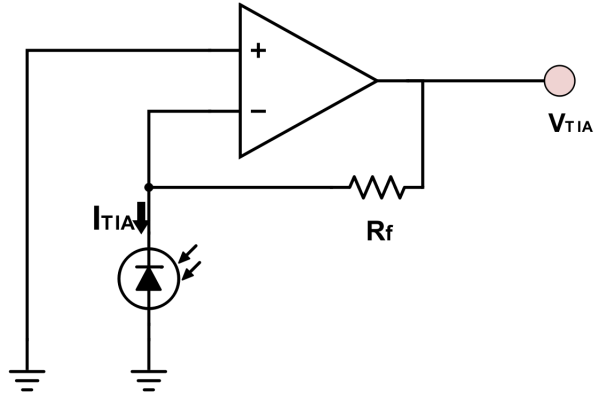


FIGURE 3.8: Transimpedance amplifier to convert photodiode current  $I_{TIA}$  to voltage.

voltage source. In order to have negligible attenuation due to distance in the PLC link, a considerably short PLC link length of approximately 2 meters is used.

For the VLC link, the geometric model in Fig. 2.8 is used and measurements are taken for different values of  $w$ , which is the horizontal displacement of the receiver from the transmitter's direct line of sight. The AF unit of the VLC transmitter in Fig. 3.7 uses an operational amplifier to amplify the PLC signal with a gain  $A_V = 1.45$  using a DC voltage  $V_1 = 1.45$  Volts. The off-the-shelf A3 series white LEDs used at the transmitter are not suitable for high frequency signals as they do not switch fast enough, hence the choice of 200 kHz center frequency in the USRP.

TABLE 3.1: USRP and modulation parameters

Parameter	Value
Center frequency	200 kHz
Sampling frequency	1 MHz
FFT Length	64
Message Length	560 bits per frame

The VLC receiver in Fig. 3.8 consists of an SFH 213 PD with a TIA unit which converts the intensity captured by the PD to an equivalent current. This current is converted to its equivalent voltage  $V_{TIA}$  and passed on to the USRP receiver (Rx). The receiver then samples the received voltages such that the received samples are demodulated to recover the likely transmitted bits.

## 3.4 Results

### 3.4.1 Estimated Model (State Transition Probabilities)

Table 3.2 shows the first order estimated model parameters (estimated state transition probabilities) at steady state. The measured error sequence for the different values of  $w$  in centimeters (cm) are obtained with and without the 11 W load connected to the powerline.

The estimated state transition probabilities show the model parameters that characterize the measured error sequences from an indoor PLC-VLC channel. It can be deduced from Table 3.2 that there are

TABLE 3.2: Estimated Models (estimated state transition probabilities)

w (cm)	Load (W)	$a_{11}$	$a_{13}$	$a_{22}$	$a_{23}$	$a_{31}$	$a_{32}$	$a_{33}$
0	0	0.8952	0.1048	1.0000	0.0000	0.4647	0.0026	0.5326
	11	0.7007	0.2993	0.9989	0.0011	0.3993	0.0611	0.5396
1	0	0.8965	0.1035	1.0000	0.0000	0.4852	0.0032	0.5116
	11	0.5895	0.4105	0.9990	0.0010	0.4687	0.0425	0.4888
2	0	0.7070	0.2930	1.0000	0.0000	0.6291	0.0013	0.3696
	11	0.7324	0.2676	0.9994	0.0006	0.4482	0.0590	0.4928
3	0	0.6790	0.3210	1.0000	0.0000	0.5583	0.0013	0.4404
	11	0.7852	0.2148	0.9995	0.0005	0.4474	0.0465	0.5062
4	0	0.4898	0.5102	1.0000	0.0000	0.5020	0.0026	0.4954
	11	0.6158	0.3842	0.9993	0.0007	0.4842	0.0452	0.4706
5	0	0.6641	0.3359	1.0000	0.0000	0.5628	0.0014	0.4358
	11	0.7141	0.2859	0.9994	0.0006	0.4379	0.0387	0.5234
6	0	0.5518	0.4482	1.0000	0.0000	0.4916	0.0008	0.5076
	11	0.5514	0.4486	0.9993	0.0007	0.4730	0.0226	0.5043
7	0	0.8962	0.1038	1.0000	0.0000	0.4476	0.0025	0.5499
	11	0.6947	0.3053	0.9991	0.0009	0.3254	0.0538	0.6207
8	0	0.7078	0.2922	0.9998	0.0002	0.5462	0.0143	0.4395
	11	0.5405	0.4595	0.9715	0.0285	0.4501	0.0542	0.4957
9	0	0.6114	0.3886	0.9978	0.0022	0.4983	0.0216	0.4801
	11	0.4715	0.5285	0.9323	0.0677	0.3984	0.1032	0.4984
10	0	0.5038	0.4962	0.8505	0.1495	0.4244	0.1203	0.4553
	11	0.4879	0.5121	0.9264	0.0736	0.4007	0.0987	0.5006

non-uniform estimated state transition probability values. This non-uniformity in estimated state transition probability distribution is attributed to the non-identical bit error sequences measured as a result of the different scenarios where  $w$  (cm) is varied with and without a load connected.

### 3.4.2 Estimated Model Validation

The aim of any channel modeling is to obtain the most probable parameter set given a measured or simulated dataset. Hence, it is important to analytically validate the fitness and accuracy of the estimated model derived in Section 3.4.1. The log-likelihood ratio (LLR), the error-free run distribution (EFRD) and the error probabilities are used to validate a close match between the measured and model generated error sequences in Sections 3.4.2.1, 3.4.2.2 and 3.4.2.3 respectively thus ascertaining the accuracy of the derived models.

#### 3.4.2.1 Log-Likelihood Ratio Plots

In order to obtain a derived model that closely matches the measured data, the LLR assists with obtaining a set of model parameters that maximize the likelihood function. For a mathematical representation and description of the LLR, refer to [68].

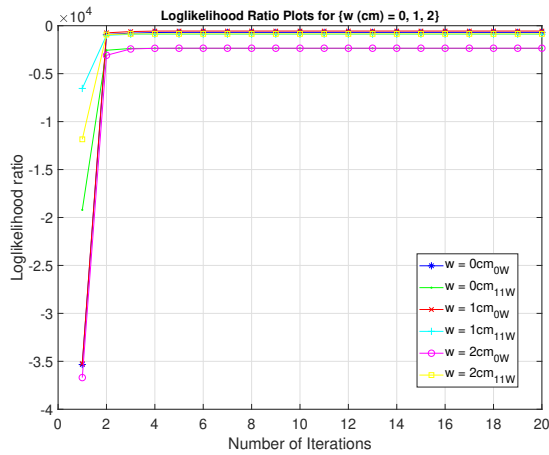


FIGURE 3.9: LLR plot 1.

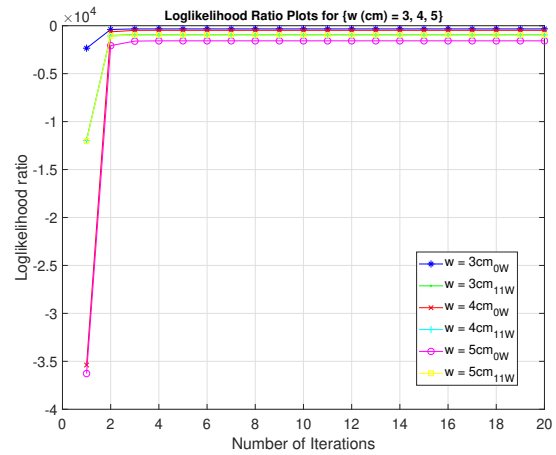


FIGURE 3.10: LLR plot 2.

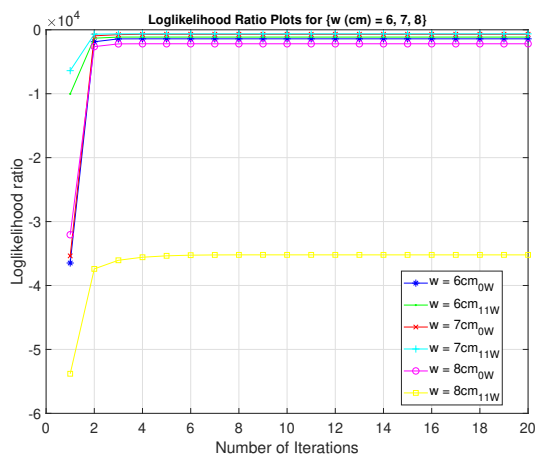


FIGURE 3.11: LLR plot 3.

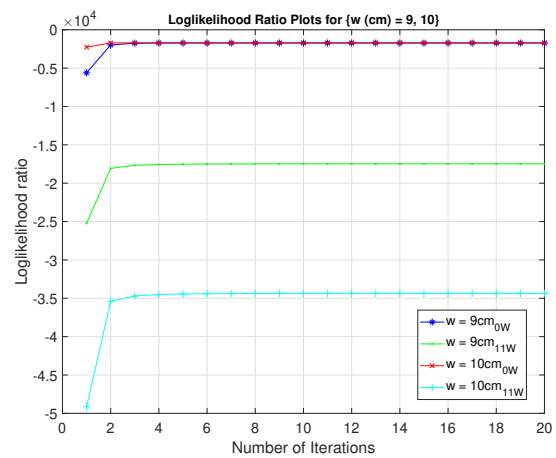


FIGURE 3.12: LLR plot 4.

Figs. 3.9 - 3.12 show the LLR plot for models realized for the different values of  $w$ , with and without the 11 W load connected. It can be deduced from these figures that the model starts to converge at the second iteration with a negative LLR value relatively close to zero, validating the model accuracy. For setups with higher amount of errors such as  $w > 8$  cm, the convergence is however not as close to zero. The LLR plot alone cannot be employed to measure the accuracy of a model as these values are a function of data size and can otherwise be applied in determining the most accurate of different model parameters obtained from the same error sequence.

### 3.4.2.2 Error-Free Run Distribution Plots

The EFRD denoted by  $Pr(0^m|1)$  implies the probability of transitioning from an error state to  $m$  consecutive error-free states. The EFRD probabilities are obtained for the measured error sequences. Using the estimated model parameter for each measured error sequence obtained, we generated an error sequence of the same length as the measured error sequence and then obtain the EFRD probabilities for these model generated error sequences.

A comparison between measured EFRD and model EFRD is then carried out to validate the accuracy of the derived models. Figs. 3.13 - 3.16 show a comparison of the measured EFRD and model EFRD for models realized for the different values of  $w$ , with and without the 11 W load connected. It can be deduced from Figs. 3.13 - 3.16 that a close match exists between the measured EFRD and model EFRD,

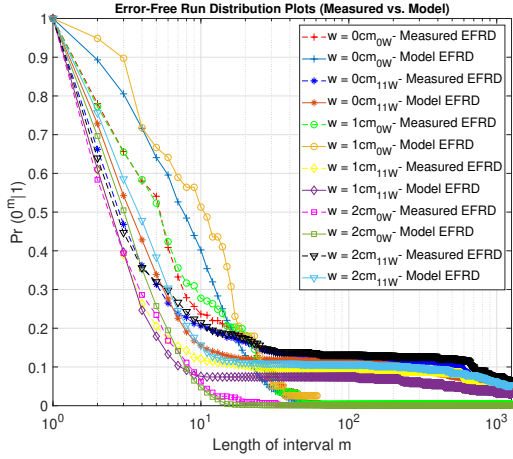


FIGURE 3.13: Measured vs. model-generated EFRD 1.

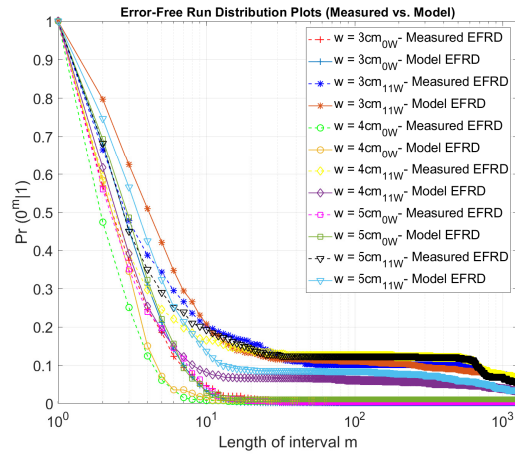


FIGURE 3.14: Measured vs. model-generated EFRD 2.

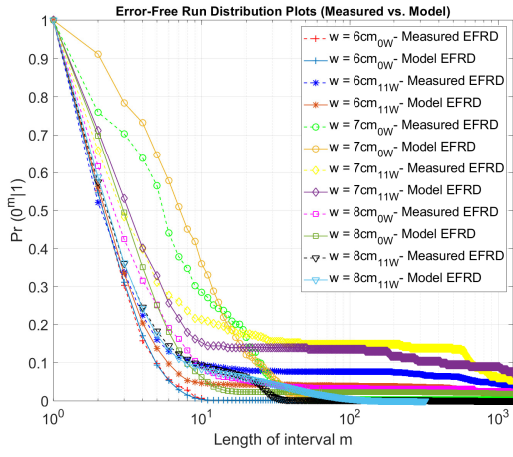


FIGURE 3.15: Measured vs. model-generated EFRD 3.

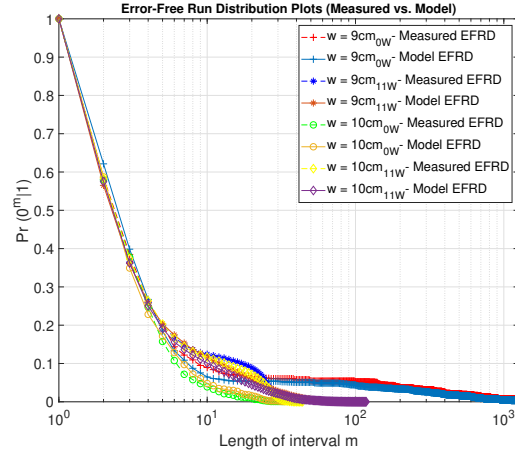


FIGURE 3.16: Measured vs. model-generated EFRD 4.

validating the accuracy of the derived models. Wider deviations between the EFRs plots of the model and their respective measured sequences can be however observed such as the  $w = 1$  cm scenario in Fig. 3.13 and  $w = 7$  cm scenario in Fig. 3.15. This can be attributed to the first order Markov model not overfitting the model. It can also be seen in these figures that  $Pr(0^m|1)$  denoting the EFRD is a monotonically decreasing function of  $m$ , that is  $Pr(0^0|1) = 1$  and similarly  $Pr(0^m|1) \rightarrow 0$  as the length of interval denoted by  $m$  increases.

### 3.4.2.3 Error Probabilities

Fig. 3.17 shows the bit error rate (BER) from the measured sequences for different values of  $w$ . The BER is given as  $\frac{\sum_{k=1}^K e}{K}$ . As the value of  $w$  increases, the number of errors increases due to the attenuation  $h$  on the signal power. The effect of the noise introduced into the PLC link by the 11 W load also becomes evident in the poorer BER performance for most values of  $w$  when compared with the 0 W scenario. As  $w$  increases, the noise power dominates the signal power, hence more errors as shown in Fig. 3.17.

The error probabilities of the measured and the model generated error sequences are obtained in order to validate the accuracy of the derived models. A close match between the error probabilities of the

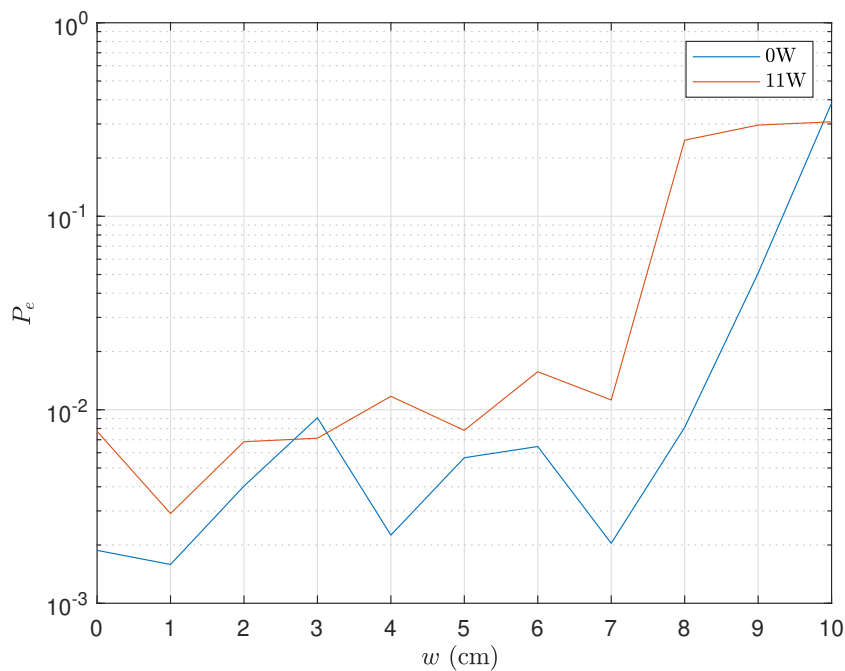


FIGURE 3.17: Probability of error for different values of  $w$  with  $d = 40$  cm measured from the hybrid channel.

measured  $P_e$  and model generated  $\bar{P}_e$  error sequences validates the accuracy of the derived models. Table 3.3 shows the error probabilities for the measured and model generated error sequences for the different values of  $w$ , with and without the 11 W load. It can be deduced from Table 3.3 that a close match exists between the error probabilities of the measured and model generated error sequences thus validating the accuracy of the derived models for the indoor PLC-VLC channel.

### 3.5 Conclusion

The error distribution of an indoor, hybrid AF PLC-VLC channel with memory is evaluated by taking error sequence measurements from the testbed with the aid of OFDM-BPSK modulation with USRP N210 radios. EFR distributions are determined from the measured error sequences in order to characterize the error distribution using the measurements from different channel conditions, under different channel disturbances. The Baum-Welch re-estimation algorithm is then used to develop statistical model parameters for the corresponding channel conditions and disturbances. The measured and re-estimated model parameters show close matches based on the chosen initial and derived parameters for the different channel conditions. The closeness of the  $\bar{P}_e$  of the error sequence generated from the estimated model with the measured  $P_e$  indicate the suitability of the SHMM and the derived statistical model parameters.

TABLE 3.3: Error probabilities comparison ( $P_e$ ) - measured sequence vs. ( $\bar{P}_e$ ) - model regenerated sequence

w (cm)	Load (W)	$P_e$	$\bar{P}_e$
0	0	0.0019	0.0027
	11	0.0135	0.0143
1	0	0.0016	0.0017
	11	0.0029	0.0025
2	0	0.0059	0.0066
	11	0.0068	0.0077
3	0	0.0091	0.0084
	11	0.0071	0.0079
4	0	0.0023	0.0029
	11	0.0117	0.0125
5	0	0.0057	0.0053
	11	0.0078	0.0087
6	0	0.0065	0.0064
	11	0.0157	0.0166
7	0	0.0020	0.0025
	11	0.0112	0.0120
8	0	0.0081	0.0086
	11	0.2473	0.2458
9	0	0.0508	0.0513
	11	0.2959	0.3085
10	0	0.3843	0.3827
	11	0.3076	0.3167

# Soft-Decision Decoding of Permutation Block Codes in AWGN and Rayleigh Fading Channels

---

**This chapter is based on the following publication:** *O. Kolade, J. Versfeld, and M. van Wyk, "Soft-Decision Decoding of Permutation Block Codes in AWGN and Rayleigh Fading Channels", IEEE Communications Letters, vol. 21, no. 12, pp. 2590 - 2593, Dec 2017.*

The author of this thesis conceptualized the work, performed the simulations, analyzed the results and wrote the paper.

---

## 4.1 Introduction

In designing a decoding algorithm for forward error correction codes, coding gain and computational efficiency are major considerations in evaluating the performance of the decoding algorithm. It is therefore important for decoding algorithms to combine both low complexity and high coding gain performance in practical environments.

$M$ -ary frequency shift keying ( $M$ -FSK) modulation provides constant envelope modulation. Assuming equal energy signals are transmitted in the AWGN channel, envelope detection then becomes suitable to recover the message by using  $M$  correlators at the receiver [38].

Vinck [69] showed the effects of different noise conditions on  $M$ -FSK signals assuming a powerline communications (PLC) channel. Vinck *et al.* [44] further showed that permutation coding with  $M$ -FSK can handle narrowband, impulse noise and also background noise within a certain distance of transmission.

When  $M$ -FSK is combined with permutation codes, additional frequencies help spread the information over additional timeslots, which aids performance against impulse and narrowband noise [70]. Shum [71] also showed that permutation block codes give better bit error rate performance when compared with convolutional codes soft-decoded with the Viterbi algorithm in some signal-to-noise ratio (SNR) regions.

With code construction examples in [72], existing decoding algorithms rely on the code construction method. We therefore introduce an efficient soft-decision decoder of permutation block codes irrespective of the code construction algorithm. We modulate with  $M$ -FSK and evaluate the performance of the proposed soft-decision decoder which implements the Hungarian Algorithm [73] for maximum assignment and Murty's algorithm of the  $k$ -th assignment [74]. The performance of the decoder is analyzed in the presence of AWGN and Rayleigh fading channel conditions.

## 4.2 $M$ -FSK and Permutation Codes

Given a set of integers  $v = \{v_1, v_2, \dots, v_L\}$ , a permutation codebook  $\mathcal{C}$  is defined as a subset of the set  $\mathcal{P}$  containing all permutations of the integers  $v$ , such that the minimum Hamming distance  $d_{\min}$  of  $\mathcal{C}$  is the largest, i.e., the minimum of the Hamming distances between any two permutations in  $\mathcal{C}$  is optimized. The code rate of a permutation codebook is defined as [71]

$$R = \frac{\log_2(|\mathcal{C}|)}{L \log_2(L)}, \quad (4.1)$$

where  $L$  is the length of each codeword and  $|\mathcal{C}|$  is the number of codewords in  $\mathcal{C}$ .

We use a one-to-one mapping from the integers  $\{v_1, v_2, \dots, v_L\}$  onto the  $M = 2^m$  distinct frequencies of the  $M$ -FSK modulator, similar to [75, 76], except now we use the integers of the codebook  $\mathcal{C}$ , and not the elements from the field  $GF(2^m)$ . The vector representation of  $M$ -FSK of a transmitted signal for a sampling instance  $T$ , assuming  $f$  was transmitted can be generalized as

$$s_z(t) = \begin{cases} \sqrt{E_s}, & \text{if } f = f_z, \\ 0, & \text{otherwise,} \end{cases} \quad (4.2)$$

where  $E_s$  is the symbol energy and  $f_z$  is any of the  $M$  possible frequencies utilised to transmit any of the  $M$  possible signals  $s_z(t)$  for  $z = 1, 2, \dots, M$ .

## 4.3 Channel Model

At the output of the AWGN channel, a non-coherently received signal  $r(t)$  of a transmitted signal  $s_z(t)$  is represented as [38]

$$r(t) = s_z(t)e^{j\phi} + \eta(t), \quad \text{for } 0 \leq t \leq T, \quad (4.3)$$

where  $\eta(t)$  is a random complex-valued white Gaussian process with zero-mean and variance of each complex component  $\sigma^2 = 2N_0$ .

The function of the non-coherent  $M$ -FSK detector is to choose the most likely transmitted frequency from a set of  $M$  frequencies, by choosing the one with the highest energy present at a sampling instance  $T$  [38]. The SNR for such a system is calculated as  $\text{SNR} = E_s/N_0$  (refer to [38]). The non-coherent  $M$ -FSK detector consists of a bank of  $M$  pairs of quadrature correlators, one pair for each frequency to be detected.

The output of each quadrature pair is a metric, which is calculated using the square law. Each metric corresponds to each possible frequency. The most likely transmitted symbol for sampling instance  $T$  is determined based on these  $M$  metrics, by choosing the symbol corresponding to the metric with the highest value as the output of the envelope detector [38].

The effect of Rayleigh fading on the transmitted signal  $s_z(t)$  is multiplicative [38]. The received low-pass signal is therefore

$$r(t) = \alpha e^{j\phi} s_z(t) + \eta(t), \quad \text{for } 0 \leq t \leq T, \quad (4.4)$$

where  $\alpha$  is the fading constant and is modelled as a random variable with a complex-valued Gaussian distribution. The channel model assumes a slow fading frequency non-selective channel such that a fading condition persists for a length of the signaling time. We assume fading is slow enough to estimate  $\phi$  and therefore achieve coherent detection [38].

## 4.4 Soft-Decision Decoder

The soft-decision decoder aims to iteratively rank the costs of the input signal matrix until the assignment produces a codeword in  $\mathcal{C}$ . In this section, we discuss the two algorithms combined in the decoder, the first determines the highest cost  $G_1$  of the signal matrix which produces an equivalent codeword  $A_1$ . The second algorithm iteratively ranks the costs from the second-highest cost to the  $k$ -th highest cost  $G_2, G_3, \dots, G_k$  each producing an equivalent codeword  $A_2, A_3, \dots, A_k$ .

### 4.4.1 Hungarian Algorithm

In linear programming, if the cost  $G_1$  is such that we minimize

$$G_1 = \sum_{i=1}^n \sum_{j=1}^n h_{ij} x_{ij}, \quad (4.5)$$

subject to

$$\begin{aligned} \sum_{i=1}^n x_{ij} &= 1, (j = 1, \dots, n), \\ \sum_{j=1}^n x_{ij} &= 1, (i = 1, \dots, n), \end{aligned} \quad (4.6)$$

where  $x_{ij} \geq 0$ ,  $n$  is a positive integer and the  $n \times n$  square cost matrix  $\mathbf{H} = [(h_{ij})]$ , then  $G_1$  is the cost of the assignment [74].

The Hungarian algorithm [73] therefore finds the permutation matrix  $\mathbf{X} = [(x_{ij})]$  that yields the lowest cost  $G_1$ , given a square cost matrix. Since  $\mathbf{X}$  is such that only one element on each row and column is 1 while other elements are 0, each element in the  $i$ -th row and  $j$ -th column of  $\mathbf{X}$  having the value of 1 permute to form a permutation codeword.

Permutation block codes are constructed such that each symbol appears only once in the codeword. The Hungarian assignment solution (for minimum cost) also assigns each job to each worker such that a worker can only be assigned one task/job, the total sum of all costs gives the minimal cost of assignment. The cost matrix must be square, having the same number of jobs as workers. In order to apply the Hungarian algorithm to decode permutation codes, the maximum assignment is rather considered.

Therefore, a sample signal at the input of the Hungarian algorithm decoder is converted to

$$r'(t) = -1 \times r(t). \quad (4.7)$$

The cost  $G_k$  at the  $k$ -th iteration has a row-column equivalent  $a_k$  such that

$$a_k = \{(1, j_1), \dots, (L, j_L)\}. \quad (4.8)$$

Each row-column pair represents a cell in the cost matrix. The sum of the cell values of all the row-column pairs in  $a_k$  produce the cost  $G_k$ . As an example, a one-to-one mapping of randomly generated messages to the cyclically rotated codebook  $\mathcal{C}_E$  with  $d_{\min} = 4$  [71]

$$\mathbf{C}_E = \begin{bmatrix} 1 & 2 & 3 & 4 \\ 4 & 1 & 2 & 3 \\ 3 & 4 & 1 & 2 \\ 2 & 3 & 4 & 1 \end{bmatrix},$$

produces a received  $R_1$  using (4.3) and negated signal  $R'_1$  using (4.7)

$$R'_1 = \begin{bmatrix} 0.1389 & \boxed{-0.3035} & 0.9411 & 0.0511 \\ \boxed{0.0985} & 0.1106 & -0.0253 & 1.1810 \\ 0.9716 & 0.0995 & 0.0668 & \boxed{-0.2412} \\ 0.0701 & 0.8874 & \boxed{-0.0914} & -0.0921 \end{bmatrix},$$

at the output of the channel.

The sum of the boxed values in  $R'_1$  equals  $-0.5376$  which is the minimum cost of  $R'_1$  using [73]. The output codeword  $A_1$  in this case is 2143 and its row-column representation is

$$a_1 = \{(1, 2), (2, 1), (3, 4), (4, 3)\}. \quad (4.9)$$

If  $A_1 \in C_E$ , the decoder stops and outputs  $A_1$  as the likely transmitted codeword. However, should  $A_1 \notin C_E$ , an invalid codeword is detected. The decoder therefore continues to Murty's algorithm to iteratively find  $A_2, A_3, \dots, A_k$ .

#### 4.4.2 Murty's Algorithm

Murty's algorithm [74] furthers upon the assignment problem by ranking the costs of a square matrix in order of increasing costs. Using the Hungarian algorithm, the next best assignment  $A_2, A_3, \dots, A_k$  can be solved.

Consider the assignment solution  $A_1$  for  $R'_1$ , the algorithm extracts  $n - 1$  non-empty subsets of  $R'_1$  into nodes  $N_1, N_2, \dots, N_{n-1}$ , by partitioning  $a_1$ . Nodes in this case are defined as:

$$\begin{aligned} N_1 &= \{\overline{(1, j_1)}\}, \\ &\vdots \end{aligned} \quad (4.10)$$

$$N_{n-1} = \{(1, j_1), \dots, \overline{(n-1, j_{n-1})}\}.$$

In each node, the row-column pair without the bar implies the values on the row and column are removed from  $R'_1$  for that node while the row-column pair with the bar implies the item at that row-column position is replaced with infinity. The minimum cost is then solved for each node. The node with the least cost forms the next assignment  $a_2$ .

Using  $R'_1$ , the output of the second iteration  $A_2$  decodes as 4123 and

$$a_2 = \{(1, 4), (2, 1), (3, 2), (4, 3)\}. \quad (4.11)$$

Since  $A_2 \in C_E$ , the decoder stops and outputs  $A_2$ . For  $A_2 \notin C_E$ ,  $a_2$  is used to partition for the next assignment.

#### 4.4.3 Maximum Likelihood Decoding

If the  $L$ -th symbol in a codeword from the set of integers  $v$  corresponds to the value of  $j$  in  $(x_{ij})$ , then each codeword in  $C$  can be used to generate a permutation matrix  $X = [(x_{ij})]$  defined in (4.5).  $X$

can then be generated such that the element in the  $i$ -th row and  $j$ -th column (which is now the  $L$ -th symbol in  $v$ ) is 1 while other elements on the row and column are 0. Using (4.5), the cost of each codeword in  $\mathcal{C}$  is

$$G_k = \sum_{i=1}^M \sum_{j=1}^L R_f x_{ij}, \quad \text{for } 1 \leq k \leq |\mathcal{C}|, \quad (4.12)$$

where  $R_f$  is the received  $M \times M$  matrix corresponding to the  $f$ -th transmitted message sequence. The optimum decoder selects the codeword  $A_1$  that corresponds to the lowest cost  $G_1$ .

## 4.5 Simulation Results

Simulations are carried out by comparing the performance of the soft-decision decoder with hard-decision and maximum likelihood decoding. Using Monte Carlo simulations, a sequence of length  $10^5$  symbols, consisting of randomly selected integers in the range  $1, 2, \dots, |\mathcal{C}|$ . The symbols are encoded with a permutation codebook with codewords satisfying the required  $d_{\min}$  and modulated with  $M$ -FSK. At the receiver, hard decision combines envelope detection with minimum distance decoding. The hard decision method is compared with the soft-decision method in which every  $M \times M$  output of the channel is decoded directly without demodulation. In the soft-decision decoder, we refer to the first iteration as the output of the Hungarian algorithm  $A_1$ , the second iteration as the first Murty's algorithm assignment solution  $A_2$ , the third iteration as the second Murty's algorithm assignment solution  $A_3$  and so on. 4-FSK is used to modulate when  $L = 4$  while 8-FSK is used for  $L = 8$  codebook.

Table 4.1 and 4.2 compare the performance of the soft-decision decoder over hard decision for large codebooks in AWGN and AWGN plus Rayleigh fading channels respectively. The performance of the soft-decision decoder is also compared with the optimum performance in Fig. 4.1 - 4.3. The value of the  $\frac{|\mathcal{C}|}{|\mathcal{P}|}$  ratio affects the error-correction performance of the soft-decision decoder, especially at the first iteration. The lower the ratio, the higher the probability of outputting a codeword outside  $\mathcal{C}$ . In the AWGN channel, this effect of values selected between  $\frac{|\mathcal{C}|}{|\mathcal{P}|} = 0.1667$  and  $\frac{|\mathcal{C}|}{|\mathcal{P}|} = 1$  is shown in Fig. 4.1 and 4.2.

The performance of the decoder also depends on  $d_{\min}$  of the codebook. For example, the soft-decision decoder produces better performance for codebook  $|\mathcal{C}| = 12$  and  $d_{\min} = 2$  compared with a similar codebook, but with  $d_{\min} = 3$ . The lowest gain is observed when  $\frac{|\mathcal{C}|}{|\mathcal{P}|}$  of the codebook is the lowest while the highest gain is at  $\frac{|\mathcal{C}|}{|\mathcal{P}|} = 1$ . When  $\frac{|\mathcal{C}|}{|\mathcal{P}|} = 1$ , every output of the decoder will always be a codeword in  $\mathcal{C}$  at the first iteration. Therefore, computational performance of the decoder is minimal at this condition.

The addition of the Rayleigh slow fading channel degrades the performance of both the soft-decision and hard decision decoders as observed in Fig. 4.3. However, the soft-decision decoder still outperforms the hard decision decoder for codebooks with  $\frac{|\mathcal{C}|}{|\mathcal{P}|} > 0.0076$  as shown in Table 4.2. The behavior of the decoder relative to the different code rates remain similar to the AWGN channel.

The computational complexity of the soft-decision decoder becomes a major advantage over hard decision for large size codebooks. For example, an 8-FSK system requires a codebook with  $L = 8$ . Therefore,  $|\mathcal{P}| = 40320$ . Large codebooks constructed from  $|\mathcal{P}|$  means it will be computationally too complex to decode using a look-up table. However, because the input to the soft-decision decoder is always an  $M \times M$  matrix, the same complexity is required by the decoder irrespective of the size of  $|\mathcal{C}|$ . The worst case order of complexity of the decoder is  $O(M^4)$  which combines the complexity of the Hungarian algorithm ( $O(M^3)$ ) [77] and Murty's algorithm ( $O(M^4)$ ) [78].

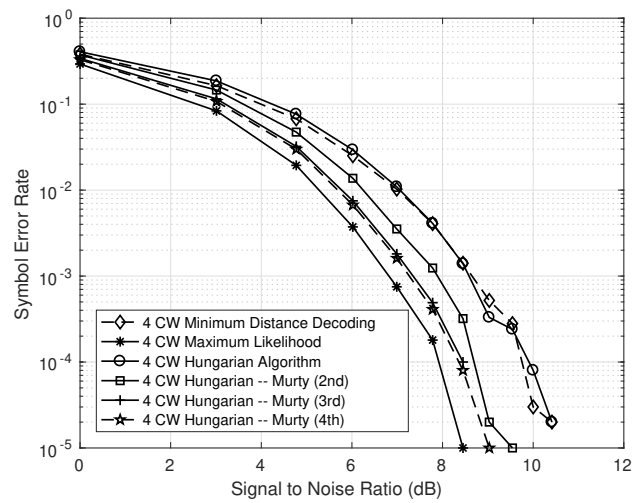


FIGURE 4.1: Performance of the soft-decision decoder in AWGN channel using 4 codewords (CW).

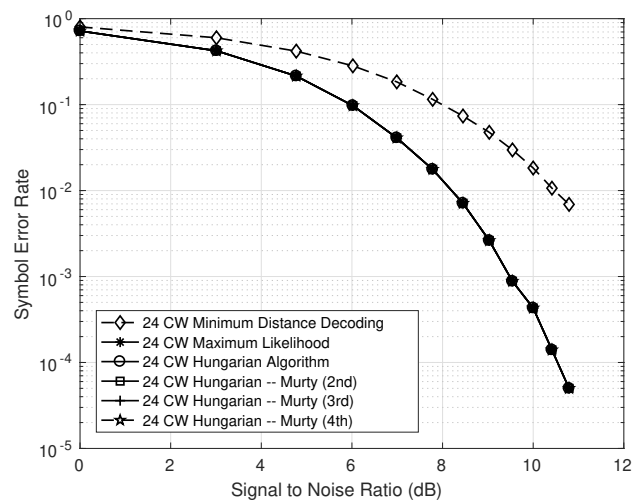


FIGURE 4.2: Performance of the soft-decision decoder in AWGN Channel using 24 codewords (CW).

TABLE 4.1: Performance of the soft-decision decoder using 8-FSK in AWGN channel, non-coherent detection

$ C $	$R$	$\frac{ C }{P}$	$d_{\min}$	Gain (dB)					
				$A_1$	$A_2$	$A_3$	$A_4$	$A_5$	$A_6$
8	0.125	0.0002	8	-0.3	-0.3	-0.2	-0.2	-0.2	-0.2
305	0.344	0.0076	5	0	0.1	0.2	0.4	0.5	0.5
1417	0.436	0.035	4	0	0.8	1.0	1.0	1.0	1.0
5000	0.512	0.124	3	0.6	1.2	1.3	1.3	1.3	1.3
10000	0.554	0.248	3	0.6	1.3	1.4	1.4	1.4	1.4
15000	0.578	0.372	3	0.6	1.2	1.3	1.3	1.3	1.3
20160	0.596	0.5	3	0.8	1.5	1.6	1.6	1.6	1.6
40320	0.637	1	2	2.3	2.3	2.3	2.3	2.3	2.3

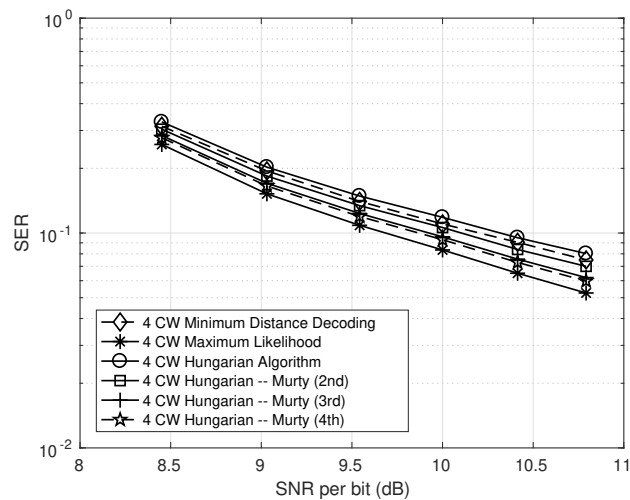


FIGURE 4.3: Performance of the soft-decision decoder in AWGN &amp; Rayleigh fading channels using 4 codewords (CW).

TABLE 4.2: Performance of the soft-decision decoder using 8-FSK in AWGN and Rayleigh fading channel

$ C $	$R$	$\frac{ C }{ P }$	$d_{\min}$	Gain (dB)					
				$A_1$	$A_2$	$A_3$	$A_4$	$A_5$	$A_6$
8	0.125	0.0002	8	-0.3	-0.3	-0.2	-0.2	-0.2	-0.2
305	0.344	0.0076	5	0	0.1	0.2	0.4	0.5	0.5
1417	0.436	0.035	4	0	0.8	1.0	1.0	1.0	1.0
5000	0.512	0.124	3	0.8	1.5	1.5	1.5	1.5	1.5
10000	0.554	0.248	3	1.0	1.5	1.5	1.5	1.5	1.5
15000	0.578	0.372	3	1.2	1.8	1.8	1.8	1.8	1.8
20160	0.596	0.5	3	1.8	1.8	1.8	1.8	1.8	1.8
40320	0.637	1	2	2.0	2.0	2.0	2.0	2.0	2.0

## 4.6 Conclusion

We designed a soft-decision decoder to decode permutation block codes in AWGN and Rayleigh fading channels. The decoder combines the Hungarian algorithm for maximum assignment and Murty's algorithm for the  $k$ -th assignment. A positive observation is that the computational performance of the decoder is not exponential, yet applicable to codebooks of large sizes. Results compared the performance of the decoding algorithms with envelope detection plus hard decision decoding up to the fourth iteration for  $L = 4$  and sixth iteration for  $L = 8$ .

The results show the performance of the Hungarian algorithm improved as the code rate increased. The performance of the Hungarian algorithm decoder is improved by iteratively using Murty's algorithm for the  $k$ -th assignment in order of decreasing costs. Murty's algorithm is only applied if the decoded codeword  $A_1 \notin C$ . With this condition, the complexity of the decoder is not always at its maximum.

# Impulse Noise Mitigation Using Subcarrier Coding of OFDM-MFSK Scheme in Powerline Channel

---

**This chapter is based on the following publication:** (Invited) *O. Kolade and L. Cheng, "Impulse Noise Mitigation Using Subcarrier Coding of OFDM-MFSK Scheme in Powerline Channel", IEEE SmartGrid-Comm, Oct 2019.*

The author of this thesis conceptualized the work, performed the simulations, analyzed the results and wrote the paper.

---

## 5.1 Introduction

Smart grids rely on powerline installations for communication in order to reduce the additional infrastructure required for communication. However, the powerline communication (PLC) channel is considered hostile as a result of impulsive noise (IN) and narrowband noise which affects multiple frequencies [30,31,50,51] in the narrowband region. In an indoor environment for example, devices plugged into the bus powerline network inject impulses into the network which affect the communication signals conveyed over the powerline. IN is observed to occur in bursts [31,61] with a maximum period of about 0.1 ms [52]. Hence, a series of signal bits may be affected in time domain or a frequency may be affected over a period of time.

While forward error correction in general improves the performance of uncoded systems, permutation codes [41] are proposed in [23,79,80] with different schemes to combat IN in powerline channels. Furthermore, permutation codes are combined with  $M$ -ary frequency shift keying ( $M$ -FSK) in [69,81] to avoid the occurrence of IN by using frequency switching properties of  $M$ -FSK to avoid IN bursts. The combination of multicarrier modulation such as orthogonal frequency division multiplexing (OFDM) with  $M$ -FSK provides powerful communication for fast time-varying channels [82]. OFDM is efficient in mitigating against inter-symbol interference while with FSK, the knowledge of the channel is not necessary, hence enabling non-coherent detection. The major disadvantage of the OFDM- $M$ FSK scheme however is its spectral inefficiency and several ideas have been proposed to improve the spectral efficiency of the scheme. It is suggested in [82] that the phases of the used subcarriers can be modulated in order to improve spectral efficiency. The spectral efficiency improvement of uncoded OFDM- $M$ FSK proposed in [83] uses multitone FSK to increase the number of bits that can be transmitted per OFDM symbol. The authors in [84] also propose an extended mapping technique and improved the coded information on each  $M$ -FSK subcarrier to one. Furthermore, it is proposed

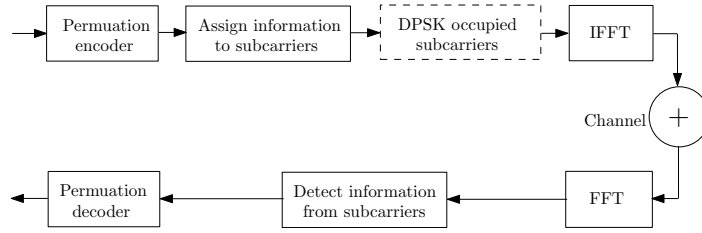


FIGURE 5.1: System diagram showing permutation codes with OFDM-MFSK without the block with dotted lines. Including block with dotted lines describes OFDM-MFSK-DPSK.

in [85] that permutation codes can assist with determining the spacing between subcarriers in the frequency domain. This proposed scheme was able to improve the BER performance of OFDM-MFSK in the presence of carrier frequency offsets in narrowband powerline channels. The authors in [86] recommend OFDM-MFSK ( $M \geq 8$ ) over OFDM with binary phase shift keying in rural and urban smart metering due to its low outage probability for uplink and downlink powerline networks. OFDM-MFSK is also recommended in [87] for internet of things, low data rate applications due to its high gain at low SNR when compared with the general OFDM modulation.

In this chapter, an OFDM-MFSK based subcarrier coding using permutations is proposed to mitigate the effect of IN in a PLC channel. The coding is done in the frequency domain in order to improve the bit error rate (BER) of the OFDM-MFSK scheme. The scheme naturally provides spacing between information-carrying subcarriers such that bad parts of the spectrum can be avoided. Combination of the scheme with permutation coding in the frequency domain hops the information between frequencies while repeating the information across the spectrum. Therefore, it is possible to recover the message with the help of other subcarriers in the permutation group if one subcarrier carrying the information is affected by noise. The mapping of the information-carrying subcarriers to the permutation sequence is done such that the spectral efficiency of the coded scheme is improved by choosing an appropriate codebook.

## 5.2 System Model

### 5.2.1 OFDM-MFSK

$M$ -FSK utilizes a set of  $M$  orthogonal signals to transmit messages by taking advantage of the different frequencies of the signals. At each sampling time, a signal is mapped onto a unique frequency while other frequencies are off. When combined with OFDM [82], the  $N$  total uncoded subcarriers used in the system are divided into  $M$  groups. Each  $\log_2 M$  bits have a one-to-one mapping onto each index of the  $M$  subcarriers in each  $\frac{N}{M}$  group. Therefore, the subcarrier index that corresponds to the incoming bits is activated while other subcarriers in the group are inactive. Using vector representation for the grouped subcarriers, a one '1' represents the activated subcarrier within the group while a zero '0' represents the inactive subcarriers. As an example, for  $M = 4$ , each signal is mapped onto one of any of the four vector alphabets in  $F$  such that

$$F_{4\text{FSK}} = \left\{ \begin{bmatrix} 1 \\ 0 \\ 0 \\ 0 \end{bmatrix}, \begin{bmatrix} 0 \\ 1 \\ 0 \\ 0 \end{bmatrix}, \begin{bmatrix} 0 \\ 0 \\ 1 \\ 0 \end{bmatrix}, \begin{bmatrix} 0 \\ 0 \\ 0 \\ 1 \end{bmatrix} \right\}. \quad (5.1)$$

To improve the spectral efficiency of OFDM-MFSK, additional information can be transmitted by adding the conventional OFDM with the activated subcarrier. For example, an  $H$ -ary phase shift keying ( $H$ -PSK) signal, selected from a set of PSK constellations  $\{h(b)\}$ ,  $b = 0, 1, \dots, H - 1$  is conveyed on

the activated subcarrier in each  $M$  group. Hence, the transmitted vector  $\mathbf{s}_m = h(b) \times \mathbf{f}_m$  is equivalent to the message symbol mapped onto  $M$  subcarriers such that the activated subcarrier also contains the  $h(b)$  constellation point. In addition,  $H$ -ary differential PSK ( $H$ -DPSK) can be used to differentially encode the phases of the activated subcarriers, thereby adding  $\log_2 H$  bits to each activated subcarrier. Therefore, each information-carrying subcarrier has  $\log_2 M + \log_2 H$  bits per  $M$  subcarrier group.

Assuming an additive white Gaussian noise (AWGN) channel, the non-coherently received signal on each subcarrier is defined as

$$\mathbf{r} = \mathbf{s}_m e^{j\phi} + \mathbf{n}_G, \quad (5.2)$$

where  $\mathbf{n}_G$  is a complex, zero mean sequence with a variance of  $\sigma_G^2 = 2N_0$  for each complex component. The symbol error probability of  $M$ -FSK in AWGN is similar to OFDM-MFSK and is defined as [38]

$$P_e = \sum_{n=1}^{M-1} \frac{(-1)^{n+1}}{n+1} \binom{M-1}{n} e^{-\frac{n \log_2 M E_b}{n+1 N_0}}, \quad (5.3)$$

where  $E_b$  is the energy per bit. Therefore, maximum likelihood (ML) detection of the likely transmitted OFDM-MFSK signal is done at the receiver by choosing from each group of  $M$  subcarriers, the likely transmitted vector  $\hat{r}$  [83]

$$\hat{r} = \arg \max_{\mathbf{f}_i \in F} |\mathbf{r}^H \mathbf{f}_i|^2, \quad (5.4)$$

where  $\mathbf{r}^H$  is the complex conjugate transpose of the received vector  $\mathbf{r}$  and  $\mathbf{f}_i$  is each row vector alphabet in  $F$ . It is obvious from (5.4) that this decision is based on the component with the maximum absolute value and is similar to envelope detection [38] for receiving  $M$ -FSK in AWGN. For OFDM-MFSK-DPSK, the information-carrying subcarrier within the group is first determined before detecting the DPSK signal.

The likely transmitted signal can also be detected by finding the component in the received vector having the least Euclidean distance with the likely transmitted vector  $\mathbf{f}_i$  in  $F$  and can be written as

$$\hat{r} = \arg \min_{\mathbf{f}_i \in F} (|\mathbf{r} - \mathbf{f}_i|). \quad (5.5)$$

The utilized bandwidth in  $M$ -FSK is  $\log_2(M)/M$  and for OFDM-MFSK, the utilized bandwidth is

$$\eta = \frac{\log_2(M)}{M} \frac{N}{N + N_c}, \quad (5.6)$$

where  $N_c$  is the number of subcarriers used for the cyclic prefix.

## 5.3 Proposed Scheme

### 5.3.1 OFDM-MFSK with Permutation Codes

Permutation codes are selected from a set of integers such that the codebook  $\mathcal{C}$  with  $|\mathcal{C}|$  codewords is a subset of all possible permutations  $\mathcal{P}$  with  $|\mathcal{P}|$  codewords. Each codeword  $c \in \mathcal{C}$  is a permutation of integers  $\{c_1, c_2, \dots, c_L\}$  and is a row vector of length  $L$ . The Hamming distance  $d_m$  between any two codewords is the number of symbols the two codewords differ in [42]. Hence, the codewords are selected to have the highest possible minimum Hamming distance  $d_{\min} = \min_{c_1, c_2 \in \mathcal{C}} d(c_1, c_2)$  between

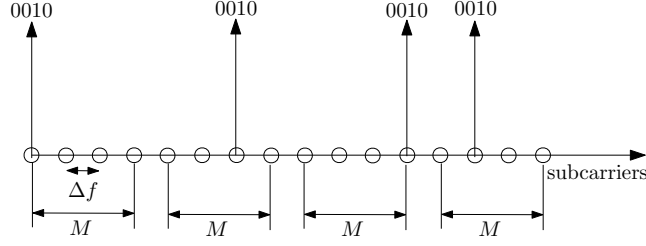


FIGURE 5.2: Encoded information bits 0010 are mapped to subcarriers such that the mapping in each group corresponds to each symbol in the permutation codeword 1342.

any two unique codewords provided  $c_1 \neq c_2$ . The coderate is defined as

$$R = \frac{\log_2(|\mathcal{C}|)}{L \log_2(L)}. \quad (5.7)$$

The subcarriers are encoded by a one-to-one mapping of  $k = \lfloor \log_2 |\mathcal{C}| \rfloor$  bits of information onto each codeword of an appropriate codebook  $\mathcal{C}$ . Note that  $\lfloor \cdot \rfloor$  denotes the floor function. The incoming bits map onto a codeword  $c$  such that each integer in  $c$  indicates the index of the active subcarrier in each  $M$  group. The  $k$  bits are repeated over each active subcarrier index as shown in Fig. 5.2 and additional  $\log_2 H$  bits can be conveyed over the active subcarriers. Therefore, a maximum of  $\lfloor \log_2 |\mathcal{P}| \rfloor + \log_2 H$  bits can be conveyed over  $M \times L$  subcarriers. The utilized bandwidth in the coded scheme can be defined as

$$\eta_{\text{CODED}} = \frac{\lfloor \log_2 |\mathcal{P}| \rfloor + \log_2 H}{M \times L} \frac{N_{\text{CODED}}}{N_{\text{CODED}} + N_c}, \quad (5.8)$$

where  $N_{\text{CODED}}$  is the number of subcarriers required to contain all the information-carrying subcarriers of the coded scheme.

As an example, each group of information bits in the set

$$\left\{ \begin{array}{l} 0000, 0001, 0010, 0011, \\ 0100, 0101, 0110, 0111, \\ 1000, 1001, 1010, 1011, \\ 1100, 1101, 1110, 1111 \end{array} \right\}, \quad (5.9)$$

is encoded using a one-to-one mapping to each codeword in

$$C = \left\{ \begin{array}{l} 1234, 1243, 1342, 1324, \\ 1423, 1432, 2134, 2143, \\ 3214, 3241, 2314, 2341, \\ 3421, 3412, 3124, 3142 \end{array} \right\}. \quad (5.10)$$

At the receiver, the likely activated subcarrier in each of the  $M$  groups is detected by computing (5.4) or (5.5) using individual subcarriers in each group. If there is no noise in the channel, the combination of the  $L$  subcarriers detected from the  $M \times L$  subcarriers representing the transmitted message will be a permutation codeword  $\hat{c} \in C$ . This permutation codeword can then be demapped to recover the transmitted message. However, in the presence of noise, it is possible that one or more out of the detected  $L$  subcarriers is wrongly detected. To recover the message, the hard decision (HD) decoder chooses the codeword with the minimum Hamming distance  $d_m = \min_{c_i \in C} d(\hat{c}, c_i)$  with the detected subcarrier combination.

### 5.3.2 OFDM-MFSK with Permutation Codes in Powerline Communication Channel

The powerline channel experiences narrowband noise, IN and background noise. A commonly used noise model for PLC is the common Middleton class A noise model [31] [32] which describes the noise mainly as background noise and IN. While background noise can be modelled as AWGN, IN is described as noise bursts, modelled by the noise's changing amplitude which depends on the number of appliances connected to the power network. If the bursts occurrence of IN is modelled to follow the Poisson distribution, then a sample of noise in the PLC channel that adds to the transmitted signal can be defined as

$$v_{\text{PLC}} = v_G + v_I\sqrt{D}. \quad (5.11)$$

The occurrence of IN is defined by the variable  $D$  with a Poisson distribution and impulsive index  $A$  which determines the frequency of occurrence of the zero-mean, Gaussian sequence  $v_I$  with variance of  $\sigma_G^2/A$ .

Due to the nature of frequency disturbances in narrowband PLC channel, permutation codes with  $M$ -FSK are combined to spread the information in order to avoid noisy parts of the frequency spectrum. Applying this principle to permutation coded OFDM-MFSK implies that subcarriers affected by noise are avoided by the frequency spreading OFDM-MFSK provides. When combined with permutation codes, it is still possible to recover the likely transmitted message if one subcarrier is affected by noise. As an example, a coded OFDM-4FSK vector  $\mathbf{S}(T) = [s_{ij}] \in \{0, 1\}$  with the energy in the activated subcarrier set to unity and encoded with permutation code (3214) is sent as

$$\mathbf{S}(T) = \begin{matrix} & t_1 & t_2 & t_3 & t_4 \\ \begin{bmatrix} 0 & 0 & 1 & 0 \\ 0 & 1 & 0 & 0 \\ 1 & 0 & 0 & 0 \\ 0 & 0 & 0 & 1 \end{bmatrix} & \begin{matrix} f_1 \\ f_2 \\ f_3 \\ f_4 \end{matrix} \end{matrix}, \quad (5.12)$$

while the effect of IN on  $\mathbf{S}(T)$  in a PLC channel can be illustrated as

$$\mathbf{Y}_1(T) = \begin{matrix} & t_1 & t_2 & t_3 & t_4 \\ \begin{bmatrix} 0 & 0 & 1 & 1 \\ 0 & 1 & 0 & 1 \\ 1 & 0 & 0 & 1 \\ 0 & 0 & 0 & 1 \end{bmatrix} & \begin{matrix} f_1 \\ f_2 \\ f_3 \\ f_4 \end{matrix} \end{matrix}, \quad (5.13)$$

affecting all the frequencies at time  $t_4$ . For HDPSK, the elements with 1 are replaced with the corresponding  $H$ -ary constellation. Using (5.2) and (5.11), each sample in  $\mathbf{Y}_1(T)$  received at the output of the PLC channel is given as  $y_{ij} = |s_{ij} + v_{\text{PLC}}|$ . Then, each column in  $\mathbf{Y}_1(T)$  is demodulated using (5.4), producing a set of integers  $\hat{c} = \{\hat{c}_1, \hat{c}_2, \dots, \hat{c}_L\}$  such that the chosen index in each column in  $\mathbf{Y}_1(T)$  corresponds to the integer in  $\hat{c}$ . The HD decoder therefore finds the codeword with minimum Hamming distance  $d_m$  using a look-up table.

### 5.3.3 Soft-Decision Decoding in Frequency Domain

At the output of the PLC channel, the received signal  $\mathbf{Y}_1(T) = [y_{ij}]$  whose elements  $y_{ij} = |s_{ij} + v_{\text{PLC}}|$  is decoded by finding the likely transmitted coded signal  $\mathbf{S}(T)$ . The SD decoder described in [27] is modified to decode the activated subcarriers by assuming  $\mathbf{Y}_1(T)$  as an assignment problem. Hence,

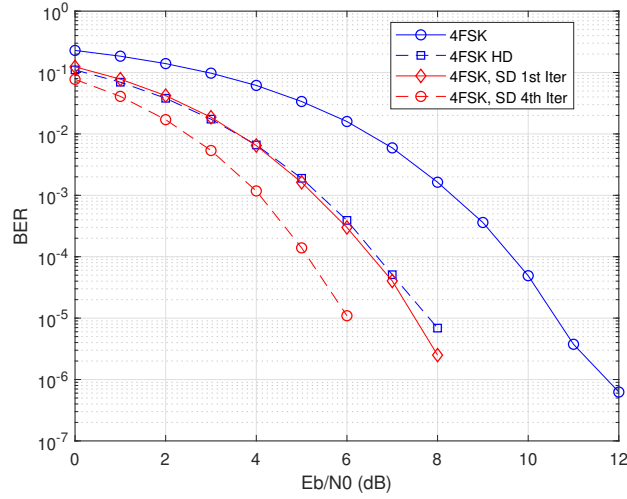


FIGURE 5.3: BER performance comparing permutation coded OFDM-4FSK scheme with the uncoded scheme in AWGN,  $L = 4$ ,  $|\mathcal{C}| = 4$ .

there exists a permutation matrix  $\mathbf{X} = [x_{ij}] \in \{0, 1\}$  such that

$$\sum_{i=1}^M x_{ij} = 1, \quad \sum_{j=1}^M x_{ij} = 1, \quad (5.14)$$

for OFDM-MFSK and a permutation matrix

$$\sum_{i=1}^M x_{ij} = h(b), \quad \sum_{j=1}^M x_{ij} = h(b), \quad (5.15)$$

for OFDM-MFSK with HPSK and solves the assignment problem

$$A_1 = \sum_{i=1}^M \sum_{j=1}^M -y_{ij} x_{ij}, \quad (5.16)$$

using the Hungarian algorithm [73].  $A_1$  is the maximum cost of  $\mathbf{Y}_1(T)$  determined by the matrix  $\mathbf{X}$ , a permutation matrix with a one '1' in positions  $\{(1, j_1), (2, j_2), \dots, (M, j_L)\}$  while other positions have zero '0'. The positions of each one '1', which is a permutation of  $j_1, j_2, \dots, j_L$  is a permutation sequence  $\mathbf{a}_1$ . Each symbol in the sequence represents the subcarrier index in each group  $M$ . Note that this method eliminates the need for (5.4) and (5.5) for detection, thereby reducing the complexity of decoding the subcarriers.

If  $\mathbf{a}_1 \notin \mathcal{C}$ , then further iterations described in [74] are performed to find the next codeword  $\mathbf{a}_2, \mathbf{a}_3, \dots, \mathbf{a}_{|\mathcal{C}|} \in \mathcal{C}$ .

## 5.4 Simulation Results

The BER of the coded OFDM-MFSK scheme is compared to that of the uncoded scheme and both schemes are non-coherently detected in AWGN and PLC channels. For the PLC channel, we choose the ratio between the power in the Gaussian noise and IN  $\frac{\sigma_G}{\sigma_I} = 0.1$  in order to simulate IN that is stronger by 10 times. The coded scheme is decoded using both HD and SD. The HD method requires a look up table to determine the likely transmitted codeword while SD uses the soft information on

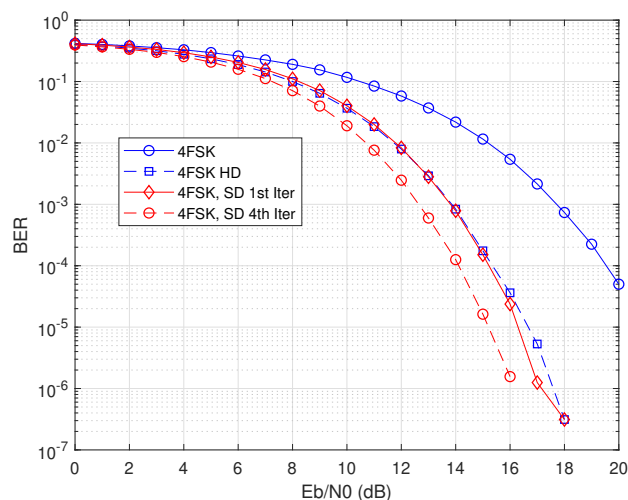


FIGURE 5.4: BER performance comparing permutation coded OFDM-4FSK scheme with the uncoded scheme in PLC,  $\frac{\sigma_G}{\sigma_I} = 0.1$ ,  $L = 4$ ,  $|C| = 4$ .

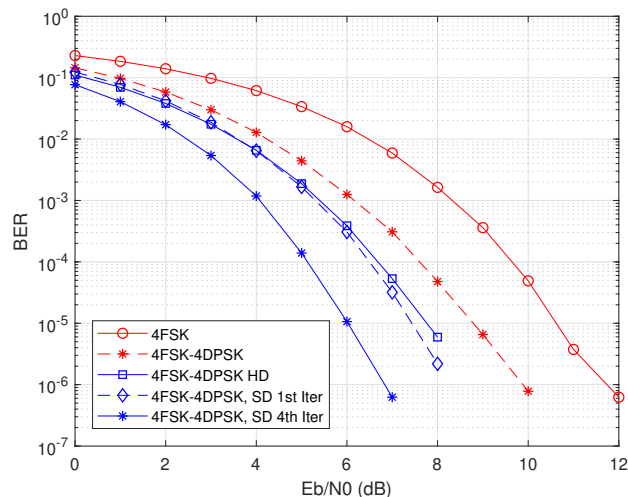


FIGURE 5.5: BER performance comparing permutation coded OFDM-4FSK-4DPSK scheme with the uncoded scheme in AWGN,  $L = 4$ ,  $|C| = 4$ .

the received subcarriers. Only the first iteration (1st Iter) and fourth iteration (4th Iter) are shown in the plots.

In the coded scheme, each information-carrying subcarrier in OFDM-4FSK is encoded by a codeword from a codebook of  $k = 4$  and  $L = 4$  and minimum Hamming distance of the codebook  $d_{\min} = 4$ . Monte Carlo simulations show in Fig. 5.3 that coded OFDM-4FSK improves the BER performance by 4 dB for the SD 4th iteration and 3 dB for the HD and SD 1st iteration in the AWGN channel. Similar coding gain is observed in Fig. 5.4 in the PLC channel with up to 5 dB at the 4th iteration and 4 dB for the HD and SD 1st iteration. The plots in Figs. 5.5 and 5.6 also compare the performances of the coded and uncoded OFDM-4FSK-4DPSK schemes in AWGN and PLC channels respectively. SD decoding of the subcarriers further improves the performance in AWGN of its hard decoded counterpart by up to 5 dB at the 4th iteration and 3 dB for the HD and SD 1st iteration. The SD 4th iteration improves the BER to approximately 6 dB in PLC (Fig. 5.4) and about 4 dB for the HD and SD 1st iteration. The worst case complexity of the SD decoder is  $O(L^4)$ , which combines the  $O(L^3)$  complexity of the Hungarian algorithm with the  $O(L^4)$  of Murty's algorithm. In Fig. 5.7, the BER of an 8FSK scheme

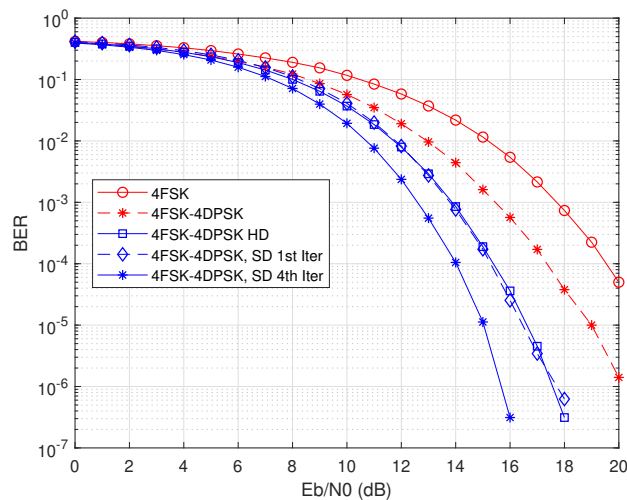


FIGURE 5.6: BER performance comparing permutation coded OFDM-4FSK-4DPSK scheme with the uncoded scheme in PLC,  $\frac{\sigma_G}{\sigma_I} = 0.1$ ,  $L = 4$ ,  $|C| = 4$ .

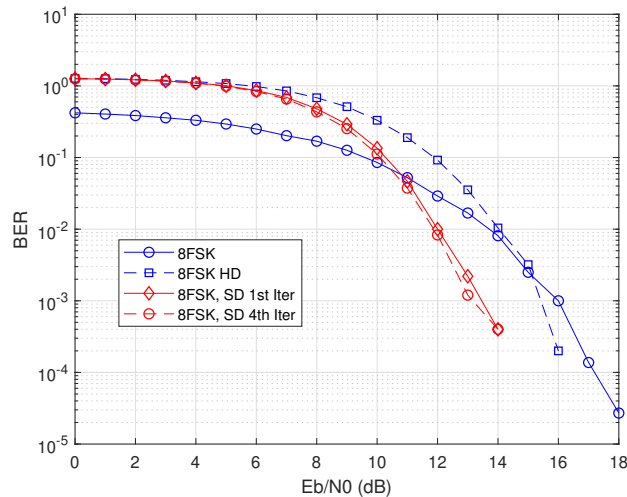


FIGURE 5.7: BER performance comparing permutation coded OFDM-8FSK-4DPSK scheme with the uncoded scheme in PLC,  $\frac{\sigma_G}{\sigma_I} = 0.1$ ,  $L = 8$ ,  $|C| = 256$ .

using  $|C| = 256$  codewords chosen from  $8!$  is shown. The coded scheme only improves the BER performance at higher SNRs in the PLC channel, while the uncoded scheme shows up to 9 dB gain at lower SNRs. This indicates the SD decoder is less attractive in scenarios where lower SNRs are required. However, for applications requiring higher SNRs, the SD is more attractive due to its low-complexity and improved performance. The spacing between the subcarriers are increased compared to the OFDM-4FSK scheme while the ratio  $\frac{|C|}{|P|}$  is small. Therefore, the HD or SD decoding is more likely to detect  $c \notin C$ .

The advantage of using permutation codes is that the encoding spreads the information across the subcarriers with spacing that could assist with avoiding noisy parts of the spectrum. The corrupted information can then be recovered by decoding the information-carrying subcarriers as a group. Therefore, if one out of  $M$  subcarriers for example, is affected by noise, the remaining  $L - 1$  subcarriers (assuming they are correctly detected) can be compared to the codebook to correct the error.

## 5.5 Conclusion

This chapter demonstrates a frequency domain coding of an OFDM-MFSK scheme using permutation codes in AWGN and PLC channels. The coding gain performance between the HD and SD decoding methods of the permutation coded scheme are presented. The coded subcarriers are soft-decoded as a group using low-complexity optimization algorithms with a combined complexity of  $O(L^4)$ . This method improves the BER performance of the OFDM-MFSK scheme in general. However, for scenarios where higher decoding complexity is attributed to codewords with longer lengths, a reasonable trade-off involving a higher SNR with lower decoding complexity can be used to increase the BER performance of the scheme. The permutation codes are used in conjunction with OFDM-MFSK to avoid bad parts of the frequency spectrum and the ability to decode subcarriers as a group rather than individually helps improve the performance of the scheme.

# Optimization Algorithms for Improving the Performance of Permutation Trellis Codes

---

**This chapter is based on the following publication:** *O. Kolade, M. Shimaponda-Nawa, D.J.J Versfeld, and L. Cheng, "Optimization Algorithms for Improving the Performance of Permutation Trellis Codes". Under revision with Elsevier Physical Communication.*

The author of this thesis conceptualized the work, performed the simulations, analyzed the results and wrote the paper.

---

## 6.1 Introduction

The error correction codes used in improving data communication over noisy channels require low-complexity, near maximum likelihood (ML) decoding performance to ensure practicality of use in their target communication systems. Permutation trellis code (PTC), which incorporates the serial concatenation of a permutation code and convolutional code is one of such codes which has been proposed to improve communication in the harsh powerline channel and cognitive radio networks. The permutation property, resulting from the combination of PTC with  $M$ -ary frequency shift keying ( $M$ -FSK) provides frequency spreading, which mitigates the effects of narrow-band interference (NBI) and impulse noise (IN) in a PLC channel [23,69,88,89]. In cognitive radio networks, PTC with  $M$ -FSK in [90,91], finds an appropriate mapping in order to increase the data rate of secondary users at low power in the presence of NBI by primary users. In addition, the ability of PTC to mitigate the effect of primary user interference is shown. In another study, the use of PTC in conjunction with quadrature amplitude modulation (QAM) and quadrature phase shift keying (QPSK) is reported [92]. In these schemes, an appropriate mapping of the binary output of the convolutional encoder to a suitable permutation codebook increases the distance between the constellation points. At the output of the channel, a soft-decision (SD), threshold detector (TD) is used in [23] to improve the performance in the PLC channel while [93] compares the performance of a range of thresholds for distance preserving PTC obtained from high order Galois fields.

In the construction PTCs, a one-to-one mapping exists between the outputs of the outer convolutional code and the codewords of the inner permutation code. While several mappings are possible, the Hamming distance between any two binary sequences and their corresponding permutation codeword are preserved, increased or decreased [23,88,94]. The symbols in the non-binary codeword can then be modulated using  $M$ -FSK, as it enables non-coherent detection, using the square law or envelope detection (ED) to select the signal with the highest energy from a pair of  $M$  quadrature correlators at each sampling period [38]. In [27], the error correction performance of the inner code of

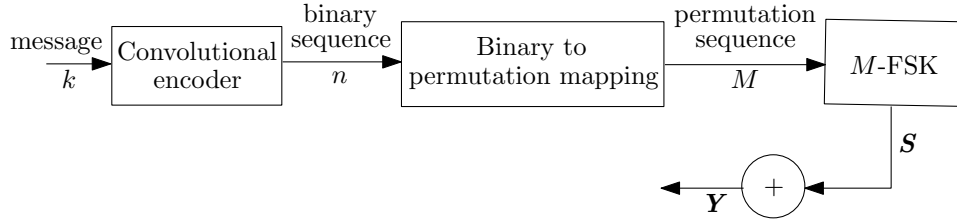


FIGURE 6.1: System model for permutation trellis encoder.

PTC is improved by optimizing the output of the channel in order to design an iterative permutation soft-decision decoder (PSDD). While the Viterbi algorithm [95] provides ML decoding of PTC, the overall error correction performance is affected by the inner code's error correction capability. In other words, the overall error correction performance is dependent on the detection scheme used at the output of the channel. SD detection of the channel output improves the performance of coded schemes in general but limited, low-complexity SD schemes exist for PTC.

In this chapter, the impact of optimization algorithms as SD decoders of PTC's inner permutation code with  $M$ -FSK is evaluated in order to improve the overall error correction performance of PTC. In order to improve the overall performance at low decoding complexity, the error correction capability of the PSDD in [27] is used in PTC. In addition, a novel SD decoder is designed using the branch and bound (BB) [96–98] algorithm. The presented SD decoders are then combined with the Viterbi decoder in two different schemes in order to improve the overall bit error rate (BER) performance. Results show that the additional step of converting the SD output to its binary equivalent before decoding with the Viterbi algorithm produces better BER performance for both decoders. The complexities of the decoders are also presented and in some cases, the SD decoder reduces the decoding complexity for large codebooks while simultaneously improving the BER performance.

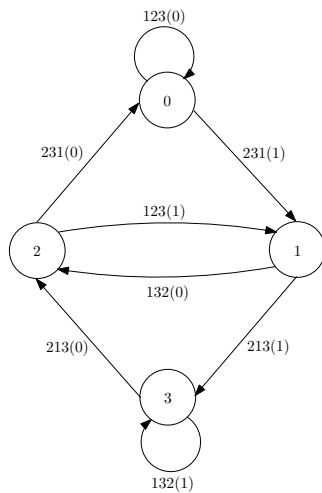
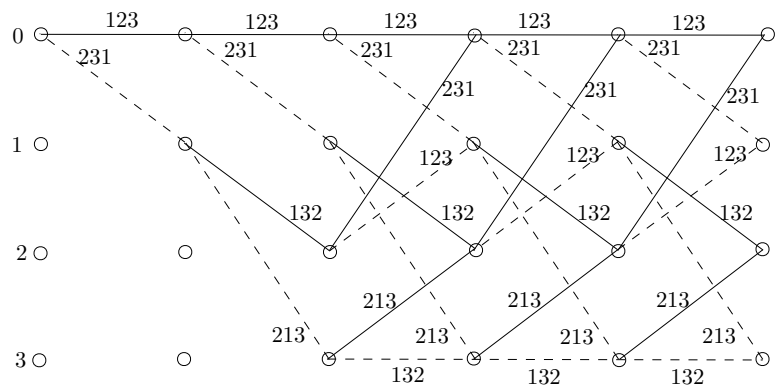
## 6.2 System Model

### 6.2.1 Permutation Trellis Codes

Permutation trellis codes combine convolutional codes and permutation codes at the encoder and are decoded using a 'modified' Viterbi decoder. A convolutional encoder with constraint length  $K$  encodes an incoming message based on a state transition diagram as shown in Fig. 6.1. Hence, every  $k$  binary bits entering the convolutional encoder produces a corresponding  $n$  bit binary sequence with a code rate of  $R_C = k/n$ . The  $n$ -tuple output from the convolutional encoder is uniquely mapped onto a codeword belonging to a permutation codebook  $\mathcal{C}$ . The codebook  $\mathcal{C}$  is a subset of all possible permutation of integers  $c_1, c_2, \dots, c_M$ . All the codewords in  $\mathcal{C}$  can be arranged in a matrix which consists of  $2^n$  rows and each row contains a codeword  $c_q$  at row  $q$  ( $1 \leq q \leq 2^n$ ). Any two codewords  $c_1, c_2$  have a Hamming distance  $d(c_1, c_2)$  between them, which is the number of positions where the two codewords differ. The permutation codebook has a minimum Hamming distance  $d_{\min}$  which is the lowest Hamming distance between all possible, distinct codeword pairs. In mapping the convolutional codeword onto the permutation codeword, the combined code rate of PTC becomes  $R_p = k/M$ . The permutation codebook is chosen such that  $n \leq M$  and the mapping is done such that the Hamming distance between each binary sequence and its respective permutation sequence is preserved, reduced or increased. Two examples of  $n = 2$  mapped onto an  $M = 3$  codebook and  $n = 3$  mapped onto an  $M = 4$  codebook are shown in Table 6.1. In Fig. 6.2, the state transition diagram of the  $n = 2, M = 3$  mapping is shown, where the non-binary sequence replaces the binary output of the convolutional encoder as an input bit (in brackets) produces an output and transition between states. The trellis representation of the code is shown in Fig. 6.3, where the dotted lines represent an input bit '1', while the solid lines in the trellis represent an input bit '0'. We refer the reader to other examples of distance increasing, reducing and preserving mappings in [23, 88, 94].

TABLE 6.1: Two sample mappings of binary outputs of convolutional code to non-binary permutation codes

$n = 2$	$M=3$	$n = 3$	$M = 4$
00	123	000	1234
01	132	001	1342
10	213	010	1423
11	231	011	2143
		100	2314
		101	2413
		110	3241
		111	3412


 FIGURE 6.2: State transition diagram for  $R_C = 1/2$  and  $R_P = 1/3$ .

 FIGURE 6.3: Trellis representation of the PTC for  $R_C = 1/2$  and  $R_P = 1/3$ .

## 6.2.2 $M$ -ary Frequency Shift Keying with PTC

Consider a set of  $M$  orthogonal signals  $s_1, s_2, \dots, s_M$ , each having one of the  $M$  different frequency components and a low pass vector representation [38]

$$\mathbf{s}_m = (\underbrace{0, \dots, 0}_{m-1}, \sqrt{E_s}, \underbrace{0, \dots, 0}_{M-m})^T. \quad (6.1)$$

The notation  $(\cdot)^T$  denotes the transpose operation and the symbol energy  $E_s$  is in the  $m$ -th ( $m = 1, 2, \dots, M$ ) position denoting the  $m$ -th frequency. The vector  $\mathbf{c}_q$  is modulated by permuting the signal  $\mathbf{s}_m$ ,  $M$  times or over  $M$  time slots. Each time slot corresponds to each integer in  $\mathbf{c}_q$  and the value of each integer indicates the position of the symbol energy. Hence, an  $M$ -FSK modulated codeword is equivalent to a permutation matrix  $\mathbf{S} = [s_{ij}] \in \{0, 1\}^{M \times M}$  of the form

$$\mathbf{S} = \begin{bmatrix} s_{11} & s_{12} & \dots & s_{1M} \\ s_{21} & s_{22} & \dots & s_{2M} \\ \vdots & \vdots & \ddots & \vdots \\ s_{M1} & s_{M2} & \dots & s_{MM} \end{bmatrix}. \quad (6.2)$$

The rows represent the  $M$  available frequencies while the columns represent the time slots. At each time slot, the position  $(i, j)$  is set to '1' if the frequency is conveying information while other positions at the same time slot are set to '0'.

Assuming perfect synchronization between the transmitter and receiver, for a transmitted coded matrix  $\mathbf{S}$ , non-coherent detection over an AWGN and PLC channel are considered. In the PLC channel, NBI and IN are common noise sources [31]. While IN may affect some or all frequencies in a time slot, NBI may affect one of the  $M$  frequencies over a period of time as illustrated in [23]. In the time domain, IN in an indoor environment occurs in short bursts and lasts for a short period of time. As a result, the occurrence may affect successive information-carrying symbols. In the case of NBI, the noise takes a frequency selective nature in which a certain frequency is affected for a certain period of time. Due to the random occurrence and short burst nature of IN, its arrival rate  $\gamma$  in units per second is used to model the Poisson process. If each IN occurs at an average duration  $T_{\text{noise}}$ , then an average of  $\gamma T_{\text{noise}}$  samples are affected by IN in 1 second and  $1 - \gamma T_{\text{noise}}$  samples are not affected by IN. At the output of the channel, each received sample can be modelled as

$$y_{ij} = \begin{cases} e^{j\phi} s_{ij} + v_G, & \text{AWGN,} \\ e^{j\phi} s_{ij} + v_G + v_I \cdot p, & \text{PLC.} \end{cases} \quad (6.3)$$

The phase  $\phi$  is a random variable, distributed uniformly between 0 and  $2\pi$ , the noise sample  $v_G$  has the Gaussian distribution  $\mathcal{CN}(0, \frac{N_0}{2})$  and  $v_I$  models the IN as a complex variable with distribution  $\mathcal{CN}(0, N_i)$ . The Poisson-distributed variable  $p$  models the occurrence of the IN with an impulsive index  $A = N_0/N_i$ , describing the power of the impulse noise  $N_i$  in terms of the Gaussian noise power  $N_0$ .

The received code matrix  $\mathbf{Y} = [y_{ij}] \in \mathcal{C}^{M \times M}$  is demodulated by comparing each column vector in  $\mathbf{Y}$  received from the output of the channel. Hence, for every transmitted vector  $\mathbf{s}_m$ , the received vector  $\mathbf{y}$  (which forms a column in  $\mathbf{Y}$ ) is demodulated using ED by choosing the  $\mathbf{s}_m$  with the highest envelope

$$r = \arg \max_{m \in M} |\mathbf{y}^H \cdot \mathbf{s}_m|. \quad (6.4)$$

This produces an integer  $r$  which is equivalent to the likely transmitted  $m$ -th frequency, hence a permutation of integers  $\mathbf{r} = r_1, r_2, \dots, r_M$  per transmitted codeword. A more adequate threshold detector proposed in [23] sets a threshold of  $\tau = 0.6\sqrt{E_s}$  on the received samples, such that

$$r_{ij} = \begin{cases} 1, & \text{if } \bar{y}_{ij} \geq \tau, \\ 0, & \text{otherwise.} \end{cases} \quad (6.5)$$

where  $\bar{y}_{ij} = |y_{ij}|$ . This results in an  $M \times M$  matrix  $\mathbf{R} = [r_{ij}] \in \{0, 1\}^{M \times M}$  equivalent to a transmitted signal  $\mathbf{S}$ .

### 6.2.3 Probability of Error of PTC

Consider a set of transmitted code matrices  $\mathbf{S}^1, \mathbf{S}^2, \dots, \mathbf{S}^V$  which are received over an AWGN channel and demodulated as  $\mathbf{R}^1, \mathbf{R}^2, \dots, \mathbf{R}^V$ . For each transmitted code matrix  $\mathbf{S}^v$  ( $v = 1, 2, \dots, V$ ), received and demodulated as  $\mathbf{R}^v$ , the probability of erroneously receiving the  $n$ -tuple symbols encoded as  $\mathbf{S}^v$  is given as [90]

$$P_e = \frac{1}{M} \sum_{i=1}^{2^n} \sum_{v=1}^{2^{M^2}} P(\mathbf{D} = \mathbf{S}^v | \mathbf{R}^v) \cdot P(\mathbf{R}^v | \mathbf{S} = \mathbf{S}^v), \quad (6.6)$$

where  $P(\mathbf{R}^v | \mathbf{S} = \mathbf{S}^v)$  is the likelihood of receiving  $\mathbf{R}^v$  if  $\mathbf{S}^v$  is transmitted and is given as

$$P(\mathbf{R}^v | \mathbf{S} = \mathbf{S}^v) = \prod_{i=1}^M \prod_{j=1}^M \left( \prod_{w=1}^W P(\bar{y}_{ij} \geq \tau | s_{ij}) \right) \left( \prod_{u=1}^U P(\bar{y}_{ij} < \tau | s_{ij}) \right), \quad (6.7)$$

where  $U$  and  $W$  are the number of zeros ('0's) and ones ('1's) respectively in  $\mathbf{R}^v$ .  $P(\mathbf{D} = \mathbf{S}^v | \mathbf{R}^v)$  is the probability of a correct decision because code matrix  $\mathbf{D}$ , which has the minimum Hamming distance with the received code matrix  $\mathbf{R}^v$  is transmitted. The probabilities in (6.6) and (6.7), derived in [90,91] are given as

$$P(\bar{y}_{ij} \geq \tau | s_{ij} = 1) = Q_1 \left( \sqrt{2 \frac{E_s}{N_0}}, 0.6 \sqrt{2 \frac{E_s}{N_0}} \right), \quad (6.8)$$

$$P(\bar{y}_{ij} < \tau | s_{ij} = 1) = 1 - P(\bar{y}_{ij} \geq \tau | s_{ij} = 1), \quad (6.9)$$

$$P(\bar{y}_{ij} \geq \tau | s_{ij} = 0) = \exp \left( -0.36 \frac{E_s}{N_0} \right), \quad (6.10)$$

and

$$P(\bar{y}_{ij} < \tau | s_{ij} = 0) = 1 - P(\bar{y}_{ij} \geq \tau | s_{ij} = 0). \quad (6.11)$$

Note that the SNR per symbol  $E_s/N_0$  is the ratio of the received signal energy  $E_s$  to the noise power spectral density  $N_0$ ,  $Q_1(\alpha, \beta) = \int_{\beta}^{\infty} x \exp\{-\frac{x^2 + \alpha^2}{2}\} I_0(\alpha x) dx$  is the Marcum  $Q$ -function [99] and  $I_0(\alpha x)$  is the zeroth order of the modified Bessel function. The derived  $P_e$  in (6.6), henceforth referred to as the analytical hard decision (HD) decoder gives the probability of error for a transmitted symbol  $n$ . The symbol  $n$  is produced by the convolutional encoder and because  $P_e$  does not take the Viterbi decoder into consideration, some coding gain is lost. The convolutional code is an encoder with memory since the current sequence is determined by the previously encoded sequence. Hence, the decoder decodes the output of the demodulator as a chain of events. In order to simplify the probability of error of the Viterbi decoder, the all-zero path is assumed to be transmitted. Therefore, the code's free distance  $d_{\text{free}}$  which is the path which departs the all-zero path and first merges with the all-zero path is assumed to contain errors when compared with the transmitted all-zero path. As a result the probability of error is bounded as [38]

$$P_{e,CC} \leq \sum_{d=d_{\text{free}}}^{\infty} a_d P_2(d), \quad (6.12)$$

where  $P_2(d)$  describes the probability of the decoded path having a Hamming distance of  $d$  bits with the transmitted codeword. When the binary convolutional code is mapped onto the non-binary permutation codeword, the Viterbi hard decision decoder's  $P_{e,CC}$  is modified as

$$P_{e,CC}^c \leq \sum_{d=d'_{\text{free}}}^{\infty} a_d^c P_2^c(d), \quad (6.13)$$

where  $a_d^c$  and  $P_2^c(d)$  are similar to  $a_d$  and  $P_2(d)$  in (6.12) but correspond to the permutation codeword  $\mathbf{c}_q$  mapped to a convolutional codeword,  $d'_{\text{free}}$  is the free distance of the non-binary code. Using the example mappings in Table 6.1, the all-zero sequence is equivalent to 123 for  $M = 3$  and 1234 for  $M = 4$ . Hence,  $a_d^c$  describes the paths with a Hamming distance of  $d$  when compared with the transmitted permutation codeword equivalent to the corresponding all-zero codeword. If the path in error consists of  $V$  stages, then a concatenation of matrices  $\mathbf{R}^1, \mathbf{R}^2, \dots, \mathbf{R}^V$  are received for transmitted code

matrices  $\mathbf{S}^1, \mathbf{S}^2, \dots, \mathbf{S}^V$ . Therefore, the probability  $P_2^c(d)$  is defined as

$$P_2^c(d) = \begin{cases} \sum_{d_H(\mathbf{S}^v, \mathbf{R}^v) = \frac{d}{2} + 1}^d \prod_{v=1}^V P(\mathbf{R}^v | \mathbf{S}^v), & \text{odd } d, \\ \sum_{d_H(\mathbf{S}^v, \mathbf{R}^v) = \frac{d}{2} + 1}^d \prod_{v=1}^V P(\mathbf{R}^v | \mathbf{S}^v) + \frac{1}{2} \prod_{v=1}^V P(\mathbf{R}^v | \mathbf{S}^v) & \text{even } d, \end{cases} \quad (6.14)$$

where  $\mathbf{S}^v$  and  $\mathbf{R}^v$  are the transmitted and received matrices respectively at each stage  $v$  in the trellis. At each stage of the trellis, the decoder computes the metric

$$d_H(\hat{\mathbf{S}}^v, \mathbf{R}^v) = M - \left( \sum_{1 \leq i, j \leq M} (s_{ij} \wedge r_{ij}) \right), \quad (6.15)$$

between the received matrix  $\mathbf{R}^v$  and each branch  $\hat{\mathbf{S}}^v$ . The decoder chooses the branch with the smallest metric, where the notation  $\wedge$  is the binary AND operation. As a result, at each stage  $v$  of the trellis, the probability of error  $P(\mathbf{R}^v | \mathbf{S}^v)$  can be evaluated as pairwise, hence a function of the difference between  $\mathbf{R}^v$  and  $\mathbf{S}^v$  and is defined as

$$P(\mathbf{R}^v | \mathbf{S}^v) = \frac{1}{2} \operatorname{erfc} \left( \sqrt{\frac{R_p E_s}{M N_0} d_H(\mathbf{S}^v, \mathbf{R}^v)} \right), \quad (6.16)$$

where  $\operatorname{erfc}(x)$  is the complementary error function of  $x$ .

## 6.2.4 The Permutation Soft-Decision Decoder

As mentioned earlier, a permutation codeword of length  $M$  permutes the MFSK signal in (6.1)  $M$  times. In each transmitted codeword matrix  $\mathbf{S}$ , all  $M$  frequencies carry information such that each frequency is activated once in each row and column. When the received signal is affected by AWGN or PLC channel noise, the PSDD solves the general assignment problem by minimizing

$$Z_g = \sum_{i=1}^M \sum_{j=1}^M \hat{y}_{ij} s_{ij}, \quad (6.17)$$

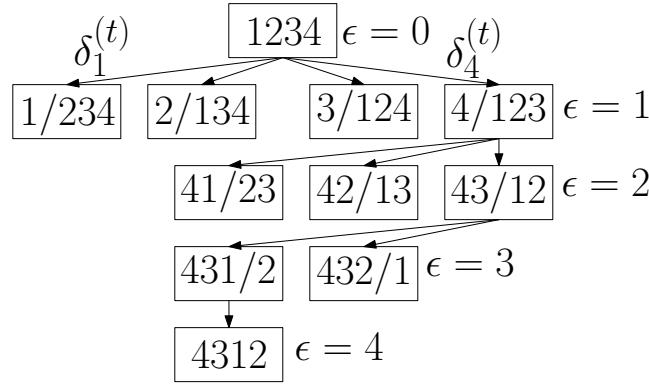
where  $\hat{y}_{ij} = -|y_{ij}|$ ,  $Z_g$  is the cost at iteration  $g$  and (6.17) is subject to

$$\sum_{i=1}^M s_{ij} = \sum_{j=1}^M s_{ij} = \sqrt{E_s}, \quad (6.18)$$

for  $i = 1, 2, \dots, M, j = 1, 2, \dots, M$ . The Hungarian algorithm (HA) [73] can find the matrix  $\mathbf{S} = [s_{ij}]$  that produces the minimum cost  $Z_1$  with a corresponding row-column representation of the permutation sequence

$$\{(1, j_1), (2, j_2), \dots, (M, j_M)\}, \quad (6.19)$$

where  $j_1, j_2, \dots, j_M$  is a permutation of integers  $1, 2, \dots, M$ . If the codeword corresponding to cost  $Z_1$  produces a codeword  $c \notin C$ , then the PSDD proceeds to the next iteration  $g = 2$ . Using Murty's algorithm [74], the PSDD ranks  $Z_2, Z_3, \dots, Z_{2^n}$  in order to find a codeword  $c \in C$ . Using the solution matrix from  $Z_1$ ,  $n-1$  non-empty subsets of  $\mathbf{Y}$  form nodes  $N_1, N_2, \dots, N_{n-1}$ , by partitioning  $a_1$ . Nodes


 FIGURE 6.4: Tree-based method to decode permutation codes using branch and bound with  $M = 4$ .

in this case are defined as

$$\begin{aligned}
 N_1 &= \{\overline{(1, j_1)}\}, \\
 N_2 &= \{(1, j_1), \overline{(2, j_2)}\}, \\
 &\vdots \\
 N_{n-1} &= \{(1, j_1), \dots, \overline{(n-1, j_{n-1})}\}.
 \end{aligned} \tag{6.20}$$

Row-column pairs with the bar ( $\overline{(\cdot, \cdot)}$ ) indicate row-column elements to be replaced with  $\infty$  while row-column elements without the bar are removed from  $\mathbf{Y}$ . The minimum cost is then solved for each node and the node with the least cost forms the next assignment  $a_2$ .

The PSDD makes an optimal decision (OD) by using a brute force to find the codeword  $\mathbf{c}$  from all possible permutations with the highest cost

$$Z_{\text{OD}} = \arg \min_{\mathbf{c}_q \in \mathcal{C}} \sum_{i=1}^M \sum_{j=1}^M \hat{y}_{ij} s_{ij}^{(\mathbf{c}_q)}, \quad \text{for } 1 \leq q \leq 2^n, \tag{6.21}$$

where  $s_{ij}^{(\mathbf{c}_q)}$  is each element in the permutation matrix produced by a codeword  $\mathbf{c}$ .

## 6.3 Proposed Soft-Decision Decoder and Schemes

### 6.3.1 Branch and Bound

In order to solve  $\mathbf{Y}$  using branch and bound (BB), a set of  $M+1$  levels  $\epsilon = 0, 1, 2, \dots, M$  are created and at each level  $\epsilon > 0$ , there exists nodes  $t = 1, 2, \dots, M - \epsilon + 1$  each with cost  $\delta_\epsilon^{(t)} = \delta_\epsilon^{(1)}, \delta_\epsilon^{(2)}, \dots, \delta_\epsilon^{(M-\epsilon+1)}$  respectively. At  $\epsilon = 0$ , there exists an initial node containing all integers  $\{c_1, c_2, \dots, c_M\}$  in no specific order and none of the  $M$  jobs is yet assigned. An example of BB as an SD technique to solve an assignment problem is shown using a state space tree in Fig. 6.4 with  $M = 4$ . For simplicity, the initial node for  $M = 4$  is 1234 and nodes 1/234, 2/134 up to 4/123 are obtained at  $\epsilon = 1$ . The node  $t$  with the minimum cost  $\hat{\delta}_\epsilon^{(t)}$  at  $\epsilon = 1$  with the minimum value from the  $M$  branches is scheduled if

$$\hat{\delta}_\epsilon^{(t)} = \min_{1 \leq t \leq M} (\hat{y}_{et} + \sum_{i,j} \hat{y}_{ij}), \quad \epsilon = 1, 2 \leq i \leq M, 0 < j \leq M : j \neq t. \tag{6.22}$$

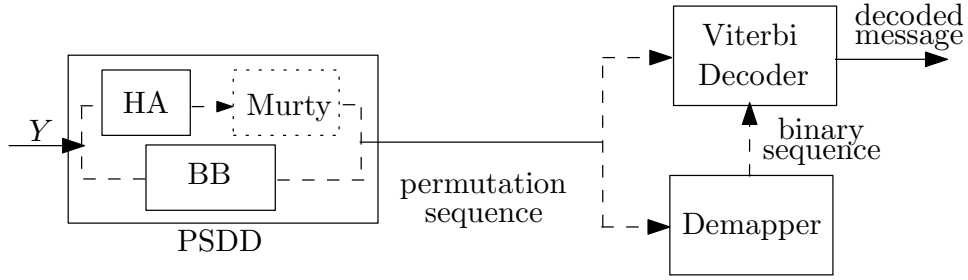


FIGURE 6.5: Decoder system model of permutation code soft-decision and permutation trellis decoder.

The other nodes are pruned while the surviving node  $\hat{t}_\epsilon$  at  $\epsilon = 1$  satisfying (6.22) is divided into  $M - \epsilon$  branches at the next level. At nodes  $\epsilon > 1$ , the surviving node at each level

$$\hat{\delta}_\epsilon^{(t)} = \min_{1 \leq t \leq M} (\hat{y}_{(\epsilon-1)\hat{t}_{(\epsilon-1)}} + \hat{y}_{\epsilon t} + \sum_{i,j} \hat{y}_{ij}), \quad \epsilon > 1, \epsilon + 1 \leq i \leq M, 1 \leq j \leq M : j \neq t, j \notin \hat{t}, \quad (6.23)$$

where  $\hat{t}$  contains an ordered set of scheduled nodes. This process of pruning and branching is done until the last level at which only one assignment is possible.

### 6.3.2 Schemes

As shown in Fig. 6.5, the PSDD uses BB or HA and Murty algorithms to decode  $Y$ , hence the dashed lines. The dotted lines around the Murty block indicates the Murty algorithm is only used when  $c \notin \mathcal{C}$  at HA. Otherwise, the Murty step is skipped.

#### 6.3.2.1 Scheme 1

The channel output  $Y$  is decoded using HA ( $g = 1$ ) and Murty ( $2 \leq g \leq M$ ). The codeword matrix which maximizes (6.17) is then decoded using the Viterbi decoder. If HA produces a sequence  $c \notin \mathcal{C}$ , Murty iterates until  $c \in \mathcal{C}$  or the specified maximum number of iterations is reached.

#### 6.3.2.2 Scheme 2

Here, the Viterbi decoder is used to decode the binary output from the permutation to binary code demapper. The PSDD produces a permutation code  $c$  that is demapped to its binary equivalent. If the final iteration of the PSDD produces a codeword  $c \notin \mathcal{C}$ , minimum distance decoding between  $c$  and all codewords in  $\mathcal{C}$  is performed before demapping. This binary output is then decoded using the Viterbi decoder.

#### 6.3.2.3 Schemes 3 & 4

In Scheme 3, the channel output  $Y$  or demodulated  $\bar{Y}$  is decoded with BB to solve for  $Z_1$ . The permutation sequence produced is then forwarded to the Viterbi decoder. In Scheme 4, the permutation sequence produced by BB is demapped to its binary equivalent and forwarded to the Viterbi decoder, similar to Scheme 2. BB uses a single iteration, hence only  $Z_1$  is solved in Schemes 3 and 4.

In the case where the threshold detector is used at the demodulator, the SD algorithms can also be applied to demodulated bits. As an example, consider a transmitted codeword 3214. The demodulated

codeword matrix  $\bar{\mathbf{Y}}_I$  affected by impulse noise at time  $t_4$  can be represented as

$$\bar{\mathbf{Y}}_I = \begin{matrix} & t_1 & t_2 & t_3 & t_4 \\ \begin{bmatrix} 0 & 0 & \boxed{1} & 1 \\ 0 & \boxed{1} & 0 & 1 \\ \boxed{1} & 0 & 0 & 1 \\ 0 & 0 & 0 & \boxed{1} \end{bmatrix} & \text{or } \bar{\mathbf{Y}}_N = \begin{matrix} & t_1 & t_2 & t_3 & t_4 \\ \begin{bmatrix} 1 & 1 & \boxed{1} & 1 \\ 0 & \boxed{1} & 0 & 0 \\ \boxed{1} & 0 & 0 & 0 \\ 0 & 0 & 0 & \boxed{1} \end{bmatrix} & \begin{matrix} f_1 \\ f_2 \\ f_3 \\ f_4 \end{matrix} \end{matrix}, \quad (6.24)$$

when affected by NBI at  $f_1$ .  $\bar{\mathbf{Y}}_I$  and  $\bar{\mathbf{Y}}_N$  can be easily solved using the PSDD to produce the codeword 3214 as shown by the boxed values. The codeword can then be decoded using the Viterbi algorithm.

## 6.4 Simulation Results and Complexity Analysis

We compare the simulated BER of the PTC decoder with BERs obtained from the proposed decoding schemes discussed in Section 6.3.2. The BER is calculated as the difference between the transmitted message bits and decoded bits over an AWGN and PLC channel. In the AWGN channel, the schemes are compared with the analytical expressions in 6.14 - 6.16. The  $d_{\text{free}}$  bound plots show the lower bound performance of the PTC decoder, since the all-zero path is compared with the  $d_{\text{free}}$  path, hence the coding gain when compared with our simulations. Different PTC mappings are simulated, with three different codes. The first code has a rate  $R_C = 1/2$  mapped onto  $M = 3$ , the second has a rate  $R_C = 2/3$  mapped onto  $M = 4$  codebook while the third is a distance preserving mapping from  $R_C = 1/4$  onto an  $M = 4$  codebook. The first is generated from  $K = 3$ , with an octal generator polynomial (7 5) while the second is generated from  $K = 4$ , with an octal generator polynomial (1 3 0; 3 2 3). The mappings of both codes have been shown in Table 6.1. The third code is generated from  $R_C = 1/4$ ,  $K = 6$ , with an octal generator polynomial (53 67 71 75). The third code is mapped onto a distance preserving permutation codebook of  $M = 4$ . The SNR per bit  $E_b/N_0$  of the system for bit energy  $E_b$  is defined as

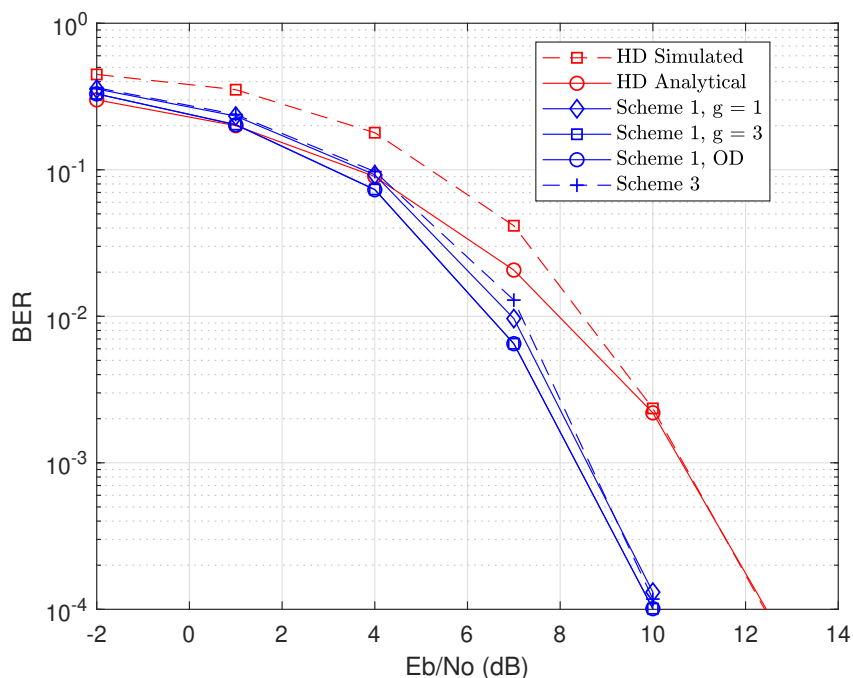
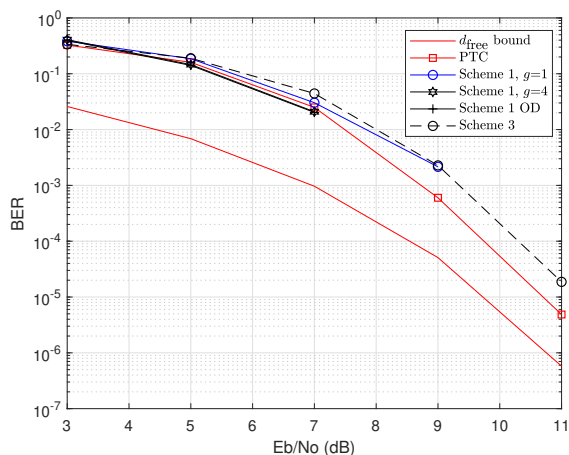
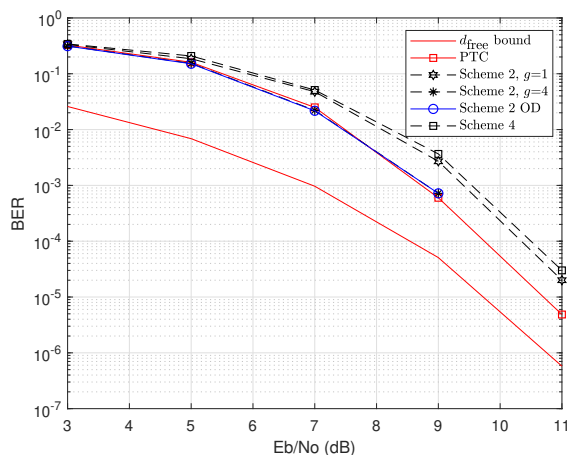
$$\frac{E_b}{N_0} = \frac{E_s}{N_0 \times R_P \times \log_2 M}. \quad (6.25)$$

For the PLC channel, we adopt the heavily disturbed channel scenario in [45] where the Inter Arrival Times (IAT) is 0.0196s while  $T_{\text{noise}}$  is 0.0641ms.

Fig. 6.6 compares the performance of the analyzed HD decoder in (6.6) with the SD decoders. The simulated HD plot matches the analytical at higher SNRs, while the SD decoders improve the coding gain by about 2 dB. The BB method in Scheme 3 shows a slightly poorer performance when compared with Scheme 1 at lower SNRs. Results in Figs. 6.7 and 6.8 show tight BER performance between the modified PTC decoder and the SD schemes. The BER of the Viterbi decoder when the all-zero codeword is compared with the  $d_{\text{free}}$  path, as described in (6.13) is also shown in 6.7 and 6.8 as the  $d_{\text{free}}$  bound. This bound can be considered as a lower bound. When  $M$  is increased in Figs. 6.9 and 6.10, the BER coding gains obtainable from Schemes 1 and 2 become more evident with up to 3 dB gain at  $g = 4$ . Figs. 6.11 and 6.12 show significant BER improvement in the PLC channel with Schemes 3 and 4 performing close to the OD of Schemes 1 and 2.

### 6.4.1 BER Performance and $\frac{2^g}{M!}$ Ratio

The SD decoders presented provide the advantage of always outputting a permutation of integers by solving an assignment problem. In Figs. 6.7 - 6.10, the PTC decoder produces better BER performance than the SD schemes at  $g = 1$ . More iterations such as  $g = 4$  are required to produce  $c \in \mathcal{C}$  compared to  $g = 1$  in order to obtain BER closer to the PTC decoder as seen in Figs. 6.7 - 6.9 and better than the PTC decoder as seen in Fig. 6.10. The SD decoder's probability of producing a codeword  $c \in \mathcal{C}$  can be described by the ratio  $\frac{2^g}{M!}$ . Hence, the performance of the schemes approaches the OD performance


 FIGURE 6.6: BER comparisons of HD with SD schemes for code having  $R_C = 1/2$  and  $M = 3$ .

 FIGURE 6.7: Schemes 1 & 3 with Viterbi decoding of PTC codewords for  $R_C = 1/2$  and  $M = 3$  in AWGN channel.

 FIGURE 6.8: Schemes 2 & 4 with Viterbi decoding of demapped codewords for  $R_C = 1/2$  and  $M = 3$  in AWGN channel.

as  $2^n$  increases. For example, in the plots in Figs. 6.11 and 6.12, the  $2^n$  unique binary sequences are mapped onto a codebook with  $M = 4$ . Since  $\frac{2^n}{M!} = 0.667$ , each scheme of the SD decoders is more likely to choose a codeword  $c \in \mathcal{C}$ . Schemes 2 and 4 further improve the performance of the SD because the demapping process chooses one of the  $2^n$  possible binary sequences using Hamming distance decoding. In Schemes 1 and 3, the codeword matrix produced by the SD decoder likely belongs to  $M!$  possible permutations rather than the encoder's  $2^n$  due to errors. Since  $2^n < M!$ , the probability of error of the schemes using demapping is lower especially at lower SNRs.

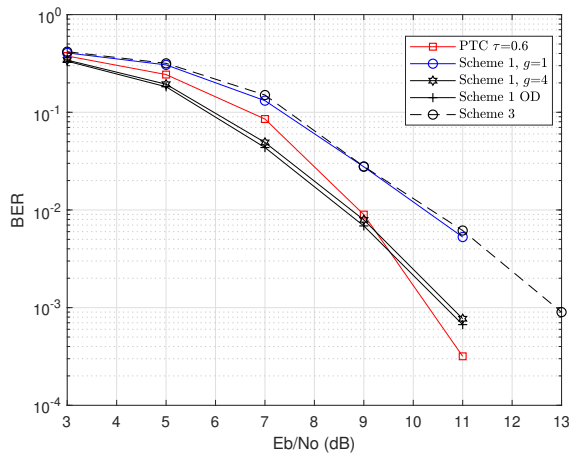


FIGURE 6.9: Schemes 1 & 3 with Viterbi decoding of PTC codewords for  $R_C = 2/3$ ,  $M = 4$  and  $A = 0.1$  in PLC channel.

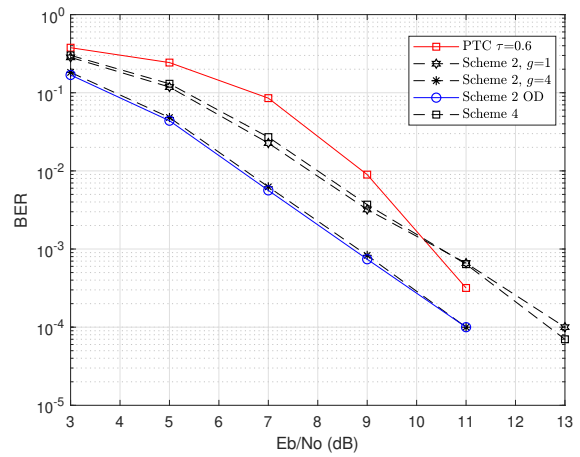


FIGURE 6.10: Schemes 2 & 4 with Viterbi decoding of demapped codewords for  $R_C = 2/3$ ,  $M = 4$  and  $A = 0.1$  in PLC channel.

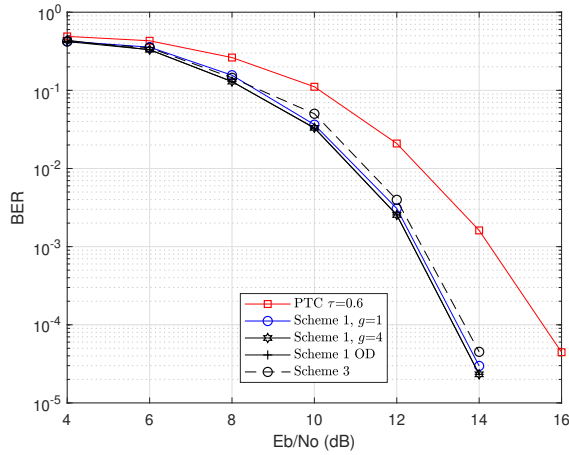


FIGURE 6.11: Schemes 1 & 3 with Viterbi decoding of PTC codewords for  $R_C = 1/4$ ,  $M = 4$  and  $A = 0.1$  in PLC channel.

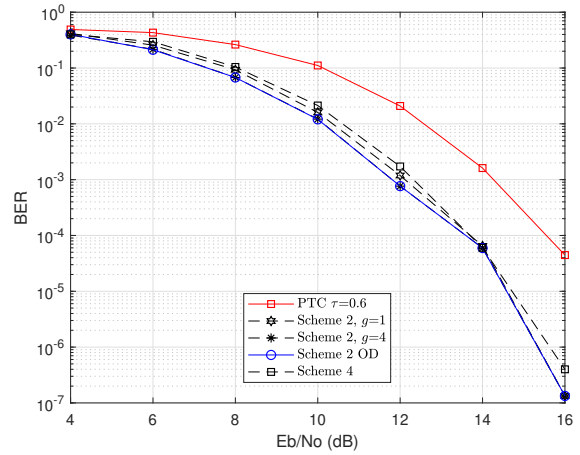


FIGURE 6.12: Schemes 2 & 4 with Viterbi decoding of demapped codewords for  $R_C = 1/4$ ,  $M = 4$  and  $A = 0.1$  in PLC channel.

## 6.4.2 Complexity Analysis

In order to analyze the different complexities of the decoder, operations required to process the digital signal are considered. The complexity of the circuitry required for the processing are not considered in this work. For each received coded signal at the output of the channel, the TD requires a complexity of  $O(M^2)$  to decide if each sample in the  $M \times M$  matrix is above or below the threshold. For the PSDD, the complexity of the iterative decoder in Scheme 1 and 2 is  $O(M^3)$  at  $g = 1$  and  $O(M^4)$  for  $2 \leq g \leq M$ . When  $g > 1$ , the complexities sum up, hence a worst case complexity of  $O(M^4)$  [77]. At each level of the tree-based BB method in Fig 6.4 and (6.22),  $M$  different computations are required on all the  $M$  nodes in order to find the minimum cost at each level. Since the number of nodes to process reduce at each level, the worst case complexity is considered and can be approximated as  $O(M^3 \log M)$  [100]. Schemes 2 and 4 require a lookup process to demap to the binary equivalent at a complexity of  $O(M \log M)$ .

## 6.5 Conclusion

The design of four decoding schemes which combine three optimization algorithms to improve the BER performance of the PTC decoder is presented. The complexities of the different components of the decoding schemes are also analyzed. Demapping the permutation sequence to its binary equivalent before decoding with the Viterbi decoder produces the best BER coding gain when compared to the PTC decoder. The BER coding gains obtained from the schemes increase as the ratio of the permutation codebook length to all possible permutations increases. While the improved BER coding gain is at the expense of additional complexity, a reasonable trade-off can be considered when the permutation codebook contains large codewords. While multitone  $M$ -FSK has been established to improve the data rate of the  $M$ -FSK scheme, future work will require techniques for increasing the data rate of permutation-coded  $M$ -FSK.

# Permutation-Aided Space-Time Shift Keying for Indoor Visible Light Communication

---

**This chapter is based on the following publication:** *O. Kolade and L. Cheng, "Permutation-Aided Space-Time Shift Keying for Indoor Visible Light Communication", IEEE SmartGridComm, Oct 2019.*

The author of this thesis conceptualized the work, performed the simulations, analyzed the results and wrote the paper.

---

## 7.1 Introduction

Multiple-input multiple-output (MIMO) systems take advantage of the spatial diversity offered by multiple antenna elements (AEs) while increasing the data rate when compared to single-input single-output (SISO) counterparts. Space shift keying (SSK) [101, 102] extends spatial modulation (SM) [49, 103, 104] by selecting a number from AEs for transmission from a set of available AEs at each symbol period. Unlike in conventional MIMO which uses all AEs at each symbol period to transmit different messages, SSK provides the advantage of eliminating inter-channel interference (ICI), however at a reduced data rate. Since one AE is activated at each symbol period, the complexity of SSK's maximum likelihood (ML) decoder is similar to the single-AE ML detection.

Space-time shift keying (STSK) [24, 25, 105] further combines SM and SSK by adding time diversity to the existing spatial diversity. STSK activates one out of  $Q$  available space-time matrices to transmit data symbols without ICI. However, the STSK schemes proposed in [24, 25] require knowledge of the channel state information (CSI) in order to detect the transmitted symbols. The differential STSK (D-STSK) in [24] is further shown to eliminate the need for CSI but adds the Cayley transform complexity to the encoding of the data symbols. The D-STSK scheme requires a random search for the required activation matrices which are only capable of transmitting one symbol per transmit block. Differential spatial modulation (DSM) [106, 107] provides a similar scheme to D-STSK by also selecting one permutation matrix per transmit block with the capability of transmitting more than one symbol per transmit block. While D-STSK and DSM are less complex compared to SM, the ML decoding complexity of the schemes become too complex as the number of AEs become large. The modulation order which assists with increasing the data rate of DSM further introduces a higher detection complexity as the modulation order increases.

Powerline communication is identified as an integral part in the successful deployment of smart grid technologies. Since VLC luminaries as shown in Fig. 7.1 are powered by powerline cables, an integration of PLC with VLC [14, 22, 53, 54] can further extend the robustness and applications of smart grid

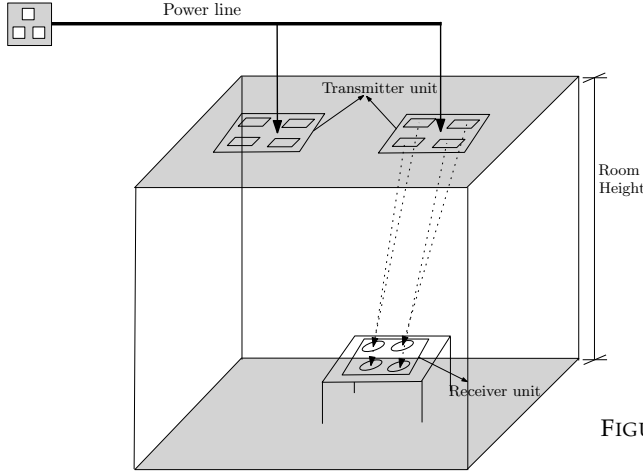


FIGURE 7.1: Room dimensions with transmitter and receiver arrangement.

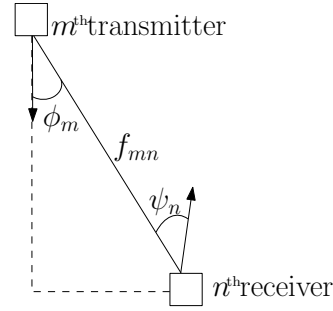


FIGURE 7.2: Geometric model of transmitter LED and receiver PD.

technologies. However, indoor illumination installations have light emitting diodes (LED) closely packed together, naturally providing multiple AEs for MIMO VLC [2, 108, 109]. In environments where cross-talk between LEDs needs to be eliminated, SSK [110] and STSK schemes in VLC are proposed.

In this chapter, a permutation-aided STSK scheme which uses a  $\{0, 1\}$  permutation matrix similar to DSM is used in an indoor MIMO VLC. The permutation matrix is determined by a codeword selected from a permutation codebook. Similar to index modulation, the non-zero elements in the permutation matrix determine the LED that is switched on at each time slot while the switched on LED simultaneously conveys additional information mapped onto an  $M$ -ary modulation scheme. In an indoor setup, the receiver interprets the received soft samples as an assignment problem. Optimization algorithms are then used to detect the received soft samples. The data rate of this scheme can be increased by increasing the number of codewords and the constellation order without necessarily increasing the number of transmit LEDs. Increasing the number of codewords however increases the complexity of the ML detection. The proposed soft-decision (SD) receiver is iterative and reduces the complexity of the ML detection, thereby providing an attractive option for large number of LEDs and increased data rate. The SD algorithm is also capable of detecting without the CSI. For a chosen data rate and a codebook's minimum Hamming distance matched with an appropriate modulation order, a reasonable trade-off between the BER performance and the achievable data rate can be obtained from the scheme. Simulation results are presented in an indoor environment by comparing the BER performance of the ML detection with soft-detection both with and without the CSI.

## 7.2 System Model

Consider an indoor MIMO VLC system consisting of  $P$  Lambertian LEDs as transmitters and  $N$  photodiodes (PD) as receivers. The direct current (DC) gain between the  $p$ -th LED and  $n$ -th photodiode is defined as [55]

$$h_{pn} = \begin{cases} \frac{(b+1)A_{pd}}{2\pi f_{pn}^2} \cos^b(\phi_p) \cos(\psi_n), & \text{for } 0 \leq \psi_n \leq \Psi_c \\ 0, & \psi_n > \Psi_c, \end{cases} \quad (7.1)$$

where the Lambertian emission order  $b = \frac{-\ln 2}{\ln(\cos \Phi_{1/2})}$  for a semi-angle  $\Phi_{1/2}$ ,  $A_{pd}$  describes the area of the  $n$ -th PD,  $f_{pn}$  is the distance between the  $p$ -th LED and the  $n$ -th PD,  $\phi_p$  and  $\psi_n$  are the transmitter's and receiver's angle of incidence respectively while  $\Psi_c$  is the receiver's field of view as shown in Fig.

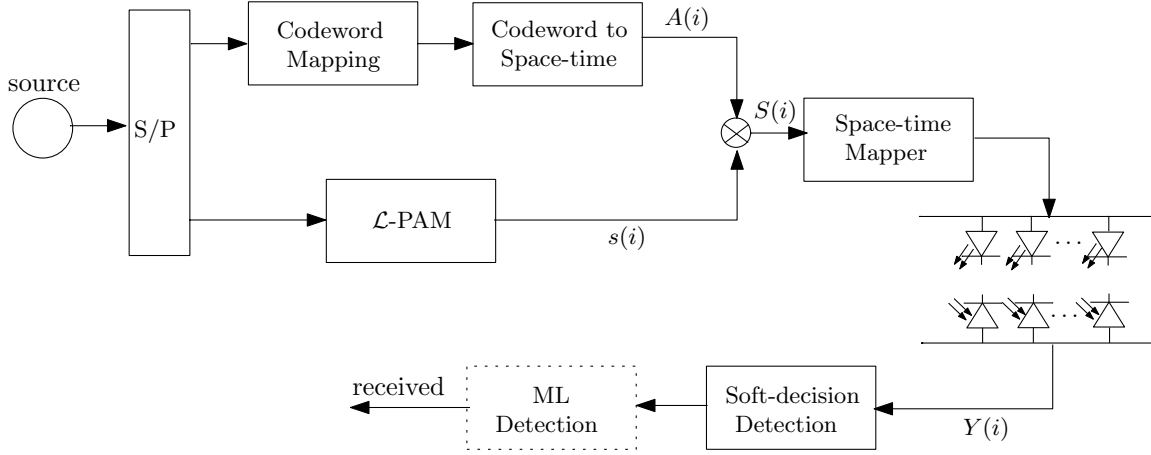


FIGURE 7.3: System model for permutation-aided STSK with soft-detection.

7.2. The source information to be transmitted over the LEDs in Fig. 7.3 are mapped to a space-time code block  $\mathbf{S}(i) = s(i) \cdot \mathbf{D}(i)$  where  $i$  represents the index of the block. The signal  $\mathbf{S}(i)$  consists of the constellation point  $s(i)$  from unipolar  $M$ -PAM or any conventional unipolar modulation scheme while  $\mathbf{D}(i)$  is chosen from a set of dispersion matrices  $\mathbf{D}_q (q = 1, 2, \dots, Q)$ . The received signals at the photodiodes can be modelled as

$$\mathbf{Y}(i) = \mathbf{H}(i)\mathbf{S}(i) + \mathbf{N}(i), \quad (7.2)$$

where  $\mathbf{Y}(i) \in \mathbb{R}^{N \times T}$  is the received  $i$ -th block, each element in  $\mathbf{H}(i) \in \mathbb{R}^{N \times P}$  is described in (7.1),  $\mathbf{S}(i) \in \mathbb{R}^{P \times T}$  describes the permutation-aided space-time signal block and  $\mathbf{N}(i) \in \mathbb{R}^{N \times T}$  models background, shot and thermal noise at the receiver modelled as an additive white Gaussian noise with zero mean and noise power  $\sigma^2$ .

The ML detector selects the combination  $(q, l)$  representing the input bits that maximizes [49]

$$(q_{\text{ML}}, l_{\text{ML}}) = \arg \max_{\mathbf{S}(i)} P(\mathbf{Y}(i) | \mathbf{S}(i), \mathbf{H}(i)), \quad (7.3)$$

and adapting the ML detection proposed in [49] which finds the  $q$  and  $l$  combination, assuming perfect CSI knowledge of  $\mathbf{H}(i)$

$$(q_{\text{ML}}, l_{\text{ML}}) = \arg \min_{q,l} \|\hat{\mathbf{Y}}(i) - s_l(\hat{\mathbf{H}}(i)\boldsymbol{\zeta})_q\|^2. \quad (7.4)$$

Eq. (7.4) vectorizes (7.2) such that  $\hat{\mathbf{Y}}(i) = \text{vec}(\mathbf{Y}(i)) \in \mathbb{R}^{NT \times 1}$ ,  $\hat{\mathbf{H}}(i) = \mathbf{I} \otimes \mathbf{H}(i) \in \mathbb{R}^{NT \times PT}$  and  $\boldsymbol{\zeta}_q = [\text{vec}(\mathbf{D}_1) \dots \text{vec}(\mathbf{D}_Q)] \in \mathbb{R}^{PT \times Q}$ .

### 7.2.1 Permutation-Aided STSK Scheme

Spatial modulation (SM) and space shift keying (SSK) are combined into STSK in order to activate a signal emission pattern in space and time. The proposed STSK modulation scheme in [24, 25] selects from a set of  $Q$  dispersion matrices  $\mathbf{D}_q (q = 1, 2, \dots, Q)$  at every block period with a power constraint defined by the trace operation  $\text{tr}[\cdot]$

$$\text{tr}[\mathbf{D}_q^H \mathbf{D}_q] = T \quad (q = 1, 2, \dots, Q), \quad (7.5)$$

and  $\mathbf{D}_q^H$  represents the transpose of  $\mathbf{D}_q$ . The emission pattern is produced using a permutation matrix  $\mathbf{D}_q$  obtained from a permutation codeword. For each column in  $\mathbf{D}_q$ , each integer in the codeword  $\mathbf{b} = [b_1, b_2, \dots, b_T]$  indicates the position with the non-zero element at each row. Therefore, every  $\log_2(Q \cdot M)$  bits from the source's incoming bits in Fig. 7.3 are mapped to a dispersion matrix  $\mathbf{D}_q$

and a constellation point  $s(i)$ . Different possible combinations of  $D(i)$  and  $s(i)$  are shown in Table 7.1. A codebook  $C$  with minimum Hamming distance  $d_{\min}$  is selected from a set of  $T!$  permutation of integers in  $\mathbf{b}$  such that each codeword is of length  $T$ . Therefore, a maximum of  $2^{\lfloor \log_2 T \rfloor}$  unique codewords can be combined with an  $M$ -PAM modulation order where  $\lfloor \cdot \rfloor$  describes the floor function. Each codeword is mapped to one of  $M$  unipolar PAM symbols whose amplitudes have discrete values

$$s(i) = A_m, m = 0, 1, \dots, M - 1. \quad (7.6)$$

TABLE 7.1: Mapping of message bits to PSTSK and Modulation Scheme

Input Bits	$Q = 8, M = 1$			$Q = 4, M = 2$		
	Codeword	$D(i)$	$s(i)$	Codeword	$D(i)$	$s(i)$
000	1234	$D_1$	1	1234	$D_1$	$A_0$
001	1342	$D_2$	1	1234	$D_1$	$A_1$
010	1423	$D_3$	1	1342	$D_2$	$A_0$
011	3214	$D_4$	1	1342	$D_2$	$A_1$
100	4132	$D_5$	1	1423	$D_3$	$A_0$
101	2314	$D_6$	1	1423	$D_3$	$A_1$
110	2431	$D_7$	1	3241	$D_4$	$A_0$
111	2143	$D_8$	1	3241	$D_4$	$A_1$

The Euclidean distance between the Gray-coded constellation points of the PAM symbols is defined as [40]

$$g_{\min,E} = \sqrt{\frac{6E_{b(\text{ELEC})}\log_2 M}{(M-1)(2M-1)}}, \quad (7.7)$$

where  $E_{b(\text{ELEC})}$  is the average electrical energy per bit. As an example, permutation codeword (2, 1, 3) will insert a 1 in the permutation matrix

$$D_q = \begin{bmatrix} 0 & d_{12} & 0 \\ d_{21} & 0 & 0 \\ 0 & 0 & d_{33} \end{bmatrix}.$$

If each non-zero element  $d_{nt} = 1$ , then the non-zero element indicates the activated LED index at each time slot. Therefore, the resulting permutation matrix  $S(i)$  represents a space-time code which transmits a PAM symbol over each activated LED index such that

$$\sum_{t=1}^T d_{nt} = s(i), \quad \sum_{n=1}^N d_{nt} = s(i). \quad (7.8)$$

The number of bits per symbol transmitted at each sampling period is given as

$$R = \frac{\log_2(Q \cdot M)}{T}. \quad (7.9)$$

Unlike SM which increases AEs in order to increase the data rate, the data rate of this scheme does not necessarily increase as the number of AEs increase. Rather, multiple combinations of the mapping between the constellation points and permutation matrices can be used to increase the data rate as shown in Table 7.1. If the mapping between the constellation point and the permutation matrix is not one-to-one, then the ML equation in (7.4) is used to determine the constellation point of the signal mapped to the codeword, hence the dotted lines in Fig. 7.3.

### 7.3 Proposed Optimization Algorithms as Soft-Detection Receiver

Consider each received intensity value  $y_{nt} \in \mathbf{Y}(i)$ , if the CSI is unknown, then a cost matrix  $\hat{\mathbf{Y}}(i)$  is derived such that  $\hat{y}_{nt} = -y_{nt}$ . This creates an assignment problem such that

$$\hat{\mathbf{Y}}(i) = \begin{array}{cccc} \text{job 1} & \text{job 2} & \dots & \text{job } N \\ \begin{bmatrix} \hat{y}_{11} & \hat{y}_{12} & \dots & \hat{y}_{1N} \\ \hat{y}_{21} & \hat{y}_{22} & \dots & \hat{y}_{2N} \\ \vdots & \vdots & \ddots & \vdots \\ \hat{y}_{T1} & \hat{y}_{T2} & \dots & \hat{y}_{TN} \end{bmatrix} & \text{worker 1} \\ & \text{worker 2} \\ & \vdots \\ & \text{worker } T \end{array}, \quad (7.10)$$

where the rows in  $\hat{\mathbf{Y}}(i)$  represent the workers while the columns represent the jobs and a one-to-one mapping of workers to jobs is assumed. Assuming a perfect knowledge of the CSI, then  $\hat{\mathbf{Y}}(i) = -\mathbf{H}(i)\mathbf{Y}(i)$ . Since  $\hat{\mathbf{Y}}(i)$  is a permutation matrix with noise and attenuation, then the likely transmitted permutation matrix can be detected by using optimization algorithms [27]. Each element  $\hat{y}_{nt} \in \hat{\mathbf{Y}}(i)$  represents the cost required by worker  $n$  to carry out job  $t$ . Therefore, the SD receiver finds the solution to the assignment problem

$$Z_1 = \sum_{t=1}^T \sum_{n=1}^N \hat{y}_{nt} d_{nt}, \quad (7.11)$$

that produces the permutation matrix  $\mathbf{D}_q = [d_{nt}] \in \{0, 1\}$ . The Hungarian algorithm [73] forms the first iteration  $e = 1$  of the receiver and provides an optimal solution to (7.11) with  $O(N^3)$  worst case complexity. The solution produces a corresponding row-column pair  $\{(1, b_1), (2, b_2), \dots, (T, b_T)\}$  and the permutation of  $b_1, b_2, \dots, b_T$  is the received codeword  $\mathbf{a}_1$ , hence the received permutation matrix.

If  $\mathbf{a}_1 \notin C$ , then Murty's solution [27,74] carries out further iterations  $e_2, e_3, \dots, e_Q$  by ranking the costs of  $\hat{\mathbf{Y}}(i)$  from  $Z_2, Z_3, \dots, Z_Q$  with worst case complexity of  $O(N^4)$  [78]. The solution to  $Z_1$  produces a solution matrix from which  $n-1$  subsets of  $\mathbf{Y}(i)$  are created as nodes  $U_1, U_2, \dots, U_{n-1}$ . The nodes are created by partitioning  $\mathbf{a}_1$  such that

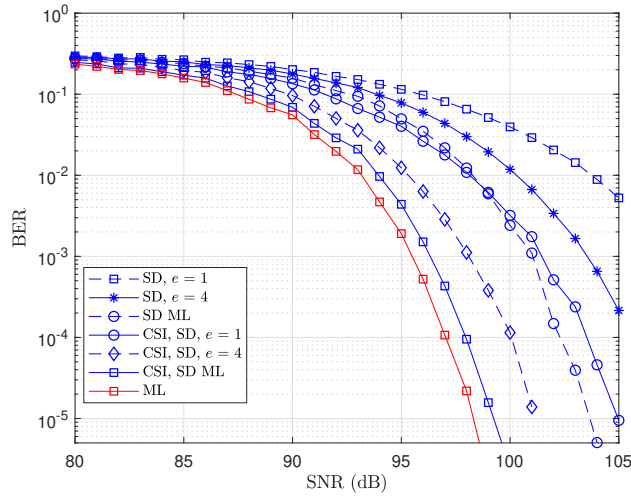
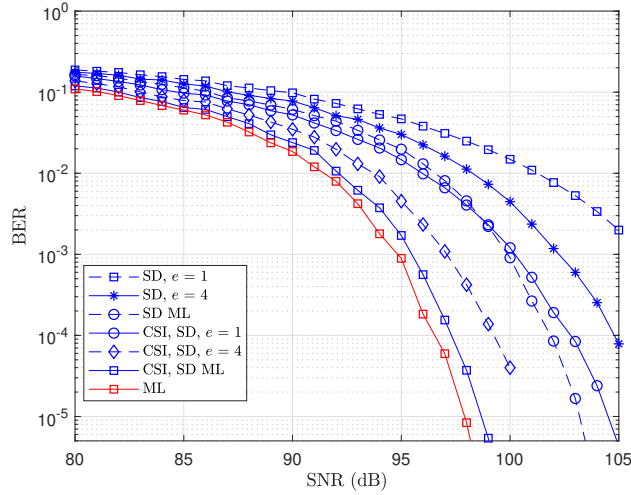
$$\begin{aligned} U_1 &= \overline{\{(1, j_1)\}}, \\ &\vdots \end{aligned} \quad (7.12)$$

$$U_{n-1} = \overline{\{(1, j_1), \dots, (n-1, j_{n-1})\}}.$$

The items with a bar ( $\overline{\cdot}$ ) in  $U_1, U_2, \dots, U_{n-1}$  are replaced with  $\infty$  while the other items are excluded. By solving for the minimum cost of each derived node, the next assignment is then derived from the node with the lowest cost. This process can be iterated from  $Z_2, Z_3, \dots, Z_Q$  until  $\mathbf{a}_e \in C$ . The soft detection's ML uses a brute force approach to find the codeword  $\mathbf{c}_q$  that produces the matrix  $\mathbf{D}_q$ , having the lowest cost

$$Z_{\text{ML}} = \arg \min_{q \in Q} \left( \sum_{n=1}^N \sum_{t=1}^T \hat{y}_{nt} d_{nt}^{(q)} \right), \quad \text{for } q = 1, 2, \dots, Q, \quad (7.13)$$

where  $d_{nt}^{(q)}$  is each element in the matrix  $\mathbf{D}_q$ .


 FIGURE 7.4: BER performance of PSTSK(4, 4, 4, 2) using codebook with  $d_{\min} = 4$  selected from  $|T| = 24$ .

 FIGURE 7.5: BER performance of PSTSK(4, 4, 4, 4) using codebook with  $d_{\min} = 4$  selected from  $|T| = 24$ .

## 7.4 Simulation Results

An indoor setup in Fig. 7.1 is assumed in the simulations and the notation PSTSK( $P, N, Q, M$ ) henceforth describes the permutation-aided scheme. The channel coefficients in (7.1), similar to [109] are generated by placing the receiver unit on the table top, 1.75 m vertical distance from the transmitter unit. The LEDs are represented as the polygon shapes inside the transmitter unit while the PDs are represented as the ellipse shapes inside the receiver unit. The transmitters are spaced 0.2 m apart while the receivers are spaced 0.1 m apart with  $A_{\text{pd}} = 1 \text{ cm}^2$ . The transmitters and receivers are symmetrically arranged for all setups and assumed to be perfectly synchronized. The semi-angle of the transmitter  $\Phi_c = 15^\circ$  and receiver  $\Psi_c = 15^\circ$  and are chosen as recommended according to [111, 112]. Monte Carlo simulations are carried out to compare the closeness of different iterations  $e$  of the SD detector's BER performance to the scheme's ML performance. The ML performance of the SD detector described in (7.13) is also shown to demonstrate the maximum achievable gain of the SD.

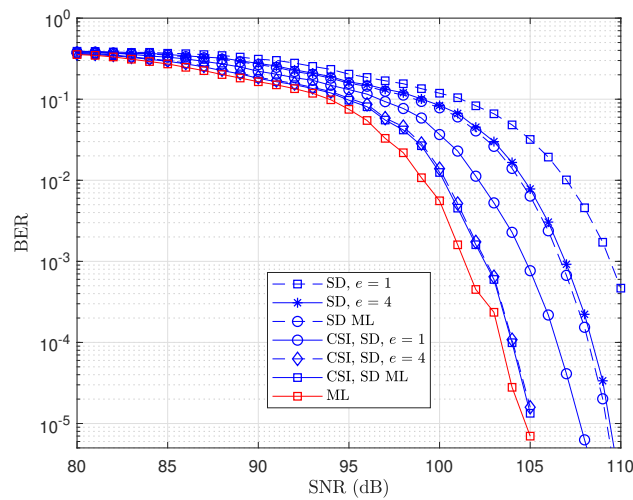


FIGURE 7.6: PSTSK(6, 6, 256, 4) when  $\frac{Q}{|T|} = 0.3556$ . Codebook's  $d_{\min} = 3$  and  $Q = 256$ , selected from  $|T| = 720$ .

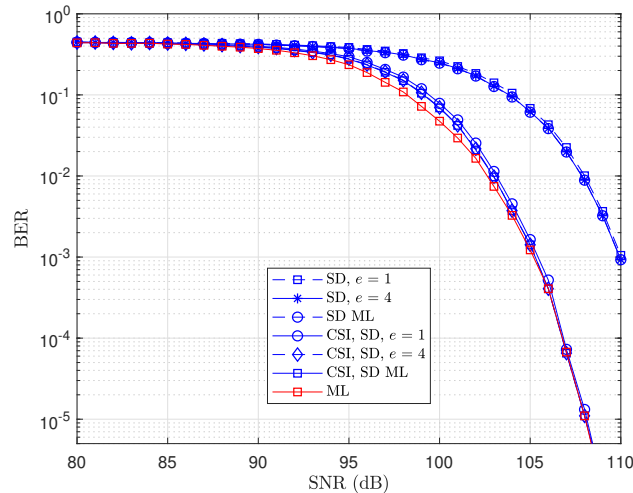
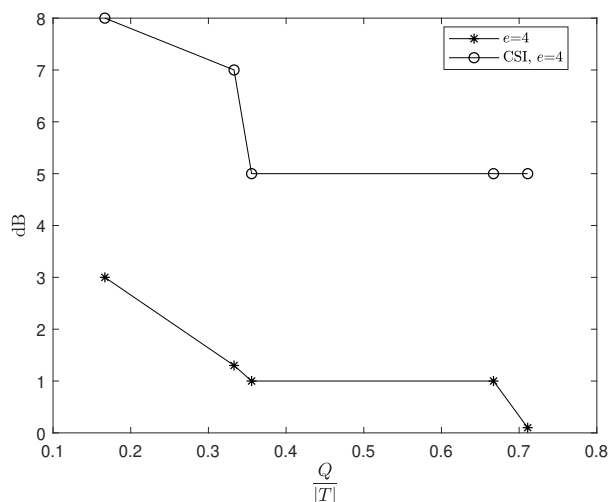
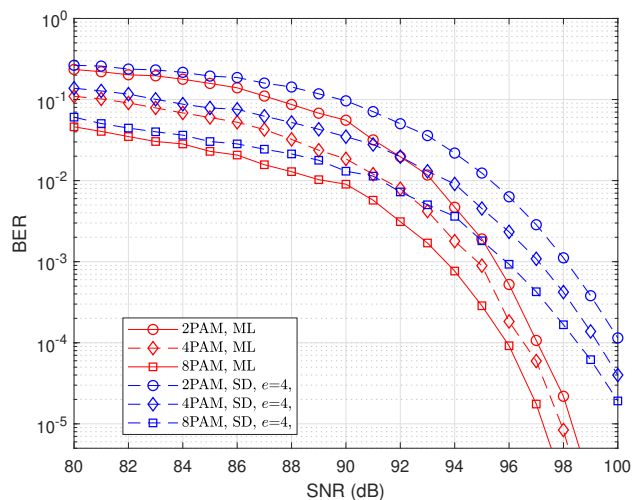


FIGURE 7.7: PSTSK(6, 6, 512, 2) when  $\frac{Q}{|T|} = 0.7111$ . Codebook's  $d_{\min} = 2$  and  $Q = 512$ , selected from  $|T| = 720$ .

#### 7.4.1 BER Performance and $\frac{Q}{|T|}$ Ratio

The ratio of  $\frac{Q}{|T|}$  describes the ratio between the number of codewords in the selected codebook  $Q$  and the number of all possible codewords  $|T|$ . Hence, the ratio represents the probability of detecting a codeword in the codebook and the BER performance of the SD with respect to the ML increases as  $\frac{Q}{|T|}$  increases. For example, in Figs. 7.4 and 7.5, a ratio  $\frac{Q}{|T|} = 0.1667$ , in which  $Q = 4$  codewords are selected from  $|T| = 24$  possible codewords produces a 3 dB difference to the ML at iteration  $e = 4$  and perfect CSI knowledge. Without the knowledge of the CSI, a 5 dB penalty is observed. However, Figs. 7.6 and 7.7 show the SD performs close to the ML with ratios  $\frac{Q}{|T|} = 0.3556$  and  $\frac{Q}{|T|} = 0.7111$  respectively. Therefore, as shown in Fig. 7.8, the SD performs closer to ML as  $\frac{Q}{|T|}$  increases in the presence of the CSI and a flat 5 dB loss is obtained in the absence of the CSI.

FIGURE 7.8: dB gain between the ML and SD at  $e = 4$  at different ratios of  $\frac{Q}{|T|}$ .FIGURE 7.9: BER vs SNR comparing the performance of the SD's 4th iteration with ML detection of a PSTSK(4, 4, 4,  $M$ ) setup with  $d_{\min} = 4$ .

## 7.4.2 Effect of Minimum Distance and Modulation Order $M$

Minimum distance  $d_{\min}$  of the codebook generally increases the BER performance of the coded system. This also applies in the permutation-aided MIMO system and the obtainable  $d_{\min}$  decreases as  $\frac{Q}{|T|}$  increases. The SD receiver performs closer to ML at a higher  $\frac{Q}{|T|}$  ratio as summarized in Fig. 7.8. Therefore, the SD receiver is suggested in scenarios where higher data rates are required and codebooks with smaller  $d_{\min}$  are naturally chosen to match the data rate. The size of  $M$  improves the BER performance as  $M$  increases. As shown in Fig. 7.9, the SD detector at lower SNRs produces better BER performance compared to the ML detection of  $M = 2$ . This suggests that increasing  $M$  not only increases the data rate but can be used to improve the BER performance at a reduced computational complexity.

## 7.5 Conclusion

An iterative SD receiver of a permutation-aided STSK in an indoor VLC system is designed by interpreting the channel output as an assignment problem. The BER performance of the ML detection of the scheme is compared with the iterative SD receiver in the presence of the CSI and absence of the CSI. The SD receiver with the CSI matches the BER performance of the ML receiver in some setups but a 5 dB loss is obtained in the absence of the CSI. The SD receiver also reduces the complexity presented by the ML detection.

# Low-complexity Detection of Multiweight Permutation Modulation Space-Time Block Codes for Indoor Visible Light Communication

---

**This chapter is based on the following publication:** *O. Kolade, and L. Cheng, "Low-complexity Detection of Multiweight Permutation Modulation Space-Time Block Codes for Indoor Visible Light Communication". Under review with Elsevier Optics Communications.*

The author of this thesis conceptualized the work, performed the simulations, analyzed the results and wrote the paper.

---

## 8.1 Introduction

The concept of using existing illumination for visible light communication (VLC) is becoming attractive for low cost communication with potential to deliver information to the last mile. Since lighting infrastructures usually consist of multiple light emitting diodes (LEDs), a natural multiple-input multiple-output (MIMO) setup is established. MIMO schemes provide several advantages such as higher data rates, spatial diversity and improvement of the error rate performance using the receiver diversity. For example, a space-time block code (STBC) [113] provides transmit diversity such as the Alamouti STBC [114]. The single receiver's maximum likelihood (ML) detection method requires the channel state information (CSI) but with reduced detection complexity.

In MIMO VLC [2, 49, 109], activating a unique combination of LEDs from the total available LEDs can be used for information signaling. The index of the activated LED(s) can also convey additional information in order to increase the data rate. Repetition coding (RC) is an example whose receiver adds up light intensities from the LEDs which are transmitting the same information over the multiple transmitters at each transmit time. Index modulation (IM) assists with improving the data rate of MIMO-VLC systems by mapping information to activated LEDs. In scenarios where inter-channel interference (ICI) is required to be eliminated, spatial modulation (SM) [49], a type of IM maps  $\log_2 M$  bits to an activated index. The activated index can also convey additional information selected from a conventional  $M$ -ary modulation scheme such as pulse amplitude modulation (PAM) or on-off keying (OOK) [115]. Another IM scheme is space shift keying (SSK) [101] which activates one LED index at each transmit time in order to eliminate ICI with a receiver complexity similar to a single-input single-output (SISO) receiver complexity. Space-time shift keying (STSK) proposed in [24] extends the concept of SSK to take advantage of the time diversity by activating one of the  $Q$  dispersion matrices

which have been prior mapped to the information bits. However, when MIMO detection schemes require the CSI, they become prone to channel estimation errors and impractical when the CSI is unknown. Differential spatial modulation (DSM) [106, 107, 116, 117] uses a permutation matrix to determine the antenna index to be activated and can also mitigate ICI between the transmitters since one transmitter is active within a transmit period. Also, the incoming information bits are differentially modulated, as a result the receiver is able to detect the transmitted signals without knowledge of the CSI.

Permutation modulation (PM) [41] is one of several methods of generating the space-time codes used for antenna transmit matrices [24, 29, 106, 118, 119] and is preferred mainly because of its ability to mitigate the effect of ICI. In [106], information bits are mapped onto PM-aided matrices which are then differentially modulated. In [24], the PM-aided matrices are used to design antenna dispersion matrices. The main drawback of PM-aided MIMO schemes is the reduced spectral efficiency when compared with conventional MIMO schemes such as RC, SM and generalized spatial modulation techniques [103, 109]. Moreover, decoding PM-aided matrices becomes too complex as the number of antennas increase. A low-complexity decoder in [27] (chapter 4) combines optimization algorithms in [73] and [74] to decode permutation block codes, while a similar concept in [29] (chapter 7) decodes PM-aided transmit matrices at the receiver with and without the knowledge of the CSI at the receiver. While the dispersion matrices are designed for radio frequency (RF) systems which can transmit either real or complex-valued signals, a PM STSK scheme suitable for VLC adopts the STSK scheme in [105]. Similar to DSM, this scheme also activates a permutation matrix in which the non-zero elements in the matrix determine the LED index to be activated at each symbol period.

Optimization algorithms in [73] and [74] have been combined in order to decode the received matrix with and without the knowledge of the CSI at the receiver. In an indoor environment where the receiver is mobile [120], it is of interest to have low-complexity detection algorithms that can operate without the knowledge of the CSI and within practical complexity limits. On the other hand, permutation coded schemes are generally low rate codes with a scarce amount of low-complexity, soft-decision receivers. In order to increase the information rate of permutation-coded systems, concatenated permutation block codes [121] have been used while simultaneously increasing the code's minimum distance. However, the concatenated permutations presented in [121] do not construct equal weight matrices which is required for the MIMO scheme presented in this chapter. On the other hand, soft-decision detection of permutation matrices with weight greater than 1 do not exist to the best of our knowledge.

In this chapter, a novel higher rate PM-aided MIMO VLC scheme is presented at the transmitter and low-complexity detection schemes at the receiver. The first contribution of this chapter introduces a class of concatenated permutation codes which generate equal weight space-time codes in order to increase the number of bits conveyed by the transmit matrix of the PM-aided MIMO VLC scheme. The second contribution designs low-complexity, iterative, soft-decision (SD) detection methods using optimization algorithms. The SD methods are capable of decoding the likely transmitted bits without knowledge of the channel matrix. The bit error rate (BER) expression for the ML decoder is also derived with the SD decoders matching the ML performance for certain setups.

The following notations are used in this chapter.  $\text{tr}[\cdot]$  is the trace operation,  $\|\cdot\|_F$  is the Frobenius norm,  $(\cdot)^H$  is the conjugate transpose operation and the Q-function is defined as  $Q(r) = \frac{1}{2\pi} \int_r^{+\infty} \exp\left(-\frac{x^2}{2}\right) dx$ .

## 8.2 System Model for Permutation-Aided MIMO For VLC

### 8.2.1 Permutation-Aided STSK Scheme

Consider a permutation codebook  $\mathcal{C}$  with  $Q$  codewords. Each codeword  $\mathbf{c}_q$  at row  $q$  ( $q = 1, 2, \dots, Q$ ) is a row vector consisting of a unique permutation of integers  $(c_1, c_2, \dots, c_L)$ . Hence, each symbol in

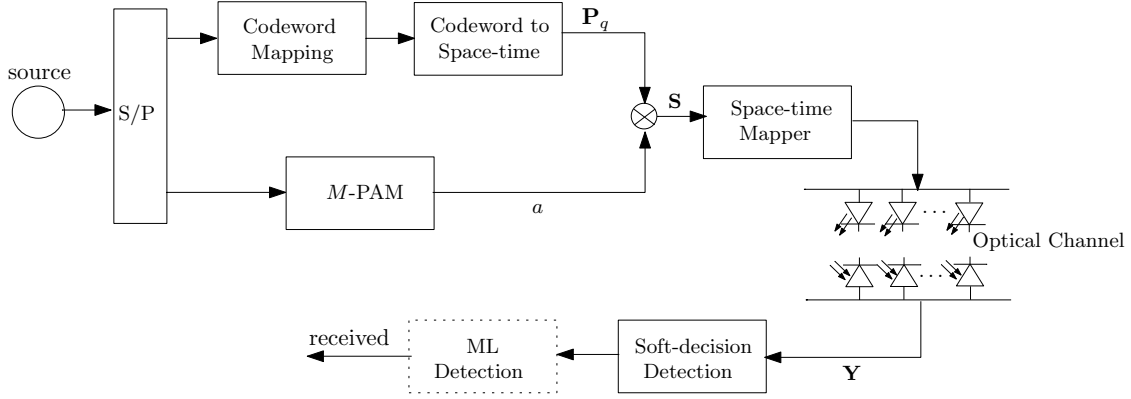


FIGURE 8.1: System model for permutation-aided STSK with soft-detection.

a codeword creates a corresponding column vector

$$\underbrace{(0, \dots, 0, 1, 0, \dots, 0)}_{l-1}^T,$$

for  $l = 1, 2, \dots, L$  and a permutation of  $L$  symbols in a codeword produces a codeword matrix  $\mathbf{P}_q$ . Each matrix  $\mathbf{P}_q$  is equivalent to the codeword at row  $q$  and the index of the non-zero element in each row of  $\mathbf{P}_q$  corresponds to each integer in  $c_q$ .

We define the weight  $w$  of the matrix as the number of non-zero elements in its rows and columns. Hence, a  $\{0, 1\}^{L \times L}$  permutation matrix  $\mathbf{P}_q$ , having columns and rows with weight  $w = 1$  is transmitted within a block of multiple time slots. Considering the model in Fig. 8.1, the incoming bits are split into two groups in the serial-to-parallel (S/P) converter. The first group is mapped onto  $\mathbf{P}_q$  and the second group is mapped onto an  $M$ -PAM intensity level to create a transmit matrix. The permutation matrix  $\mathbf{P}_q$  enables an activation pattern per transmit block, with each non-zero element representing the activated LED index. As a result, each transmit block conveys  $\log_2 Q$  bits from the incoming message bits. The power constraint of the transmitted block is given as  $\text{tr}[\mathbf{P}_q^H \mathbf{P}_q]$ . Additional  $\log_2 M$  information bits, mapped onto a unipolar  $M$ -ary modulation scheme such as pulse amplitude modulation (PAM) can be transmitted over the active LED in order to increase the information rate. This also ensures the transmitted signal is positive and real and a total of  $\log_2(Q \cdot M)$  bits can be transmitted at each transmit block. The resulting transmitted matrix  $\mathbf{S} = [s_{ij}]$

$$\mathbf{S} = a \cdot \mathbf{P}_q, \quad (8.1)$$

represents a space-time code where  $a$  takes any of the  $M$  intensities

$$I_m = \frac{2I}{w(M+1)} m \quad \text{for } m = 1, 2, \dots, M, \quad (8.2)$$

where  $I$  is the mean optical transmit power. The  $M$ -PAM symbol is transmitted over each activated LED index such that

$$\sum_{i=1}^L s_{ij} = \sum_{j=1}^L s_{ij} = a. \quad (8.3)$$

As a result, the number of bits per symbol transmitted at each sampling period is given as  $\frac{\log_2(Q \cdot M)}{L}$ .

## 8.2.2 MIMO VLC Channel Model

A line-of-sight (LOS) channel model between  $L$  LEDs as transmitters and  $L$  photodiodes (PD) as receivers is assumed. The transmitters employ intensity modulation while direct detection is employed

at each receiver. Assuming Lambertian LEDs and PDs, the channel gain between an LED and a PD is given as [55]

$$h = \begin{cases} \frac{(e+1)A_{\text{pd}}}{2\pi f^2} \cos^e(\phi) \cos(\psi), & \text{for } 0 \leq \psi \leq \Psi \\ 0, & \psi > \Psi, \end{cases} \quad (8.4)$$

where  $A_{\text{pd}}$  is the PD's surface area,  $f$  is the distance between the LED and the PD,  $\phi$  and  $\psi$  describe the transmitter's and receiver's angle of incidence respectively. For a semi-angle  $\Phi_{\frac{1}{2}}$ , the Lambertian emission order  $e = \frac{-\ln 2}{\ln(\cos \Phi_{\frac{1}{2}})}$ , while  $\Psi$  is the field of view of the receiver. The received matrix at the photodiodes is modelled as

$$\mathbf{Y} = \mathbf{H}\mathbf{S} + \mathbf{N}, \quad (8.5)$$

where  $\mathbf{Y} \in \mathbb{R}^{L \times L}$  is the matrix received at each block, each element in  $\mathbf{H} \in \mathbb{R}^{L \times L}$  is given by the expression in (8.4),  $\mathbf{S} \in \mathbb{R}^{L \times L}$  is the transmitted PM signal matrix and  $\mathbf{N} \in \mathbb{R}^{L \times L}$  consists of real-valued additive white Gaussian noise (AWGN) samples with  $\mathcal{CN}(0, \frac{N_0}{2})$  values in order to model shot and thermal noise at the receiver.

The ML detector selects the codeword matrix that satisfies

$$\hat{\mathbf{S}} = \arg \min_{\mathbf{S}} \|\mathbf{Y} - \mathbf{H}\mathbf{S}\|^2, \quad (8.6)$$

which implies the codeword matrix which has the closest Euclidean distance with the received codeword matrix.

### 8.2.3 Concatenated Permutations for STSK

In order to increase the data rate of the PM MIMO scheme, multiple permutation codewords are combined to activate more than one LED at each transmit time. First, we denote  $\mathbf{c}_q^{\bar{w}}$  as the codeword in codebook  $\bar{w}$  ( $1 \leq \bar{w} \leq w$ ) at row  $q$  and  $\mathbf{P}_q^{\bar{w}}$  is the equivalent permutation matrix. The concatenated codewords ( $\mathbf{c}_q^1 \mathbf{c}_q^2 \cdots \mathbf{c}_q^w$ ) are chosen such that the Hamming distance between any two codewords at row  $q$  of the codebooks

$$d_m(\mathbf{c}_q^1, \mathbf{c}_q^2) = L. \quad (8.7)$$

This means any  $w$  concatenated codewords differ in as many places as the length of a codeword. The number of codewords with Hamming distance  $L$  from a given codeword  $\mathbf{c}_q^{\bar{w}} \in \mathbf{C}_w$  is [122]

$$|K| = L! \cdot \sum_{k=0}^L \frac{(-1)^k}{k!}, \quad (8.8)$$

and the codewords can be concatenated in order to produce unique codeword transmit matrices. Each matrix has a weight  $w$  on the columns and rows, same as the number of concatenated codewords. The transmitted matrix of the concatenated codewords is given as

$$\mathbf{P}_q = \mathbf{P}_q^1 + \mathbf{P}_q^2 + \cdots + \mathbf{P}_q^w. \quad (8.9)$$

In the combined codebook  $\mathbf{P}_q$ , any two codewords ( $\mathbf{P}_q^1, \mathbf{P}_q^2$ ) are the same if  $\mathbf{P}_q^1 - \mathbf{P}_q^2 = 0$ , even if produced by different combined codewords. Hence, only one of the codewords is chosen to avoid duplicate entries.

A simple construction of codewords which satisfy (8.7) is achieved by selecting from  $L$ -order Latin squares [123], each consisting of an  $L \times L$  integer matrix, derived from a set of  $L$  codewords. In each matrix, an integer occurs only once in each row and column and each row and column is a permutation. The permutations that form the Latin square can be constructed for example, by performing a cyclic shift on a codeword. For example, in codebook  $\mathbf{C}_1$ , a cyclic shift on a codeword  $\mathbf{c}_1^1 = (c_1^1 c_2^1 \cdots c_L^1)$

TABLE 8.1: Mapping between modulation scheme and codes with  $w = 1$  and  $w = 2$ .

Input Bits	$Q = 32, M = 1$		$Q = 32, M = 2$	
	Codewords	$m$	Codewords	$m$
0000	1234	1	1234	1
0001	1243	1	1234	2
0010	1243	1	1234	1
0011	1243	1	1234	2
$\vdots$	$\vdots$	$\vdots$	$\vdots$	$\vdots$
11100	1234, 2143	1	1234, 2143	1
11101	1324, 2413	1	1324, 2413	2
11110	3241, 4132	1	3241, 4132	1
11111	3124, 4312	1	3124, 4312	2

produces  $\mathbf{c}_2^1 = (c_2^1 c_3^1 \dots c_L^1 c_1^1)$ . Assuming  $\mathbf{c}_1^1$  is (2314) and is cyclically shifted to (3142),  $\mathbf{c}_1^1$  and  $\mathbf{c}_2^1$  satisfy (8.7) and the concatenated codewords produce a matrix

$$\mathbf{P}_q = \begin{bmatrix} 0 & 1 & 1 & 0 \\ 1 & 0 & 0 & 1 \\ 1 & 1 & 0 & 0 \\ 0 & 0 & 1 & 1 \end{bmatrix},$$

with  $w = 2$ . This enables  $w$  unique LED combinations in each time slot in a block using codewords which belong to one of  $w$  codebooks  $\{\mathbf{C}_1, \mathbf{C}_2, \dots, \mathbf{C}_w\}$  for  $1 < w < L$ . The message symbols are then mapped onto  $w$ -tuple codewords  $(c_q^1 c_q^2 \dots c_q^w)$  which belong to the same row  $q$  in  $\mathbf{C}_1, \mathbf{C}_2, \dots, \mathbf{C}_w$  respectively.

The concatenated codewords can be added to the conventional  $w = 1$  codewords in order to increase the number of codewords. Hence, the total number of codewords achievable is

$$Q = Q_1 + Q_2 + \dots + Q_{L-1}, \quad (8.10)$$

where  $Q_w$  is the number of codewords available for a given weight  $w$ . An example is shown in Table 8.1 where the bits per symbol is increased to  $2^{(L+1)}$  without increasing the size of  $L$ . The increase in the number of active indices also enables higher order constellation points to be modulated on top of the active LED index, hence increasing the data rate when compared to the  $w = 1$  permutation-aided scheme. Using (8.1), the transmitted matrix is given as

$$\sum_{i=1}^M s_{ij} = \sum_{j=1}^M s_{ij} = w \cdot a. \quad (8.11)$$

Given equiprobable symbols with unique one-to-one mapping onto codewords, the pairwise error probability of receiving a codeword signal  $\hat{\mathbf{S}}$  when  $\mathbf{S}$  is transmitted is given as [38]

$$Pr(\hat{\mathbf{S}} \rightarrow \mathbf{S} | \mathbf{H}) \leq Q \left( \sqrt{\frac{E_{\text{rx}}}{2N_0} \|\mathbf{H}(\mathbf{S} - \hat{\mathbf{S}})\|_F^2} \right). \quad (8.12)$$

Within a transmit block, the electrical SNR which is the ratio between the received electrical energy ( $E_{\text{rx}}$ ) and the noise power is  $\frac{E_{\text{rx}}}{N_0} = \frac{(rI)^2}{N_0} T_s$  for sampling time  $T_s$  and an optical-to-electrical conversion coefficient  $r$ . By using the union bound method, the upper bound of the BER is derived in (8.13) adopting the methods from [109]. This is done by comparing all possible  $M \cdot Q$  codeword matrices

$$\text{BER} \leq \frac{1}{M \cdot Q \log_2(M \cdot Q)} \sum_{m_1=1}^M \sum_{q_1=1}^Q \sum_{m_2=1}^M \sum_{q_2=1}^Q d_m(b_{m_1}^{(q_1)}, b_{m_2}^{(q_2)}) Q \left( \sqrt{\frac{E_{\text{rx}}}{2N_0} \|\mathbf{H}(I_{m_1} \mathbf{S}^{(q_1)} - I_{m_2} \mathbf{S}^{(q_2)})\|_F^2} \right). \quad (8.13)$$

and intensity combinations. The term  $d_m(b_{m_1}^{(q_1)}, b_{m_2}^{(q_2)})$  denotes the Hamming distance between the received bits  $b_{m_2}^{(q_2)}$  when actually,  $b_{m_1}^{(q_1)}$  was transmitted.

### 8.3 Proposed Optimization Algorithms for Soft-Decision Detection

From the received matrix  $\mathbf{Y} = [y_{ij}]$  at each block, the detector processes  $\hat{\mathbf{Y}} = [\hat{y}_{ij}]$  such that  $\hat{y}_{ij} = -y_{ij}$ . For  $w = 1$ , the decoder finds the corresponding codeword  $\hat{c}$  at row  $q$  that produces the cost

$$g_1 = \sum_{i=1}^L \sum_{j=1}^L \hat{y}_{ij} s_{ij}, \quad (8.14)$$

that minimizes (8.14). For  $1 < w < L$ , the decoder finds the set of  $w$ -tuple codewords  $\{\hat{c}_q^1, \hat{c}_q^2, \dots, \hat{c}_q^w\}$  which belong to the same row  $q$  in  $\{C_1, C_2, \dots, C_w\}$  that produce the cost

$$g_1 = \arg \min_{c_q \in C} \left( \sum_{i=1}^L \sum_{j=1}^L \hat{y}_{ij} s_{ij}^{(c_q^1)} + \sum_{i=1}^L \sum_{j=1}^L \hat{y}_{ij} s_{ij}^{(c_q^2)} + \dots + \sum_{i=1}^L \sum_{j=1}^L \hat{y}_{ij} s_{ij}^{(c_q^w)} \right), \text{ for } q = 1, 2, \dots, Q, \quad (8.15)$$

that minimizes (8.15). Here,  $s_{ij}^{(c_q^w)}$  values are the elements in  $S$ , produced by a codeword at row  $q$ . Each codeword  $c_q^1, c_q^2, \dots, c_q^w$  belongs to codebooks  $C_1, C_2, \dots, C_w$  respectively.

#### 8.3.1 Brute Force Soft-Decision Receiver

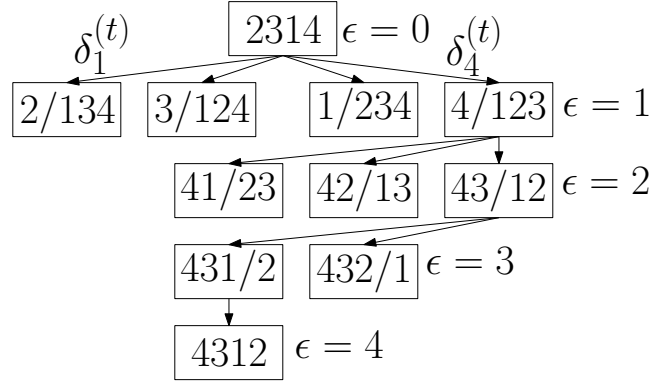
The brute force (BF) of the soft-decision decoders solves

$$g_{\text{BF}} = \arg \min_{c_q \in C} \left( \sum_{i=1}^L \sum_{j=1}^L \hat{y}_{ij} s_{ij}^{(c_q)} \right), \text{ for } q = 1, 2, \dots, Q, \quad (8.16)$$

where  $s_{ij}^{(c_q)}$  is each element in the permutation matrix produced by a codeword  $c$ . The BF SD receiver ranks the costs  $g_1, g_2, \dots, g_Q$  and chooses the lowest cost  $g_{\text{BF}}$  that produces the permutation matrix  $P_{\text{BF}}$  and whose corresponding codeword  $\hat{c}_{\text{BF}} \in C$ .

#### 8.3.2 Branch and Bound

The branch and bound (BB) algorithm [96] can be used to solve a  $w = 1$  received matrix in (8.14) using the tree-based method in Fig. 8.2.  $L + 1$  levels defined as  $\epsilon = 0, 1, \dots, L$  are created. Each node has an associated cost  $\delta_\epsilon^{(t)} = \delta_\epsilon^{(1)}, \delta_\epsilon^{(2)}, \dots, \delta_\epsilon^{(L-\epsilon+1)}$ . The initial node at  $\epsilon = 0$  is any of the codewords used at


 FIGURE 8.2: Tree-based method to decode permutation codes using branch and bound with  $L = 4$ .

the encoder. The surviving node at  $\epsilon = 1$  is determined by finding the node that satisfies

$$\hat{\delta}_\epsilon^{(t)} = \min_{1 \leq t \leq L} \left( \hat{y}_{\epsilon t} + \sum_{i,j} \hat{y}_{ij} \right), \quad (8.17)$$

for  $\epsilon = 1, 2 \leq i \leq L, 0 < j \leq L : j \neq t$ . The surviving node  $\hat{t}_\epsilon$  which satisfies (8.17) is used to create  $L - \epsilon$  branches for levels  $\epsilon = 2$ . The surviving node at each levels  $\epsilon > 1$  is evaluated as

$$\hat{\delta}_\epsilon^{(t)} = \min_{1 \leq t \leq L} \left( \hat{y}_{(\epsilon-1)\hat{t}_{(\epsilon-1)}} + \hat{y}_{\epsilon t} + \sum_{i,j} \hat{y}_{ij} \right), \quad (8.18)$$

for  $\epsilon > 1, \epsilon + 1 \leq i \leq L, 1 \leq j \leq L : j \neq t, j \notin \hat{\mathbf{t}}$ . Note that  $\hat{\mathbf{t}}$  is a vector containing the surviving nodes and (8.18) is repeated until the  $L - 1$ -th node to solve the permutation codeword.

### 8.3.3 Iterative Soft-Decision Detection

The iterative decoder finds the maximum cost of  $\hat{\mathbf{Y}}$  that produces a codeword  $\hat{c}_q^n$  in each codebook  $\{\mathbf{C}_1, \mathbf{C}_2, \dots, \mathbf{C}_w\}$  at each iteration  $e$ . Assuming  $\hat{c}_1^1$  is the decoded codeword for  $\mathbf{C}_1$  and  $\hat{c}_2^2$  is decoded for  $\mathbf{C}_2$ , then the decoder chooses between the codeword pairs  $\{\hat{c}_1^1, \hat{c}_1^2\}$  and  $\{\hat{c}_2^1, \hat{c}_2^2\}$  having the highest cost.

At iteration  $e = 1$ , the Hungarian algorithm finds the minimum cost  $g_1$  using steps described in [73]. This produces a row-column pair  $\{(1, \hat{c}_1), (2, \hat{c}_2), \dots, (Q, \hat{c}_L)\}$  which corresponds to a codeword  $\hat{\mathbf{c}} = (\hat{c}_1 \hat{c}_2 \dots \hat{c}_L)$  with the minimum cost  $g_1$ . If  $\hat{\mathbf{c}} \notin \{\mathbf{C}_1, \mathbf{C}_2, \dots, \mathbf{C}_w\}$ , then solutions at  $e = 2, 3, \dots, Q$  are found using Murty's algorithm [74]. The solution matrix from the Hungarian algorithm at  $e = 1$  is used to create  $L - 1$  nodes or subsets  $U_1, U_2, \dots, U_{L-1}$ . The nodes are created by partitioning the solution matrix at  $e = 1$  such that  $U_1 = \{(1, \hat{j}_1)\}, \dots, U_{L-1} = \{(1, \hat{j}_1), \dots, (L-1, \hat{j}_{L-1})\}$ . The items with a bar ( $\bar{\cdot}$ ) in  $U_1, U_2, \dots, U_{L-1}$  are replaced with  $\infty$  while the other items are excluded. By solving for the minimum cost of each derived node, the next assignment is then derived from the node with the lowest cost. This process can be iterated from  $e = 2, 3, \dots, Q$  until  $\hat{\mathbf{c}} \in \{\mathbf{C}_1, \mathbf{C}_2, \dots, \mathbf{C}_w\}$ .

## 8.4 Simulation Results

The error rate performance of the space-time schemes are evaluated for an indoor environment for different values of the electrical SNRs. The transmitter units are assumed to be placed at the top of

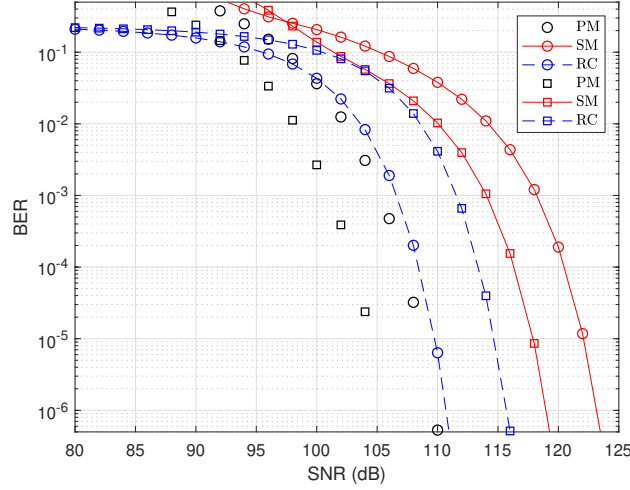


FIGURE 8.3: BER comparisons of PM with RC and SM for two channel matrices transmitting 4 bits. The circles and squares are plots for  $\mathbf{H}_{0.2}$  and  $\mathbf{H}_{0.6}$  respectively.

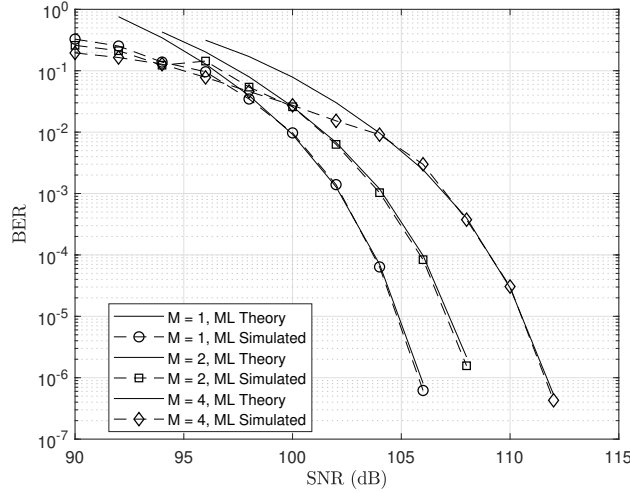


FIGURE 8.4: BER of concatenated codebooks of  $w = 1$  and  $w = 2$  containing 24 and 8 codewords respectively.

the room while the receiver units are placed on a table in the room, 1.75 m from the transmitters. The number of LEDs in the transmitter and PDs in the receiver are both four and the channel gain between each transmitter and receiver are calculated using (8.4). Spacing between the receivers is 0.1 m while different transmitter spacing  $D_{tx}$  are considered to generate the channel matrix  $\mathbf{H}_{D_{tx}}$  used for the numerical simulations. The channel matrix for  $D_{tx} = 0.2$  m also adopted from [109]

$$\mathbf{H}_{0.2} = \begin{bmatrix} 1.0708 & 0.9937 & 0.9937 & 0.9226 \\ 0.9937 & 1.0708 & 0.9226 & 0.9937 \\ 0.9937 & 0.9226 & 1.0708 & 0.9937 \\ 0.9226 & 0.9937 & 0.9937 & 1.0708 \end{bmatrix} \times 10^{-4},$$

with values obtained using (8.4) with 0.2 m and 0.1 m spacing between the transmitters and receivers respectively.  $A_{pd}$  is assumed to be unity while both  $\Phi_{\frac{1}{2}}$  and  $\Psi$  are set to  $15^\circ$  [111, 112]. We shorten the simulation properties by describing the schemes using  $P(L, Q, M, w)$  for single weight codebooks and  $P(L, Q, M, \{w_1, w_2\})$  for multiweight codebooks.

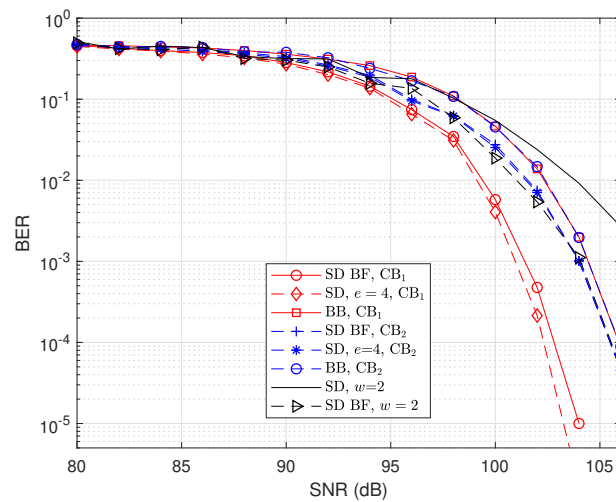


FIGURE 8.5: Comparison of soft-decision techniques with ML performance for  $P(4, 8, 1, 1)$  and  $P(4, 8, 1, 2)$  with  $H_{0.2}$ .

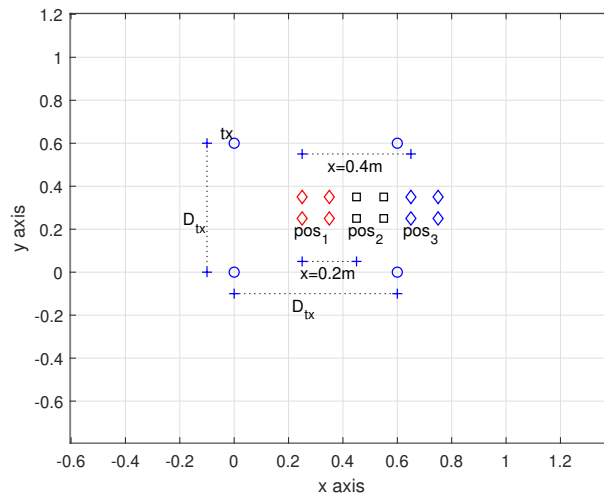


FIGURE 8.6: Top view cross-section of transmitter and receiver placements.

Fig. 8.3 shows the BER using two transmitter spacings  $D_{tx} = 0.2$  m and  $D_{tx} = 0.6$  m. The advantage of the space-time code over spatial multiplexing schemes such as RC and SM is seen in the BER performance as well as better transmitter spacing, improving the PM's performance. In Fig. 8.4, the combination of permutation codewords to increase the data rate is shown with the simulations matching the derived bound in (8.13). In the SD decoder of the combined codebooks, it is assumed the receiver can differentiate between transmitted  $w = 1$  and  $w > 2$  matrices because the decoder .

### 8.4.1 BER Analysis

The BER of the ML performance of the scheme with a perfect knowledge of the CSI is compared with the BER of the SD decoders. For the scheme using the concatenated codebook, equal total transmit power is maintained for all codewords by transmitting intensity  $\frac{I_m}{w}$  over each active transmitter.

In the results, the SD decoders decode the channel output directly, hence the CSI is not required. In Fig. 8.5 where  $w = 1$ , appropriate codeword selection can improve the performance of the SD decoder

rather than the minimum distance of the code. Hence, choosing codewords which exploit the channel gain properties of the  $\mathbf{H}$  matrix can produce a different performance of the SD decoder. The effect of codeword selection is shown using two different codebooks transmitting the same rate of information. The two codebooks are  $\text{CB}_1 = (4321, 4132, 3124, 3412, 2431, 2143, 2314, 1342)$  and  $\text{CB}_2 = (1234, 2134, 2143, 3214, 3124, 3241, 1342, 1432)$ .  $\text{CB}_1$  is chosen such that for each codeword, the total channel gain

$$\sum_{i=1}^L \sum_{j=1}^L h_{ij} s_{ij}, \quad (8.19)$$

is low.  $\text{CB}_2$  is the opposite where the codewords target the higher channel gains. It can be seen in Fig. 8.5 that the codebook which exploits the lower channel gains produces better BER performance from SD decoding. The BB decoder performance is however the same for both codebooks. For  $w = 2$ , the BER plots are compared with  $w = 1$  with the same power allocation to the activated LEDs and the same bits per transmit block. However, codeword selection is limited due to the number of codewords that meet the criteria in (8.7). The SD decoder of  $w = 2$  codewords differ in about 3 dB from the ML while the SD which uses the BF detection matches the ML BER performance.

### 8.4.2 Mobile Receiver without CSI

The transmitter and mobile receiver setups are shown in Fig. 8.6 with the blue circles showing the position of the transmitter (tx) with  $D_{\text{tx}} = 0.6$  m. The performance of the SD decoder as the receiver moves away from the direct LOS of the transmitter units is shown in Fig. 8.7 and 8.8 for combined codebooks of  $w = 1$  and  $w = 2$ . The first position ( $\text{pos}_1$ ) of the receiver is centered with the transmitter while the second and third positions ( $\text{pos}_2$  and  $\text{pos}_3$ ) are moved  $x$  m away from the first position. Perfect synchronization between the transmitters and receivers is assumed and three different positions at  $x = 0.0, 0.2$  and  $0.4$  m are shown in clusters of four diamond and black square shapes. Combining these two codebooks increases the bits per block for the same time block and transmitter units. Since the decoder does not require the CSI, the performance degrades from the ML with perfect CSI but is able to decode with about 4 dB difference when the receiver moves 0.2 m away from the transmitters' LOS. At  $x = 0.4$  m away from the transmitter, the SD fails to decode correctly.

Link blockage sets up the transmitter and receiver such that a PD is removed from the field of view of an LED. This has shown to assist with improving BER performance by cancelling possible interference caused by the link. Using the  $\mathbf{H}_{0.6}$  channel matrix as an example, the link blockage between transmitter and receiver pairs (1, 4), (2, 3), (3, 2) and (4, 1) produces a matrix

$$\tilde{\mathbf{H}}_{0.6} = \begin{bmatrix} 0.6888 & 0.5559 & 0.5559 & 0.0000 \\ 0.5559 & 0.6888 & 0.0000 & 0.5559 \\ 0.5559 & 0.0000 & 1.0708 & 0.5559 \\ 0.0000 & 0.5559 & 0.5559 & 0.6888 \end{bmatrix} \times 10^{-4},$$

with the zero elements showing the removal of the possible channel gains between the corresponding transmitter and receiver. The BER improvement is shown in Fig. 8.8 with the SD decoder matching its OD performance but with 4 dB loss when compared with the ML decoder.

### 8.4.3 Data Rate Analysis

The combination of codebooks with different weights makes more codewords available in order to increase the bits per symbol. Consider the codebook with  $L = 4$  which has 24 ( $L!$ ) matrices for  $w = 1$ . An exhaustive search of unique codewords that satisfy (8.7) produces 90 matrices for  $w = 2$ . For the same  $L$ , 24 matrices are found for  $w = 3$ . If the codebooks with the 3 weights are combined, 7 bits per symbol can be transmitted by each matrix compared to the possible 4 bits per symbol achievable for the  $w = 1$  codebook.

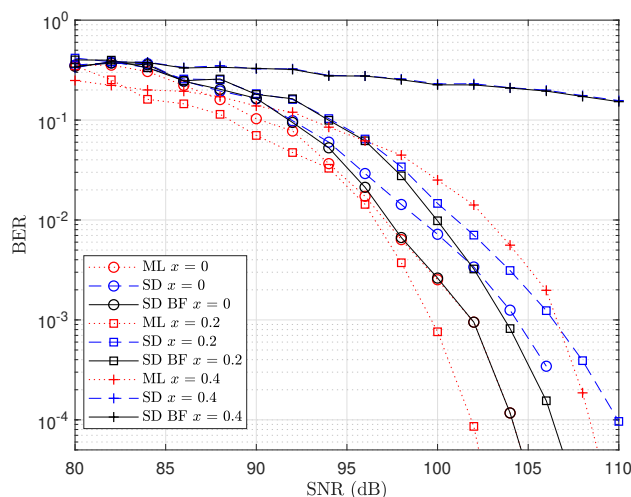


FIGURE 8.7: BER of concatenated codebooks of  $P(4, 8, 1, \{1, 2\})$  transmitting 5 bits with receiver at the transmitter's center using  $\mathbf{H}_{0.6}$  and different positions of the receiver.

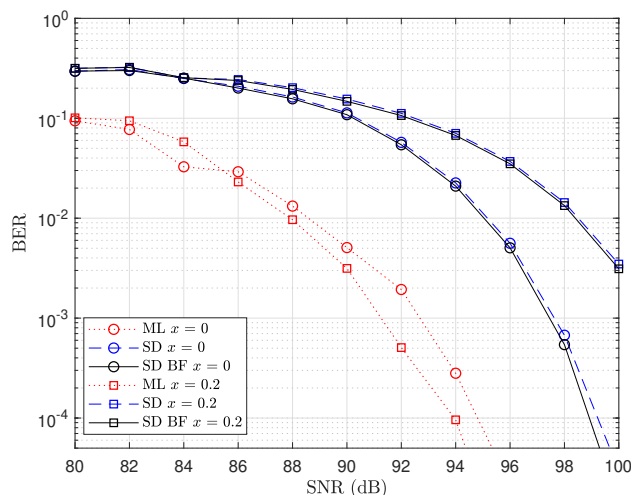


FIGURE 8.8: BER of concatenated codebooks of  $P(4, 8, 1, \{1, 2\})$  using  $\tilde{\mathbf{H}}_{0.6}$  for different positions of the receiver.

#### 8.4.4 Complexity Analysis of Soft-Decision Decoders

The decoders' complexities are analyzed based on the different operations required in the decoding process, while excluding circuitry complexities. Consider a received  $L \times L$  codeword matrix, which represents a received coded symbol and is fed into the decoder. The ML decoder compares the received codeword matrix with all possible  $Q$  codeword matrices used at the transmitter in order to make a decision. Depending on the method used, each element in the received codeword matrix can be compared with each element in the likely transmitted codeword matrix in order to find the distance between the two matrices. This method will additionally require  $L^2$  operations. Hence the ML decoder's complexity can be approximated as  $O(Q \cdot L^2)$ . With the same  $L \times L$  input size, the algorithms in the SD decoders perform their respective decoding operations. Using the tree-based method for BB in Fig. 8.2, each level requires  $L$  operations, i.e., for each node, and each node computes the individual costs before finding the minimum cost at each level. The complexity of the BB algorithm can then be approximated as  $O(L^3 \log L)$  since the number of nodes to compute reduce at

each level. In the SD decoder, each term in (8.15) requires a complexity of  $O(L^3)$  [124] at  $e = 1$  and  $O(L^4)$  [77] at  $e > 1$ . Therefore, the worst-case complexity can be approximated to  $O(L^4)$ . This implies the complexity of the SD decoder is dependent on the size of  $L$  rather than the size of the codebook  $Q$ . In large codebooks which can assist with creating codeword matrices for higher data rates,  $Q \gg L$ . The SD BF method finds the cost of each codeword and finds the codeword that minimizes (8.16). This approximates the complexity to  $O(L \cdot Q)$  in order to find the optimal cost that corresponds to the decoded codeword.

## 8.5 Conclusion

Concatenated permutations are used to increase the data rate of the PM-aided MIMO scheme in VLC by combining permutation matrices of different weights. Low-complexity, SD techniques are also used to detect the transmitted signals without the knowledge of the CSI. The results show the soft-decision decoder can match the ML decoder using certain codebooks and the decoding complexities are also analyzed. In future work, low-complexity code construction techniques are required because the brute force code construction is prohibitive computationally. Also, low-complexity, SD techniques which can decode without the CSI knowledge, yet with closer BER performance will assist with improving the overall system.

# Conclusions and Future Work

## 9.1 Conclusions

PLC using existing indoor power installations will become more attractive if reliable communication is possible with adequate, robust coding and modulation schemes. Communication over powerlines is already common in power grids to enable small data applications such as smart metering. Power grids are able to communicate with customer devices in homes and obtain necessary data from billing information to information that can assist with intelligent metering and energy scheduling applications. Vehicular technology is also embracing PLC while in underground mines, PLC is unconventionally used in smart blasting applications to link the blasting device to the detonators at the face. With PLC found in such a wide range of areas and the impending growth of connected devices, appropriately coded and modulated PLC will ensure more reliable communication.

VLC units are mostly powered by powerlines. This research has established a reliable channel model for a multicarrier modulation in a hybrid, indoor PLC-VLC channel under some indoor channel conditions. The derived models match the measured models relatively well, validating the accuracy of our model. The channel model also shows that while the errors in the PLC channel occur in bursts, the VLC channel is a cleaner channel but attenuates the signal as the angle between the receiver and transmitter increases. Hence, in scenarios where the VLC link has direct LOS, reliable PLC-VLC communication depends on the quality of signal forwarded from the PLC channel.

Coded systems generally improve error correction performance and permutation codes with  $M$ -FSK have generally been proven to mitigate the effect of impulsive noise in PLC. However, existing hard-decision decoders of permutation codes have exponential computational complexity, hence too complex for decoding large codebooks. By interpreting the output of the channel as an assignment problem, soft-decision decoders using optimization algorithms were designed in this research. The decoder algorithms estimated the likely transmitted codeword using the branch-and-bound algorithm as well as an iterative decoder which combines the Hungarian and Murty algorithms. The BER performance of the algorithms were first presented in AWGN and Rayleigh fading channels and they showed improvement in the BER performance while simultaneously reducing the computational complexity. Permutation codes were then used to encode the subcarriers in a multicarrier system that selects the active subcarriers using  $M$ -FSK. The soft-decision decoders were further used to decode the subcarriers in order to improve the performance as well as reduce the complexity. The performance of the soft-decision decoders were also extended to permutation trellis code (PTC) which serially concatenates convolutional codes with permutation codes. In PTC, the SD decoders were used to eliminate the demodulation step in the decoder, forward a permutation codeword to the Viterbi decoder which improved the overall BER performance of high rate PTC codes.

Indoor illumination units commonly exist as a cluster of LEDs, naturally creating a MIMO system. Hence, modulation schemes that eliminate ICI are attractive as well as detection schemes that mitigate channel estimation errors. Permutation modulation-aided STSK have been presented as an ICI mitigation technique with optimization algorithms used to detect the received, noisy matrix without the

knowledge of the CSI. This research evaluated the performance of the SD decoder when the channel coefficients are constant as well as the performance of the SD decoder when the channel coefficients change within a given range. This exposes the limits of the SD decoder's error correction performance when considered for a mobile receiver. However, permutation-coded systems in general, support low data rates, hence the need to present a novel technique that combines the codewords. Such combined codewords have the maximum Hamming distance between them in order to increase the number of active LED units per transmit block, hence increasing the data rate.

## 9.2 Future Work

With the derived channel model, the behavior of the channels becomes clearer for an indoor environment. The SD decoding algorithms presented have also been used to improve the BER performance at a reduced computational complexity, ranging from single carrier to multicarrier and trellis-coded schemes. Permutation coded schemes now have the potential for higher data rate communication as a result of the schemes presented in this thesis. While the higher rate scheme is presented in MIMO VLC, the power allocation for controlling the intensity of the activated, transmitting LEDs is not optimal. Investigating power allocation schemes that can exploit the indices of the activated LEDs for better BER performance will improve the feasibility of the MIMO VLC scheme. In addition, the limitation of the soft-decision decoder's inability to differentiate between single weight and multiweight transmit matrices requires investigation and schemes to correct this flaw. The concatenated concept can also be extended to permutation-coded,  $M$ -FSK single carrier and multicarrier schemes. Such novel concept can be further extended to designing multiple access (MA) codes for optical systems because of properties which are similar to existing combinatorial methods used for constructing optical orthogonal MA codes. Reliable communication of a hybrid AF PLC-VLC will enable more connected devices in homes, connected people and machines in underground mining environments, expand the reach of communication infrastructure and may deliver information to areas quicker and cheaper than conventional communication systems such as optic fibre and WiFi.

# Bibliography

- [1] L. U. Khan, "Visible light communication: Applications, architecture, standardization and research challenges," *Digital Communications and Networks*, vol. 3, no. 2, pp. 78 – 88, 2017. [Online]. Available: <http://www.sciencedirect.com/science/article/pii/S2352864816300335>
- [2] T. Komine and M. Nakagawa, "Fundamental analysis for visible-light communication system using LED lights," *IEEE Transactions on Consumer Electronics*, vol. 50, no. 1, pp. 100–107, Feb. 2004.
- [3] J. Hou and D. C. O'Brien, "Vertical handover-decision-making algorithm using fuzzy logic for the integrated radio-and-OW system," *IEEE Transactions on Wireless Communications*, vol. 5, no. 1, pp. 176–185, Jan. 2006.
- [4] Y. Wang, X. Wu, and H. Haas, "Load balancing game with shadowing effect for indoor hybrid LiFi/RF networks," *IEEE Transactions on Wireless Communications*, vol. 16, no. 4, pp. 2366–2378, Apr. 2017.
- [5] M. B. Rahaim, A. M. Vegni, and T. D. C. Little, "A hybrid radio frequency and broadcast visible light communication system," in *2011 IEEE GLOBECOM Workshops (GC Wkshps)*, Dec. 2011, pp. 792–796.
- [6] W.-Y. Lin, C.-Y. Chen, H.-H. Lu, C.-H. Chang, Y.-P. Lin, H.-C. Lin, and H.-W. Wu, "10m/500mbps WDM visible light communication systems," *Opt. Express*, vol. 20, no. 9, pp. 9919–9924, Apr. 2012. [Online]. Available: <http://www.opticsexpress.org/abstract.cfm?URI=oe-20-9-9919>
- [7] F. M. Wu, C. T. Lin, C. C. Wei, C. W. Chen, Z. Y. Chen, H. T. Huang, and S. Chi, "Performance comparison of OFDM signal and CAP signal over high capacity RGB-LED-based WDM visible light communication," *IEEE Photonics Journal*, vol. 5, no. 4, pp. 7901507–7901507, Aug. 2013.
- [8] J. Vučić, C. Kottke, K. Habel, and K. Langer, "803 mbit/s visible light WDM link based on DMT modulation of a single RGB LED luminary," in *2011 Optical Fiber Communication Conference and Exposition and the National Fiber Optic Engineers Conference*, Mar. 2011, pp. 1–3.
- [9] C. Kamwangala, M. A. Cox, and L. Cheng, "Transmitter power control for a multicarrier visible light communication system," *Transactions on Emerging Telecommunications Technologies*, vol. 30, no. 2, p. e3453, 2019.
- [10] S. Hranilovic, "On the design of bandwidth efficient signalling for indoor wireless optical channels," *International Journal of Communication Systems*, vol. 18, no. 3, pp. 205–228, Apr. 2005. [Online]. Available: <http://doi.org/10.1002/dac.700>
- [11] J. Armstrong and B. J. C. Schmidt, "Comparison of asymmetrically clipped optical OFDM and DC-biased optical OFDM in AWGN," *IEEE Communications Letters*, vol. 12, no. 5, pp. 343–345, May 2008.
- [12] O. Gonzalez, R. Perez-Jimenez, S. Rodriguez, J. Rabadan, and A. Ayala, "OFDM over indoor wireless optical channel," *IEEE Proceedings - Optoelectronics*, vol. 152, no. 4, pp. 199–204, Aug. 2005.
- [13] T. Komine and M. Nakagawa, "Integrated system of white LED visible-light communication and power-line communication," in *The 13th IEEE International Symposium on Personal, Indoor and Mobile Radio Communications*, vol. 4, Sept. 2002, pp. 1762–1766 vol.4.

- [14] A. D. Familua, A. R. Ndjiongue, K. Ogunyanda, L. Cheng, H. C. Ferreira, and T. G. Swart, "A semi-hidden Markov modeling of a low complexity FSK-OOK in-house PLC and VLC integration," in *2015 IEEE International Symposium on Power Line Communications and Its Applications (ISPLC)*, Mar. 2015, pp. 199–204.
- [15] A. R. Ndjiongue, H. C. Ferreira, K. Ouahada, and A. J. H. Vinck, "Low-complexity SOCPBFSK-OOK interface between PLC and VLC channels for low data rate transmission applications," in *18th IEEE International Symposium on Power Line Communications and Its Applications*, Mar. 2014, pp. 226–231.
- [16] T. Komine, S. Haruyama, and M. Nakagawa, "Performance evaluation of narrowband OFDM on integrated system of power line communication and visible light wireless communication," in *2006 1st International Symposium on Wireless Pervasive Computing*, Jan. 2006, pp. 6 pp.–6.
- [17] A. R. Ndjiongue, T. Shongwe, H. C. Ferreira, T. M. N. Ngatched, and A. J. H. Vinck, "Cascaded PLC-VLC channel using OFDM and CSK techniques," in *2015 IEEE Global Communications Conference (GLOBECOM)*, Dec. 2015, pp. 1–6.
- [18] S. M. Nlom, A. R. Ndjiongue, K. Ouahada, H. C. Ferreira, A. J. H. Vinck, and T. Shongwe, "A simplistic channel model for cascaded PLC-VLC systems," in *2017 IEEE International Symposium on Power Line Communications and its Applications (ISPLC)*, Apr. 2017, pp. 1–6.
- [19] A. R. Ndjiongue, H. C. Ferreira, J. Song, F. Yang, and L. Cheng, "Hybrid PLC-VLC channel model and spectral estimation using a nonparametric approach," *Transactions on Emerging Telecommunications Technologies*, vol. 28, no. 12, p. e3224, 2017.
- [20] J. Song, S. Liu, G. Zhou, B. Yu, W. Ding, F. Yang, H. Zhang, X. Zhang, and A. Amara, "A cost-effective approach for ubiquitous broadband access based on hybrid PLC-VLC system," in *2016 IEEE International Symposium on Circuits and Systems (ISCAS)*, May 2016, pp. 2815–2818.
- [21] L. L. H. Ma and S. Hranilovic, "Subcarrier allocation in hybrid visible light and power line communication system," in *2016 IEEE International Symposium on Circuits and Systems (ISCAS)*, May 2016, pp. 2819–2822.
- [22] O. Kolade, M. Cox, and L. Cheng, "Visible light communication using a software-defined radio approach," in *Fifth Conference on Sensors, MEMS, and Electro-Optic Systems*, Jan. 2019.
- [23] H. C. Ferreira, A. J. H. Vinck, T. G. Swart, and I. de Beer, "Permutation trellis codes," *IEEE Transactions on Communications*, vol. 53, no. 11, pp. 1782–1789, Nov. 2005.
- [24] S. Sugiura, S. Chen, and L. Hanzo, "Coherent and differential space-time shift keying: A dispersion matrix approach," *IEEE Transactions on Communications*, vol. 58, no. 11, pp. 3219–3230, Nov. 2010.
- [25] —, "A universal space-time architecture for multiple-antenna aided systems," *IEEE Communications Surveys & Tutorials*, vol. 14, no. 2, pp. 401–420, 2012.
- [26] O. Kolade, A. D. Familua, and L. Cheng, "Indoor amplify-and-forward power-line and visible light communication channel model based on a semi-hidden Markov model," *AEU - International Journal of Electronics and Communications*, p. 153108, 2020. [Online]. Available: <http://www.sciencedirect.com/science/article/pii/S1434841119324823>
- [27] O. Kolade, J. Versfeld, and M. Van Wyk, "Soft-decision decoding of permutation block codes in AWGN and Rayleigh fading channels," *IEEE Communications Letters*, vol. 21, no. 12, pp. 2590–2593, 2017.
- [28] O. Kolade and L. Cheng, "Impulse noise mitigation using subcarrier coding of OFDM-MFSK scheme in powerline channel," in *2019 IEEE International Conference on Communications, Control, and Computing Technologies for Smart Grids (SmartGridComm)*, 2019, pp. 1–6.

- [29] —, "Permutation-aided space-time shift keying for indoor visible light communication," in *2019 IEEE International Conference on Communications, Control, and Computing Technologies for Smart Grids (SmartGridComm)*, Oct. 2019, pp. 1–6.
- [30] K. D. M. Zimmermann, "A multipath model for the powerline channel," *IEEE Transactions on Communications*, vol. 50, no. 4, pp. 553–559, Aug. 2002.
- [31] D. Middleton, "Statistical-physical model of electromagnetic interference," *IEEE Transactions on Electromagnetic Compatibility*, vol. EMC-19, no. 3, p. 106–127, Aug. 1977.
- [32] —, "Non-Gaussian noise models in signal processing for telecommunications: New methods and results for Class A and Class B noise models," *IEEE Transactions on Information Theory*, vol. 45, no. 4, p. 1129–1149, May 1999.
- [33] M. Ghosh, "Analysis of the effect of impulse noise on multicarrier and single carrier QAM systems," *IEEE Transactions on Communications*, vol. 44, no. 2, pp. 145–147, Feb. 1996.
- [34] R. Pighi, M. Franceschini, G. Ferrari, and R. Raheli, "Fundamental performance limits of communications systems impaired by impulse noise," *IEEE Transactions on Communications*, vol. 57, no. 1, pp. 171–182, Jan. 2009.
- [35] W. P. Z. Ghassemlooy and S. Rajbhandari, *Optical wireless communications: system and channel modelling with Matlab®*. CRC Press, 2012, ch. 3.
- [36] M. Ettus, *Universal software radio peripheral (USRP)*, 2008. [Online]. Available: <http://www.ettus.com>
- [37] T.-Y. Lin, R. J. Green, and P. B. O'Connor, "A low noise single-transistor transimpedance preamplifier for Fourier-transform mass spectrometry using a T feedback network," *Review of Scientific Instruments*, vol. 83, no. 9, p. 094102, 2012.
- [38] J. G. Proakis and M. Salehi, *Digital Communications*, 5th ed. McGraw-Hill, 2008, pp. 203–219, 846–849.
- [39] K. Cho and D. Yoon, "On the general BER expression of one- and two-dimensional amplitude modulations," *IEEE Transactions on Communications*, vol. 50, no. 7, pp. 1074–1080, Jul. 2002.
- [40] A. Nuwanpriya, S. Ho, J. A. Zhang, A. J. Grant, and L. Luo, "PAM-SCFDE for optical wireless communications," *Journal of Lightwave Technology*, vol. 33, no. 14, pp. 2938–2949, Jul. 2015.
- [41] D. Slepian, "Permutation modulation," *Proceedings of the IEEE*, vol. 53, no. 3, pp. 228–236, Mar. 1965.
- [42] S. Lin and D. Costello, *Error-Correcting Codes*. Prentice-Hall, Inc, 1983.
- [43] H. C. Ferreira, D. A. Wright, and A. L. Nel, "Hamming distance preserving mappings and trellis codes with constrained binary symbols," *IEEE Transactions on Information Theory*, vol. 35, no. 5, pp. 1098–1103, Sep. 1989.
- [44] A. J. H. Vinck, J. Haering, and T. Wadayama, "Coded M-FSK for power line communications," in *Proceedings, IEEE International Symposium on Information Theory*, Jun. 2000, p. 137.
- [45] Y. H. Ma, P. L. So, and E. Gunawan, "Performance analysis of OFDM systems for broadband power line communications under impulsive noise and multipath effects," *IEEE Transactions on Power Delivery*, vol. 20, no. 2, pp. 674–682, 2005.
- [46] E. R. D. France, *G3-PLC physical layer specification*, Aug. 2009. [Online]. Available: <http://www.maximintegrated.com/products/powerline/pdfs/G-PLC-Physical-Layer-Specification.pdf>
- [47] P. Project, *Technology white paper: PHY MAC and convergence layers*, Jul. 2008.

- [48] P. Amirshahi, S. M. Navidpour, and M. Kavehrad, "Performance analysis of uncoded and coded OFDM broadband transmission over low voltage powerline channels with impulsive noise," *IEEE Transactions on Power Delivery*, vol. 21, no. 4, pp. 1927–1934, Oct. 2006.
- [49] R. Mesleh, H. Haas, C. W. Ahn, and S. Yun, "Spatial modulation - a new low complexity spectral efficiency enhancing technique," in *2006 First International Conference on Communications and Networking in China*, Oct. 2006, pp. 1–5.
- [50] N. Andreadou and F. N. Pavlidou, "PLC channel: Impulsive noise modelling and its performance evaluation under different array coding schemes," *IEEE Transactions on Power Delivery*, vol. 24, no. 2, pp. 585–595, Apr. 2009.
- [51] D. Middleton, "Canonical and quasi-canonical probability models of Class A interference," *IEEE Transactions on Electromagnetic Compatibility*, vol. EMC-25, no. 2, pp. 76–106, May 1983.
- [52] O. G. Hooijen, "On the channel capacity of the residential power circuit used as a digital communications medium," *IEEE Communications Letters*, vol. 2, no. 10, pp. 267–268, Oct. 1998.
- [53] W. Ding, F. Yang, H. Yang, J. Wang, X. Wang, X. Zhang, and J. Song, "A hybrid power line and visible light communication system for indoor hospital applications," *Computers in Industry*, vol. 68, pp. 170–178, 2015.
- [54] X. Ma, J. Gao, F. Yang, W. Ding, H. Yang, and J. Song, "Integrated power line and visible light communication system compatible with multi-service transmission," *IET Communications*, vol. 11, no. 1, pp. 104–111, 2017.
- [55] F. R. Gfeller and U. Bapst, "Wireless in-house data communication via diffuse infrared radiation," *Proceedings of the IEEE*, vol. 67, no. 11, pp. 1474–1486, Nov. 1979.
- [56] R. A. Howard, *Dynamic probabilistic systems: Markov models*. Courier Corporation, 2012, vol. 1.
- [57] L. Rabiner and B. Juang, "An introduction to hidden Markov models," *IEEE ASSP magazine*, vol. 3, no. 1, pp. 4–16, 1986.
- [58] H. S. Wang and N. Moayeri, "Finite-state Markov channel-A useful model for radio communication channels," *IEEE Transactions on Vehicular Technology*, vol. 44, no. 1, pp. 163–171, 1995.
- [59] E. N. Gilbert, "Capacity of a burst-noise channel," *Bell system technical journal*, vol. 39, no. 5, pp. 1253–1265, 1960.
- [60] S. Sivaprakasam and K. S. Shanmugan, "An equivalent Markov model for burst errors in digital channels," *IEEE Transactions on Communications*, vol. 43, no. 2/3/4, pp. 1347–1355, 1995.
- [61] A. D. Familua and L. Cheng, "First and second-order semi-hidden Fritchman Markov models for a multi-carrier based indoor narrowband power line communication system," *Physical Communication*, vol. 29, pp. 55 – 66, 2018. [Online]. Available: <http://www.sciencedirect.com/science/article/pii/S1874490717302343>
- [62] G. Ndo, F. Labeau, and M. Kassouf, "A Markov-Middleton model for bursty impulsive noise: Modeling and receiver design," *IEEE Transactions on Power Delivery*, vol. 28, no. 4, p. 2317–2325, Oct. 2013.
- [63] B. Fritchman, "A binary channel characterization using partitioned Markov chains," *IEEE transactions on Information Theory*, vol. 13, no. 2, pp. 221–227, 1967.
- [64] D. G. Holmes, L. Cheng, M. Shimaponda-Nawa, A. D. Familua, and A. M. Abu-Mahfouz, "Modelling noise and pulse width modulation interference in indoor visible light communication channels," *AEU-International Journal of Electronics and Communications*, vol. 106, pp. 40–47, 2019.
- [65] *MATLAB*, The Mathworks, Inc., Natick, Massachusetts, 2017. [Online]. Available: <https://www.mathworks.com>

- [66] L. E. Baum, T. Petrie, G. Soules, and N. Weiss, "A maximization technique occurring in the statistical analysis of probabilistic functions of Markov chains," *The annals of mathematical statistics*, vol. 41, no. 1, pp. 164–171, 1970.
- [67] T. R. W. Tranter, K. Shanmugan and K. Kosbar, "Principles of communication systems simulation with wireless applications," *Prentice Hall Press*, vol. 1, pp. 601–623, 2003.
- [68] A. D. Familua and L. Cheng, "A semi-hidden Fritchman Markov modeling of indoor CENELEC A narrowband power line noise based on signal level measurements," *AEU-International Journal of Electronics and Communications*, vol. 74, pp. 21–30, 2017.
- [69] A. J. H. Vinck, "Coding for a terrible channel," in *EU-COST289 2nd Workshop Special Topics on 4G Technologies*, University of Duisburg-Essen, Germany, Jul. 8-9, 2005, pp. 101–106.
- [70] S. Huczynska, "Powerline communication and the 36 officers problem," *Philosophical Transactions of the Royal Society of London A: Mathematical, Physical and Engineering Sciences*, vol. 364, no. 1849, pp. 3199–3214, 2006. [Online]. Available: <http://rsta.royalsocietypublishing.org/content/364/1849/3199>
- [71] K. W. Shum, "Permutation coding and MFSK modulation for frequency selective channel," in *Personal, Indoor and Mobile Radio Communications, 2002. The 13th IEEE International Symposium on*, vol. 5, Sep. 2002, pp. 2063–2066.
- [72] R. Ahlswede and G. Dueck, "Good codes can be produced by a few permutations," *IEEE Transactions on Information Theory*, vol. 28, no. 3, pp. 430–443, May 1982.
- [73] H. W. Kuhn, "The Hungarian method for the assignment problem," *Naval Research Logistics Quarterly*, vol. 2, no. 1-2, pp. 83–97, 1955. [Online]. Available: <http://dx.doi.org/10.1002/nav.3800020109>
- [74] K. Murty, "Letter to the editor — an algorithm for ranking all the assignments in order of increasing cost," *Operations Research*, vol. 16, no. 3, pp. 682–687, 1968. [Online]. Available: <http://dx.doi.org/10.1287/opre.16.3.682>
- [75] A. Matache and J. A. Ritcey, "Optimum code rates for noncoherent MFSK with errors and erasures decoding over Rayleigh fading channels," in *Conference Record of the Thirty-First Asilomar Conference on Signals, Systems Computers*, vol. 1, Nov. 1997, pp. 62–66.
- [76] J. D. Choi, D.-S. Yoo, and W. E. Stark, "Performance limits of M-FSK with Reed-Solomon coding and diversity combining," *IEEE Transactions on Communications*, vol. 50, no. 11, pp. 1787–1797, Nov. 2002.
- [77] L. Liu and D. A. Shell, "Assessing optimal assignment under uncertainty: An interval-based algorithm," *The International Journal of Robotics Research*, vol. 30, no. 7, pp. 936–953, 2011. [Online]. Available: <https://doi.org/10.1177/0278364911404579>
- [78] I. J. Cox, M. L. Miller, R. Danchick, and G. E. Newnam, "A comparison of two algorithms for determining ranked assignments with application to multitarget tracking and motion correspondence," *IEEE Transactions on Aerospace and Electronic Systems*, vol. 33, no. 1, pp. 295–301, Jan. 1997.
- [79] K. Ogonyanda, A. D. Familua, T. G. Swart, H. C. Ferreira, and L. Cheng, "Adaptive permutation coded differential OFDM system for power line communications," in *2014 IEEE 6th International Conference on Adaptive Science Technology (ICAST)*, Oct. 2014, pp. 1–7.
- [80] C. J. Colbourn, T. Klove, and A. C. H. Ling, "Permutation arrays for powerline communication and mutually orthogonal Latin squares," *IEEE Transactions on Information Theory*, vol. 50, no. 6, pp. 1289–1291, June 2004.
- [81] L. Cheng and H. C. Ferreira, "Time-diversity permutation coding scheme for narrow-band power-line channels," in *2012 IEEE International Symposium on Power Line Communications and Its Applications*, March 2012, pp. 120–125.

- [82] M. Wetz, W. G. Teich, and J. Lindner, "OFDM-MFSK with differentially encoded phases for robust transmission over fast fading channels," in *11th International OFDM-Workshop*, 2006.
- [83] E. Peiker-Feil, M. Wetz, W. G. Teich, and J. Lindner, "OFDM-MFSK as a special case of noncoherent communication based on subspaces," in *OFDM 2012; 17th International OFDM Workshop 2012 (InOWo'12)*, Aug. 2012, pp. 1–5.
- [84] G. Yammine, E. Peiker, W. G. Teich, and J. Lindner, "Improved performance of coded OFDM-MFSK using combined alphabets and extended mapping," in *2014 8th International Symposium on Turbo Codes and Iterative Information Processing (ISTC)*, Aug. 2014, pp. 17–21.
- [85] M. Ndlovu and L. Cheng, "An OFDM inter-subcarrier permutation coding scheme for power-line communication," in *18th IEEE International Symposium on Power Line Communications and Its Applications*. IEEE, 2014, pp. 196–201.
- [86] G. Al-Juboori, A. Doufexi, and A. R. Nix, "Feasibility study of OFDM-MFSK modulation scheme for smart metering technology," in *2017 IEEE PES Innovative Smart Grid Technologies Conference Europe (ISGT-Europe)*, Sept. 2017, pp. 1–6.
- [87] G. Al-Juboori, E. Tsimbalo, A. Doufexi, and A. R. Nix, "A comparison of OFDM and GFDM-based MFSK modulation schemes for robust IoT applications," in *2017 IEEE 85th Vehicular Technology Conference (VTC Spring)*, Jun. 2017, pp. 1–5.
- [88] H. C. Ferreira and A. J. H. Vinck, "Interference cancellation with permutation trellis codes," in *Vehicular Technology Conference Fall 2000. IEEE VTS Fall VTC2000. 52nd Vehicular Technology Conference (Cat. No.00CH37152)*, vol. 5, Sep. 2000, pp. 2401–2407 vol.5.
- [89] T. M. Lukusa, K. Ouahada, and H. C. Ferreira, "Advantage of using permutation trellis codes and M-FSK modulation for power-line communications channel," in *AFRICON, 2011*, Sept. 2011, pp. 1–6.
- [90] R. E. Bardan, E. Masazade, O. Ozdemir, and P. K. Varshney, "Performance of permutation trellis codes in cognitive radio networks," in *2012 35th IEEE Sarnoff Symposium*, 2012, pp. 1–6.
- [91] R. El-Bardan, E. Masazade, O. Ozdemir, Y. S. Han, and P. K. Varshney, "Permutation trellis coded multi-level FSK signaling to mitigate primary user interference in cognitive radio networks," *IEEE Transactions on Communications*, vol. 64, no. 1, pp. 104–116, Jan. 2016.
- [92] F. Gagnon and D. Haccoun, "Coding and modulation schemes for slow fading channels," *IEEE Transactions on Communications*, vol. 43, no. 2/3/4, pp. 858–868, Feb. 1995.
- [93] K. Ouahada, "Improved Viterbi-decoding performance in the presence of permanent frequency disturbances in power-line environment," in *AFRICON, 2011*, Sept. 2011, pp. 1–5.
- [94] J.-C. Chang, R.-J. Chen, T. Klove, and S.-C. Tsai, "Distance-preserving mappings from binary vectors to permutations," *IEEE Transactions on Information Theory*, vol. 49, no. 4, pp. 1054–1059, Apr. 2003.
- [95] A. Viterbi, "Error bounds for convolutional codes and an asymptotically optimum decoding algorithm," *IEEE Transactions on Information Theory*, vol. 13, no. 2, pp. 260–269, Apr. 1967.
- [96] J. D. Little, K. G. Murty, D. W. Sweeney, and C. Karel, "An algorithm for the traveling salesman problem," *Operations research*, vol. 11, no. 6, pp. 972–989, 1963.
- [97] G. T. Ross and R. M. Soland, "A branch and bound algorithm for the generalized assignment problem," *Mathematical programming*, vol. 8, no. 1, pp. 91–103, 1975.
- [98] R. Leroy, "Parallel branch-and-bound revisited for solving permutation combinatorial optimization problems on multi-core processors and coprocessors. (algorithmes branch-and-bound parallèles revisités pour la résolution de problèmes d'optimisation combinatoire de permutation sur processeurs multi-cœurs et coprocesseurs)," Ph.D. dissertation, Lille University of Science and Technology, France, 2015. [Online]. Available: <https://tel.archives-ouvertes.fr/tel-01248563>

- [99] J. Marcum, "Table of q functions." *Rand Corporation*, 1950.
- [100] B. J. Lageweg, J. K. Lenstra, and A. H. G. R. Kan, "A general bounding scheme for the permutation flow-shop problem," *Operations Research*, vol. 26, no. 1, pp. 53–67, 1978. [Online]. Available: <http://0-www.jstor.org.innopac.wits.ac.za/stable/169891>
- [101] J. Jeganathan, A. Ghrayeb, L. Szczecinski, and A. Ceron, "Space shift keying modulation for MIMO channels," *IEEE Transactions on Wireless Communications*, vol. 8, no. 7, pp. 3692–3703, Jul. 2009.
- [102] J. Jeganathan, A. Ghrayeb, and L. Szczecinski, "Generalized space shift keying modulation for MIMO channels," in *2008 IEEE 19th International Symposium on Personal, Indoor and Mobile Radio Communications*. IEEE, 2008, pp. 1–5.
- [103] —, "Spatial modulation: optimal detection and performance analysis," *IEEE Communications Letters*, vol. 12, no. 8, pp. 545–547, Aug. 2008.
- [104] R. Y. Mesleh, H. Haas, S. Sinanovic, C. W. Ahn, and S. Yun, "Spatial modulation," *IEEE Transactions on Vehicular Technology*, vol. 57, no. 4, pp. 2228–2241, Jul. 2008.
- [105] S. Sugiura, S. Chen, and L. Hanzo, "Generalized space-time shift keying designed for flexible diversity-, multiplexing- and complexity-tradeoffs," *IEEE Transactions on Wireless Communications*, vol. 10, no. 4, pp. 1144–1153, Apr. 2011.
- [106] Y. Bian, M. Wen, X. Cheng, H. V. Poor, and B. Jiao, "A differential scheme for spatial modulation," in *2013 IEEE Global Communications Conference (GLOBECOM)*. IEEE, 2013, pp. 3925–3930.
- [107] N. Ishikawa and S. Sugiura, "Unified differential spatial modulation," *IEEE Wireless Communications Letters*, vol. 3, no. 4, pp. 337–340, Aug. 2014.
- [108] R. Mesleh, H. Elgala, and H. Haas, "Optical spatial modulation," *IEEE/OSA Journal of Optical Communications and Networking*, vol. 3, no. 3, pp. 234–244, Mar. 2011.
- [109] T. Fath and H. Haas, "Performance comparison of MIMO techniques for optical wireless communications in indoor environments," *IEEE Transactions on Communications*, vol. 61, no. 2, pp. 733–742, Feb. 2013.
- [110] S. P. Alaka, T. L. Narasimhan, and A. Chockalingam, "Generalized spatial modulation in indoor wireless visible light communication," in *2015 IEEE Global Communications Conference (GLOBECOM)*, Dec. 2015, pp. 1–7.
- [111] D. C. O'Brien, G. Faulkner, O. Bouchet, M. El Tabach, M. Wolf, J. W. Walewski, S. Randel, S. Nerreter, M. Franke, K. Langer, J. Grubor, and T. Kamalakis, "Home access networks using optical wireless transmission," in *2008 IEEE 19th International Symposium on Personal, Indoor and Mobile Radio Communications*, Sept. 2008, pp. 1–5.
- [112] O. Bouchet, G. Faulkner, L. Grobe, E. Gueutier, K. Langer, S. Nerreter, D. O'Brien, R. Turnbull, J. Vucic, J. Walewski *et al.*, "Deliverable D4. 2b physical layer design and specification," *Seventh Framework Programme Information Commun. Technol.*, 2011.
- [113] V. Tarokh, H. Jafarkhani, and A. R. Calderbank, "Space-time block codes from orthogonal designs," *IEEE Transactions on Information Theory*, vol. 45, no. 5, pp. 1456–1467, Jul. 1999.
- [114] S. M. Alamouti, "A simple transmit diversity technique for wireless communications," *IEEE Journal on Selected Areas in Communications*, vol. 16, no. 8, pp. 1451–1458, Oct. 1998.
- [115] J. M. Kahn and J. R. Barry, "Wireless infrared communications," *Proceedings of the IEEE*, vol. 85, no. 2, pp. 265–298, Feb. 1997.
- [116] L. Xiao, Y. Xiao, P. Yang, J. Liu, S. Li, and W. Xiang, "Space-time block coded differential spatial modulation," *IEEE Transactions on Vehicular Technology*, vol. 66, no. 10, pp. 8821–8834, Oct. 2017.

- [117] E. Bayaki and R. Schober, "Performance and design of coherent and differential space-time coded FSO systems," *Journal of Lightwave Technology*, vol. 30, no. 11, pp. 1569–1577, Jun. 2012.
- [118] I. Lai, J. Shih, C. Lee, H. Tu, J. Chi, J. Wu, and Y. Huang, "Spatial permutation modulation for multiple-input multiple-output (MIMO) systems," *IEEE Access*, vol. 7, pp. 68 206–68 218, 2019.
- [119] J. Chi, Y. Yeh, I. Lai, and Y. Huang, "Sphere decoding for spatial permutation modulation MIMO systems," in *2017 IEEE International Conference on Communications (ICC)*, 2017, pp. 1–8.
- [120] A. Nuwanpriya, S. Ho, and C. S. Chen, "Indoor MIMO visible light communications: Novel angle diversity receivers for mobile users," *IEEE Journal on Selected Areas in Communications*, vol. 33, no. 9, pp. 1780–1792, 2015.
- [121] R. Heymann, J. H. Weber, T. G. Swart, and H. C. Ferreira, "Concatenated permutation block codes based on set partitioning for substitution and deletion error-control," in *2013 IEEE Information Theory Workshop (ITW)*, Sep. 2013, pp. 1–5.
- [122] P. Frankl and M. Deza, "On the maximum number of permutations with given maximal or minimal distance," *Journal of Combinatorial Theory, Series A*, vol. 22, no. 3, pp. 352 – 360, 1977. [Online]. Available: <http://www.sciencedirect.com/science/article/pii/0097316577900097>
- [123] L. Euler, "Recherches sur un nouvelle espèce de quarrés magiques," *Verhandelingen uitgegeven door het zeeuwisch Genootschap der Wetenschappen te Vlissingen*, pp. 85–239, 1782.
- [124] D. Smith, "On the computation complexities of branch and bound strategies," Master's thesis, Naval Postgraduate School, Monterey, California, 1979.